A Broadband Optical Ring Resonator for Absorption and Refractive Index Detection

Thomas Christopher Oates

A dissertation

submitted in partial fulfillment of the

requirements for the degree of

Doctor of Philosophy

University of Washington

2013

Reading Committee:

Lloyd W. Burgess, Chair

Robert E. Synovec

Bo Zhang

Program Authorized to Offer Degree:

Department of Chemistry

University of Washington

Abstract

A Broadband Optical Ring Resonator for Absorption and Refractive Index Detection

Thomas Christopher Oates

Chair of the Supervisory Committee:

Research Professor Lloyd W. Burgess

Department of Chemistry

Optical ring resonators have been studied in recent years as chemical sensors. Conventionally, these devices are operated by means of tracking a single resonance wavelength through use of a finely tunable laser source. This wavelength will shift as a result of changing resonator conditions, such as a refractive index (RI) shift resulting from sample analyte activity. In this work, an alternative approach to the conventional ring resonator methods is presented. This approach utilizes a 'broadband' (relative to a monochromatic laser) light source such as a light emitting diode.

Results are presented for both absorption and RI detection. While the demonstrated absorbance enhancement for surface-active analytes is theoretically anticipated, the observed RI sensitivity exceeds expectations. Due to multiple optical mechanisms that are simultaneously affected by an RI shift, detection limits on the order of 10^{-6} RIU (refractive index units) are presented using Fourier-transform based extraction of interference components from output spectra. Additional device characterizations are performed for a number of variables, including wall thickness, fabrication method, detector resolution, and dynamic range.

Through study of these new methods, certain advantages become clear. While one is the ability to take absorbance and RI measurements with the same device, perhaps the most significant advantage is the compatibility these methods have with lower quality resonators, such as those which could be mass-produced. With these aspects in mind, potential absorption and RI based applications are probed further. Low-cost and/or portable devices are proposed, as well as improvements on classical analytical methods and biosensing applications.

Table of Contents

List of Figures

Acknowledgement

To Lloyd, for providing me with just the right balance of guidance and freedom.

To my parents and sister, for supporting my scientific interests since childhood.

To my wife, Julie, for keeping me afloat with her unconditional love and support

CHAPTER 1

Introduction

Resonant Devices

Tapping on a glass of water with a spoon will produce a tone. Repeated tapping will produce the same tone so predictably that a song can be played using several different glasses of water. In Figure 1, taken from a 15th century music theory textbook, Pythagoras is shown demonstrating this experiment, along with an early understanding of resonance frequencies. (Johnston, 2009)

Figure 1-1 – Ancient illustration of resonant tones produced from glasses of water

The tones illustrated in Figure 1-1 are produced from constructive interference and amplification of particular frequencies along with destructive interference and attenuation of all other frequencies. This is known as resonance. In the case of the glasses of water, the resonance was storage of physical vibrations. Resonance can also occur with types of energy such as electromagnetic radiation, including visible light. In either case, the particular frequencies being

amplified, or 'resonance frequencies', are a function of the dimensions and physical properties of the device storing the energy. In the case of the glasses of water, simply changing the volume of water in each glass changes these physical properties, and thus the tone produced. A resonator's ability to accept resonant, and filter out non-resonant, frequencies is referred to as its 'quality'. This is often quantified as a 'Q-factor', defined as the frequency divided by the peak width at half of the maximum peak height, as illustrated in Figure 1-2. (Davis, 2010) In this figure, X/X_m represents the displacement relative to maximum, ω/ω_0 represents frequency relative to central resonance frequency, and sharper and narrower peaks are shown to have a higher Q-factor.

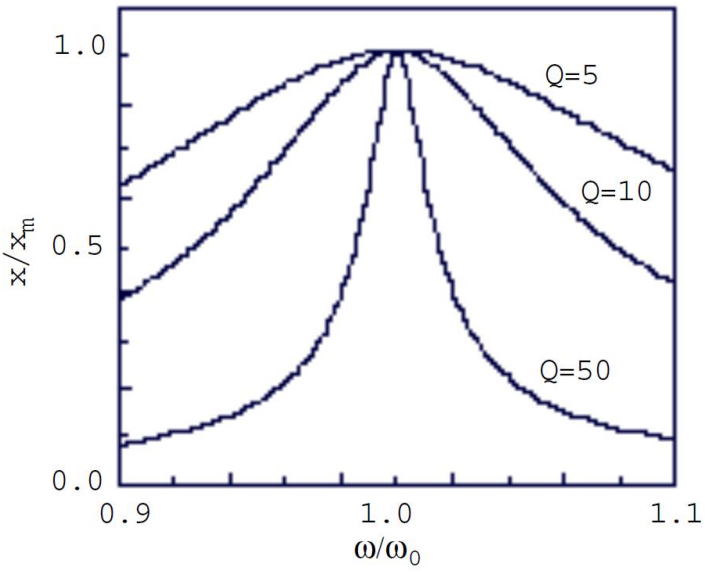

Figure 1-2 - Resonance peaks of varying quality (Reproduced with permission from NASA)

The resonance frequency of a device is a function of the physical dimensions and properties of the device. The influence that a chemical analyte has on these physical properties can be detected through the measurement of the resonance frequency shift. Most resonance-based chemical sensors can be categorized as being either mechanical, utilizing physical vibrations, or optical. (Wang & Anslyn, 2011)

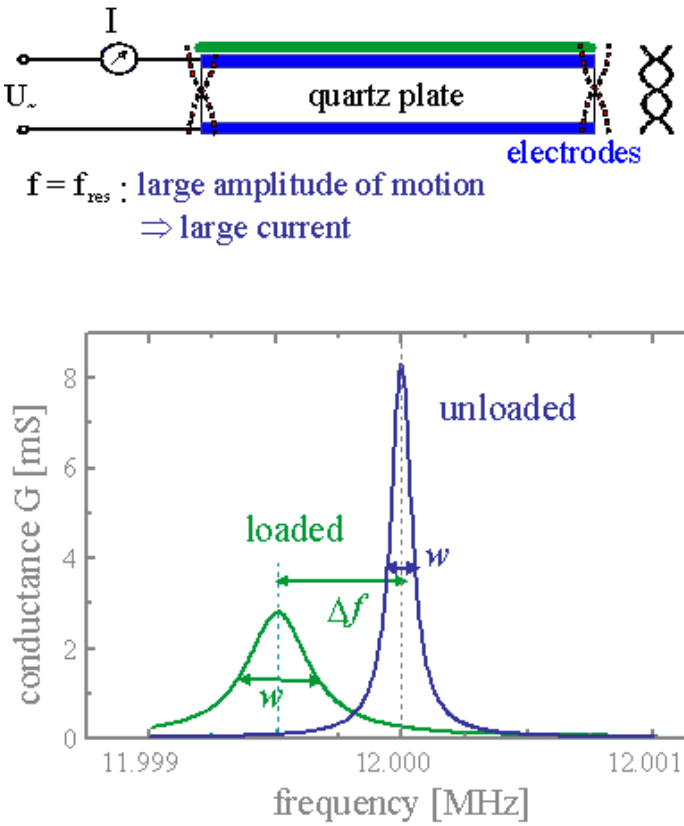

Figure 1-3 (top) - Schematic of quartz crystal microbalance (QCM) where the green area is an added mass to the surface. (bottom) - Decrease in resonance frequency and quality on addition of mass to surface.

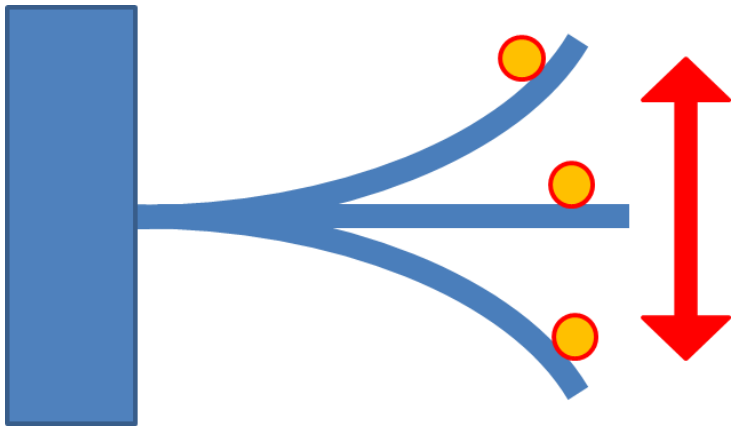

Figure 1-4 - Microcantilever resonant sensor. Vibration frequency changes with mass on surface.

Chemical sensors that utilize the resonance frequency of physical vibrations include quartz crystal microbalance (QCM), illustrated in Figure 1-3, as well as surface acoustic wave (SAW), and a variety of other micro-electro-mechanical sensors (MEMS), such as microcantilevers, pictured in Figure 1-4. (Quartz Crystal Microbalance Arrays, 2009) (Boisen, Dohn, Keller, Schmid, & Tenje, 2011) (Grate, 2000) (Ballantine & Wohltjen, 1989) (Zougagh & Rios, 2009) (Campbell & Mutharasan, 2007) These devices are constructed from piezoelectric materials, undergoing physical deformation with an applied voltage. By applying an oscillating voltage to the device, physical vibration and resonance will be observed when the driving frequency of the voltage matches the natural resonance frequency of the device. This type of resonator can be approximated by a simple harmonic oscillator, which itself can be approximated as a spring with a mass attached, as in Figure 1-5, whose natural resonance frequency is determined by Equation 1-1 or Equation 1-2 for angular or normal frequency, respectively. In these equations, k provides the restoring elastic force and is sometimes referred to as the 'spring constant' if the simple harmonic oscillator is imagined as a spring with a mass attached. Also, m represents the mass, and resulting inertial force, and is shown to be inversely related to resonance frequency. (Nave, 2012) In a chemical sensor, a mass change, and therefore a resonance frequency shift, will result from analytes adsorbing on the surface of the device. Various surface modifications are used to selectively control the chemical or biological analytes that adsorb to the sensor surface. (Zougagh & Rios, 2009)

Figure 1-5 - Simple harmonic oscillator visualized as a spring with an attached mass.

Equation 1-1

$$\omega_0 = \sqrt{\frac{k}{m}}$$

Equation 1-2

$$f_0 = \frac{1}{2\pi}\sqrt{\frac{k}{m}}$$

Optical resonance occurs where reflected, superimposed rays of light build intensity through constructive interference. (Fan, Advanced Photonic Structure for Biological and Chemical Detection, 2009) In an optical device, the resonance is a result of overlapping constructive wavelengths within a particular physical path length, so for this reason, optical ring resonators are more commonly expressed in terms of a resonance wavelength rather than frequency.

A variety of chemical sensors based on optical resonance exist. Some of the most common devices are based on cavity ring-down, Fabry-Perot cavities, or optical ring resonators, represented in Figures 1-6, 1-7, and 1-8, respectively. (Berden & Engeln, 2009) (Barone, 1963) (Fan X. , White, Zhu, Suter, & Oveys, 2007)

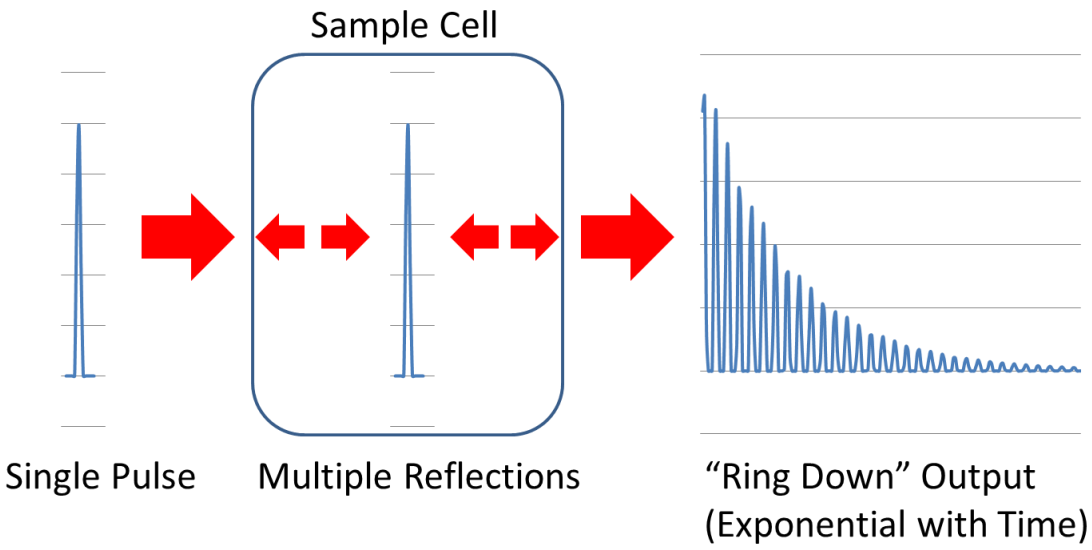

Figure 1-6- Basic principle of cavity ring down spectroscopy

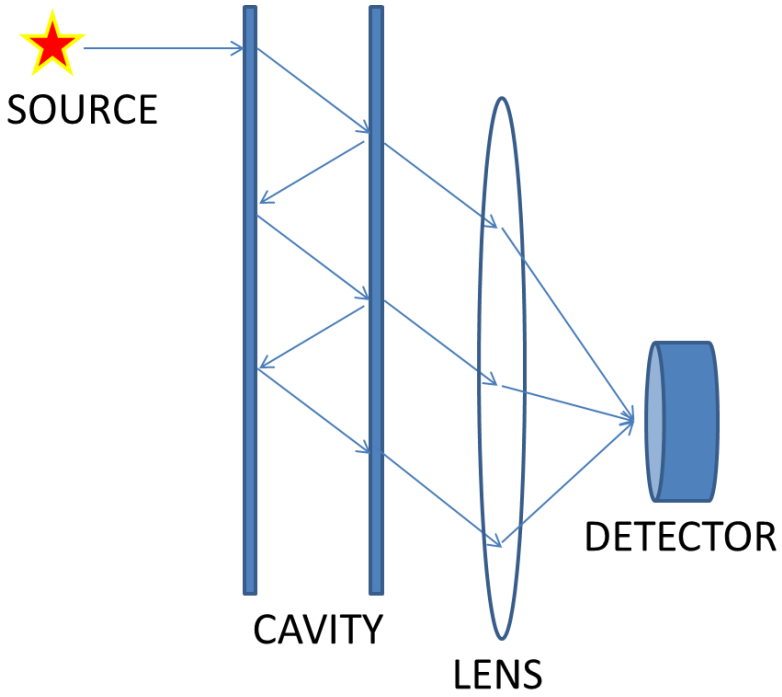

Figure 1-7 - Fabry-Perot cavity. Constructive and destructive interference is accomplished through multiple reflections in the cavity.

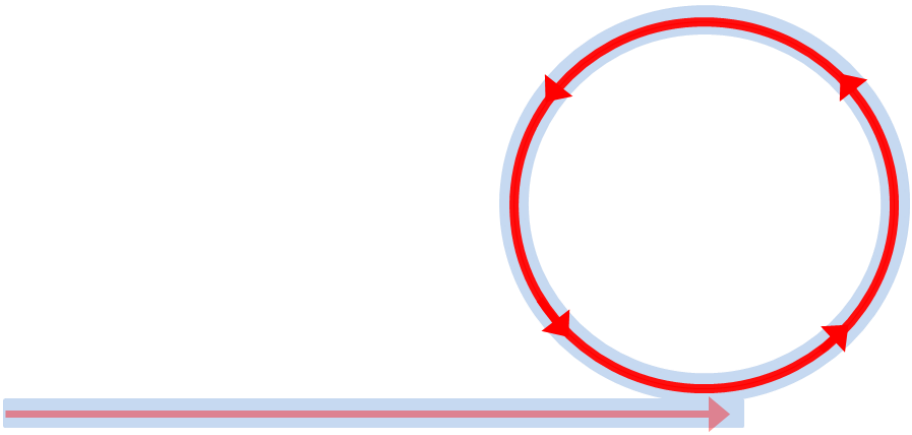

Figure 1-8 - Optical ring resonator. A building of optical intensity is achieved by overlapping constructive wavelengths.

In cavity ring-down (CRD) spectroscopy, a sample cavity is constructed with a partially reflective mirror. As resonance builds in the cavity from constructive interference, this light reflects repeatedly off of the partially reflective mirror. By then turning off the light source, the decay in light intensity can be measured temporally from what escapes the partially reflective mirror on each reflection pass. This process is illustrated in Figure 1-6.

Fabry-Perot sensors, as well as other interferometric devices, also rely on the resonance produced in a cavity. Although many variations exist, in typical operation of these devices the resonance is achieved and then the light path is split into a reference and sample channel. When the two channels are recombined and sent to the detector, any change to the conditions that alter the phase speed of light in the sample channel relative to the reference channel will be observed in the output signal. This change can be produced by various sample properties such as refractive index and temperature. (Deng, et al., 2010) (Rao & Liao, 2007) Shown in Figure 1-7 is a schematic of a Fabry-Perot interferometric system, along with simulated and simplified signals at each step.

Ring resonators are based on the constructive interference of light as it makes successive trips around a circular path. They will be discussed in much greater detail in the following section.

Optical Ring Resonators

High in the central dome of St. Paul's Cathedral in London, there is a room known as the Whispering Gallery. The room is a 34 m diameter circle where softly spoken words on one side of the gallery will reflect of the walls and reach a listener on the opposite side, despite no detectable words being heard anywhere in the center of the room. This was the location where whispering gallery waves, consequentially named, were studied by Lord Rayleigh over a century ago. (Rayleigh, 1910)

If the walls of St. Paul's Cathedral were polished to a perfect mirror finish, one could expect not only sound but also a light source to reflect around the Whispering Gallery to an observer on the other side. The term "whispering gallery mode" has been adopted in the field of optics to describe a propagating mode where, in the same manner as voices in the Whispering Gallery, the ray of light is guided by reflection off of the wall of a circular cavity. (Vollmer & Arnold, 2008) (Arnold, Khoshsima, Teraoka, Hollser, & Vollmer, 2003)

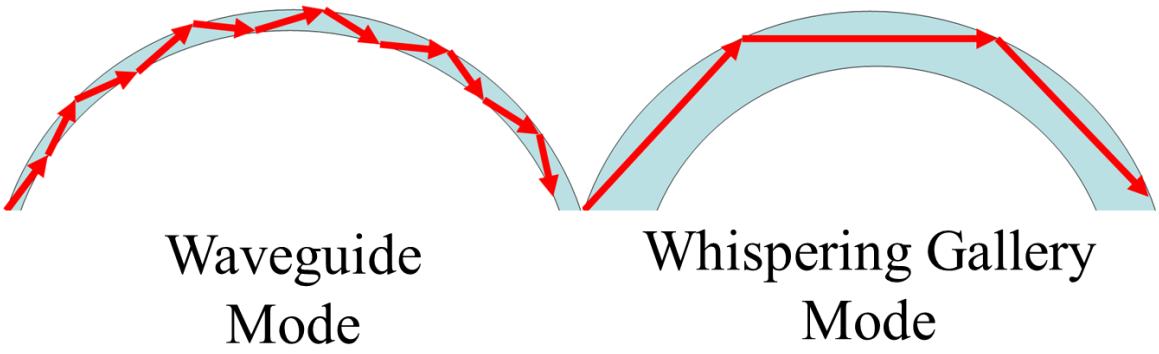

Figure 1-9 - Whispering gallery mode vs. waveguide mode.

If the area of the Whispering Gallery were mostly taken away by a smaller circular room, leaving a large, narrow, circular hallway with mirrored walls, the light would be guided to the observer by reflection off of both the inner and outer wall surfaces. The light propagation in this case is not referred to as a whispering gallery mode, but rather as a "waveguide mode," as reflection off of multiple surfaces is characteristic of waveguides, such as optical fibers for example. (Suter & Fan, Handbook of Optofluidics, 2010) (Oates & Burgess, 2012) The differences between the two types of circular modes will be discussed in more depth later; however Figure 1-9 is shown to give a simple illustration of the two types of modes.

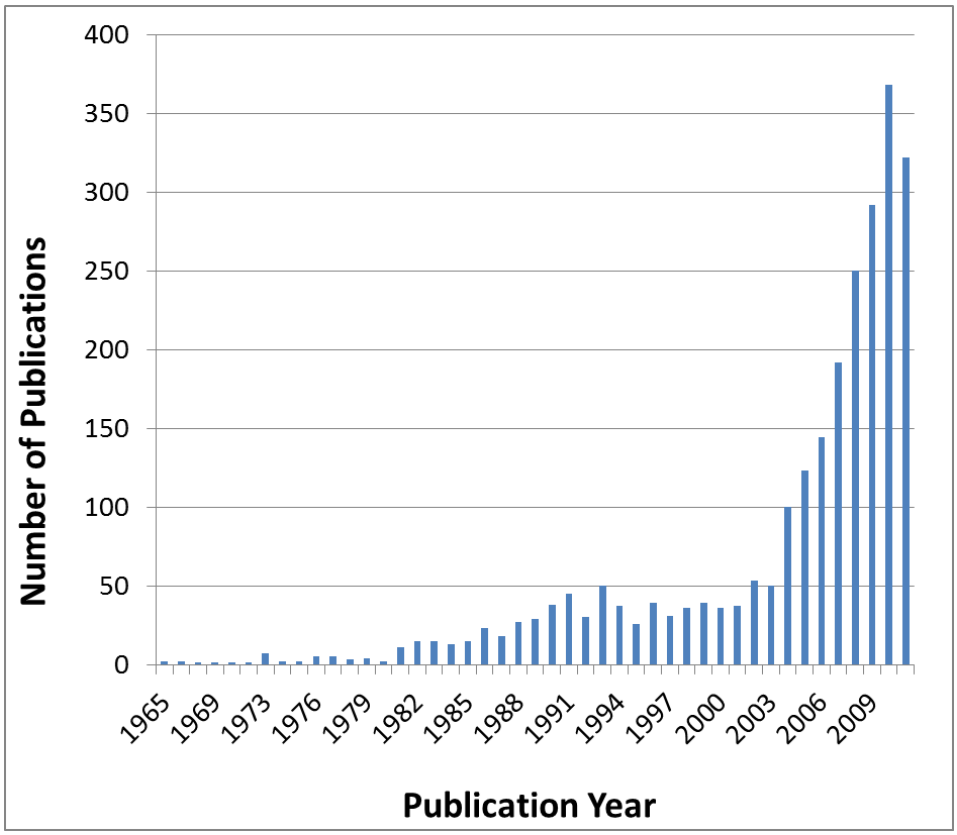

Figure 1-10 - Number of publications with a title containing "Ring Resonator" per year.

As chemical sensors, ring resonators have emerged in just the past 15-20 years. This parallels the dramatic increase of overall interest in ring resonators, shown in Figure 1-10, where the term “Ring Resonator” was searched in the Scifinder Scholar database and the number of matching publications was plotted against publication year. (Scifinder Scholar Database, 2012) Prior to being studied in chemical sensing, ring resonators were primarily studied in the field of laser optics, for their unique form as resonant cavity. (Bridges & Rigrod, 1965) (Garrett, Kaiser, & Bond, 1961) Illustrated in Figure 1-11 is a ruby ring resonator, shown by Roess and Geher in 1964. (Roess & Gehrer, 1964) From this device, they observed interference fringes. While this very early ring resonator was, in fact, based on total internal reflection, some early publications

using the term “ring resonator” were simply referring to a four-sided mirrored cavity, as shown in Figure 1-12. (Ezekiel & Balsamo, 1977) Dating back to 1913, Hermann discussed the concept of circular resonance in the context of electrons in the photoelectric effect. (Herrmann, 1913)

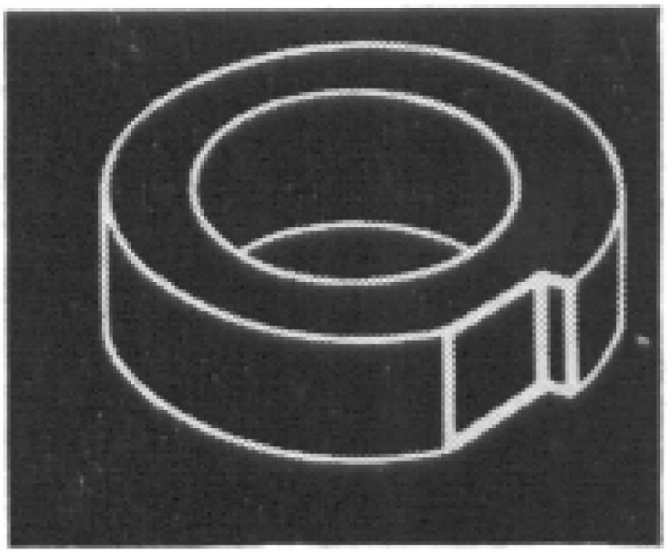

Figure 1-11 - Ruby ring resonator presented by Roess and Gehrer in 1964. (Copyright 1964 IEEE)

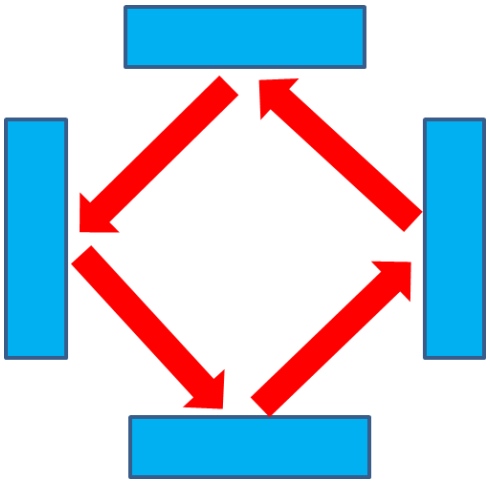

Figure 1-12 - Ring resonator based on four mirrors

Ring Resonator Formats

Chemical sensors based on ring resonators have been demonstrated in a variety of geometries, each with its own advantages and disadvantages. The most common include microsphere, planar (or micro-fabricated), and liquid core (or capillary-based).

Microsphere resonators have been shown to have the potential to resonate with higher quality than resonators of other geometries. (Fan, Advanced Photonic Structure for Biological and Chemical Detection, 2009) This is due to the exceptionally smooth and spherical surface produced by microsphere construction methods. These methods typically produce the microsphere as a suspended bead of glass from a melted optical fiber. The limitations of microsphere resonators come in its somewhat limited potential for real-world use outside of research. Precisely aligning a light source to couple into a microsphere can be challenging, and the format is not as well suited to microfluidic installations as other ring resonator geometries. Illustrated in Figure 1-13 is a schematic of a microsphere ring resonator system with the inset showing representative data, as a transmission dip of the through port (end of fiber used for coupling into the resonator) at a resonant wavelength. (Vollmer & Arnold, 2008)

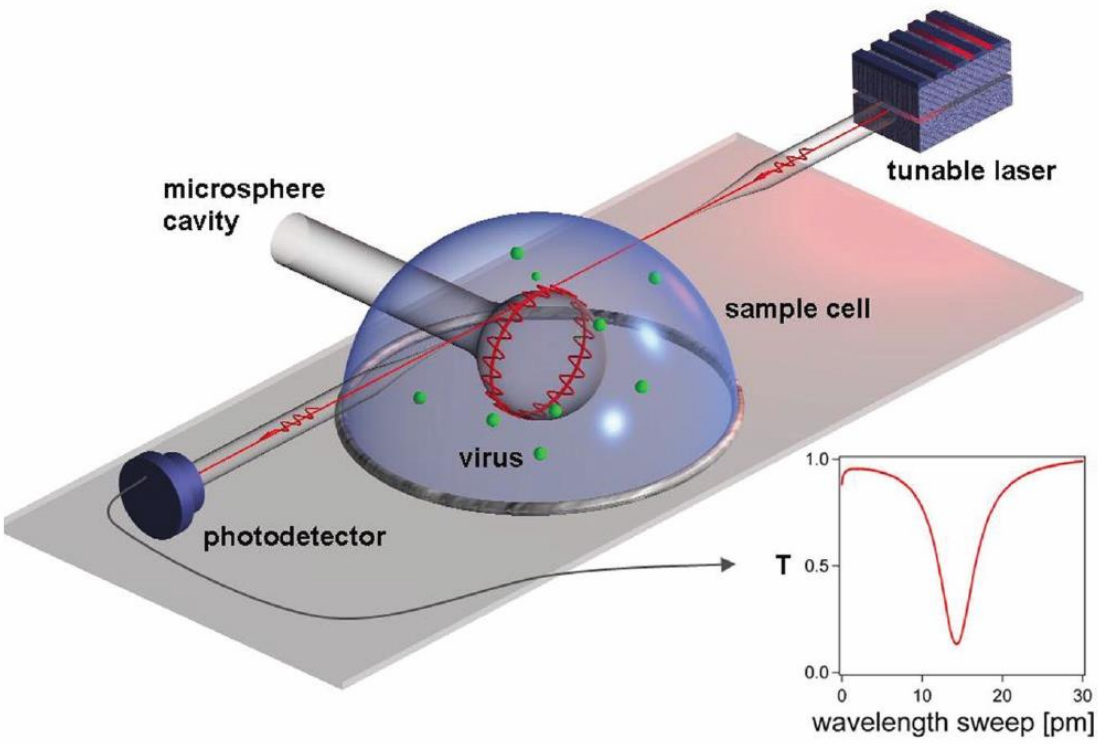

Figure 1-13 - Microsphere ring resonator with inset of resulting transmission data, shown by Vollmer & Arnold. (Copyright 2008, National Academy of Sciences, U.S.A.)

Shown in Figure 1-14, planar ring resonator fabrication is typically based on lithographic etching processes. (Chao, Fung, & Guo, 2006) (Yalcin, et al., 2006) (Kim, et al., 2010) (Fan, Advanced Photonic Structure for Biological and Chemical Detection, 2009) This naturally makes mass-production a real possibility. With mass-production comes the significant benefit of lower unit cost, potentially to the point of being disposable. The limitation with micro-fabricated ring resonators is in the same etching process that makes the devices cost-effective. This process produces a rough surface, when compared with a microsphere glass bead for example, and therefore resonator quality is somewhat limited. (Scholten, Fan, & Zellers, 2011)

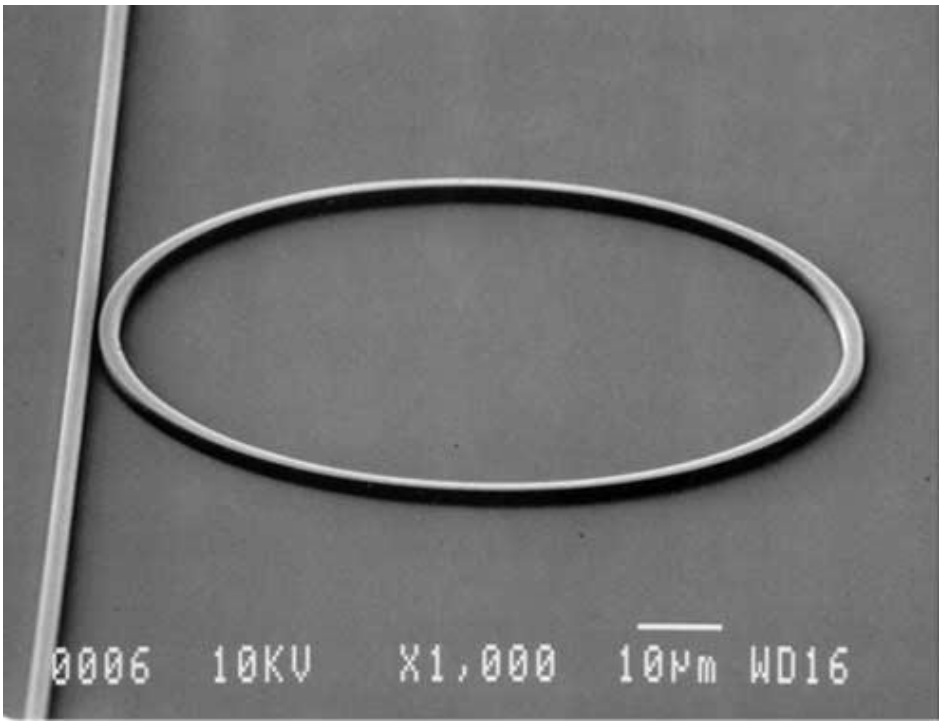

Figure 1-14 – Scanning electron microscopy image of polystyrene microfabricated ring resonator, shown by Chao, Fung, and Guo. Copyright 2006 IEEE.

Liquid core optical ring resonators (LCORR) are generally constructed in the wall of a capillary. The sample being analyzed is located on the inside of the capillary, thus making this format well suited for easy integration into microfluidic systems. Fan and coworkers have pioneered the LCORR in recent years, demonstrating a variety of potential applications. (Fan X. , White, Zhu, Suter, & Oveys, 2007) (Fan X. , White, Zhu, Suter, & Sun, 2008) (White, Oveys, & Fan, 2006) (Suter J. , White, Zhu, & Fan, 2007) (Suter J. , et al., 2008) Using a combination of heating, pulling, and chemical etching, they have produced LCORRs with quality nearly as high as typical microsphere resonators. Illustrated in Figure 1-15 is a capillary-based LCORR with DNA-capturing surface chemistry, and on right is a more complete schematic including temperature control. (Suter J. , et al., 2008)

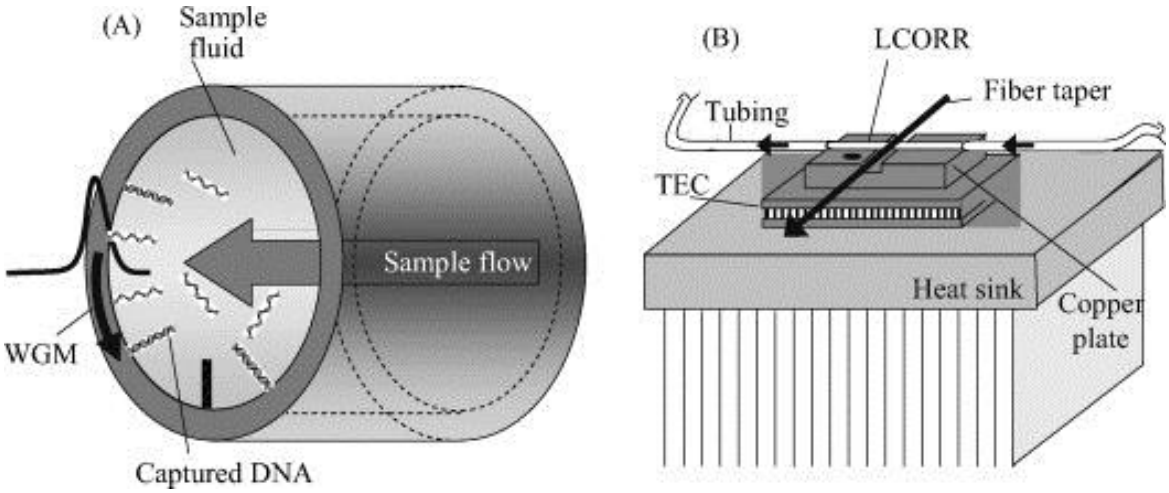

Figure 1-15 – (Left) Cross-sectional diagram of an individual LCORR sensor. (Right) Side view of the experimental setup. Reprinted from Biosensors and Bioelectronics, 23, 7, Suter, et al., "Label-free quantitative DNA detection using the liquid core optical ring resonator," Pages 1003-1009, Copyright 2008, with permission from Elsevier.

Mentioned earlier, the difference between whispering gallery modes and waveguide modes was analogous to the reflection around the walls of an open whispering gallery room, and reflection down both walls of a narrow hallway, respectively. If the "hallway" were sufficiently wide, the reflection could simply take place off of the outer wall. It should be emphasized the optical guiding in a ring resonator is based on internal reflection rather than external reflection, as would be the case in the Whispering Gallery room used in the analogy. Illustrated in Figure 1-9, before the capillary wall is sufficiently thinned, the modal profile for a capillary-based ring resonator is dominated by WGMs that have no interaction with the inner surface. In other words, without sufficient thinning, a liquid core resonator will have the same modal profile as a microsphere resonator or any other solid core resonator. As the analyte to be detected in an LCORR is in the core of the capillary, thinning clearly becomes a critical factor.

The limitations of LCORRs come in the fabrication process. Thinned walls can become very fragile. (Scholten, Fan, & Zellers, 2011) Therefore, the pulling and etching of capillaries requires

great care and precision. This applies, perhaps even more, to the handling of the thinned capillaries during installation and operation. In this work, the LCORR format was chosen primarily for both the ease of fluidics integration, as the device is already fashioned on a capillary, and simplicity of operation.

Ring Resonator Coupling Schemes

For the identification of resonance wavelengths, two general approaches are taken. In one, the loss in transmission through a waveguide is measured, where these resonance wavelengths are coupled out of the waveguide and into the ring resonator. Another method relies on intensity at resonant wavelengths being picked up from a "drop" port on the other side of the ring resonator. The difference in these two approaches is illustrated in Figure 1-16. (Yupapin, Saeung, & Li, 2007) (Sambaraju, et al., 2010) (Fan, Advanced Photonic Structure for Biological and Chemical Detection, 2009)

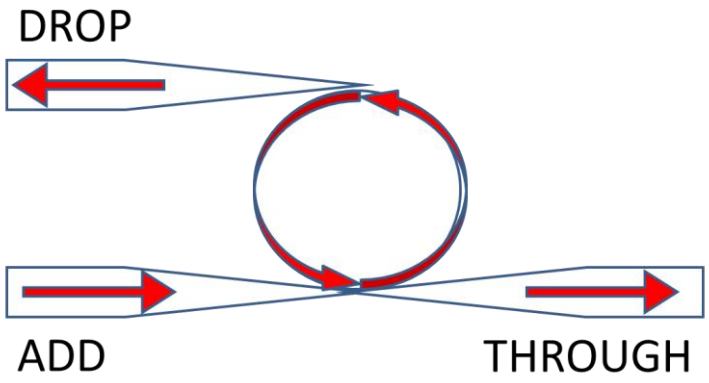

Figure 1-16 - Coupling light into a ring resonator using tapered optical fibers. The light is introduced through the 'ADD' port, and the output can be measured either through the 'DROP' port (as a resonant transmission peak) or 'THROUGH' port (as a loss in transmission at resonance).

Coupling light into ring resonators can be accomplished in a variety of ways. Shown in Figure 1-17 some of the most common methods include a prism, a beveled fiber, and tapered fibers. (Oates & Burgess, 2012) For this work, coupling based on Figure 1-17 (D) was developed, with input and output (drop) fiber tapers placed on opposite sides of the capillary. This method was chosen not only for its simplicity of construction and positioning, but also to maximize the amount of light being detected that has interacted with the ring resonator. In other words, when compared to other schemes, such as that presented in Figure 1-17 (C), the amount of light that has simply passed through the fiber without interaction with the ring resonator is minimized. This was found to be helpful in allowing absorption detection to be taken with the device described later in this work, in addition to refractive index. (Oates & Burgess, 2011)

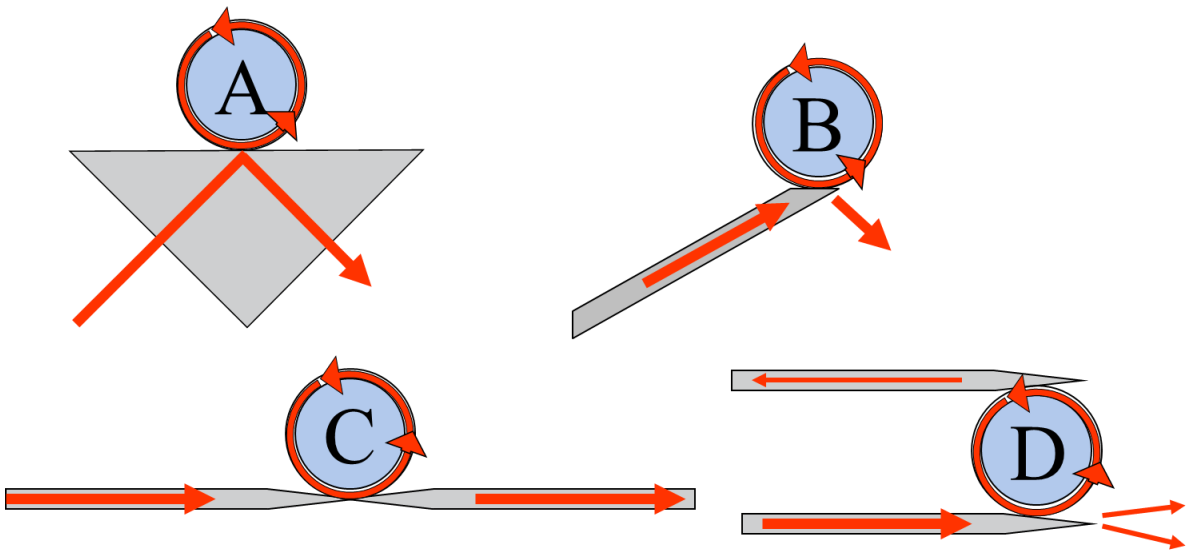

Figure 1-17 - Several ring resonator coupling schemes: (A) prism, (B) beveled fiber, (C) tapered fiber, and (D) tapered fiber ends.

Ring Resonator Basic Theory

In ring resonator sensors, where the physical radius is much longer than the optical wavelength, a resonant wavelength can be approximated by Equation 1-3. In this equation, r is the average radius of the resonator, n_{eff} is the effective refractive index, m is an integral number, and λ is the resonant wavelength. L_{opt} is a factor relative to the optical path length to account for the zig-zag propagation in multimode waveguides, illustrated in Figure 1-18. (Daly, 1984) Therefore, L_{opt} ranges from 1 for the minimum mode, taking the shortest possible ray path, to n_1/n_2 for rays propagating at the critical angle. Note that n_1 is the RI of the waveguide material, n_2 is the RI of the material external to the reflecting surface, and this ratio is approximately 1.09 for visible light at a fused silica/water interface.

Equation 1-3

$$\lambda = \frac{2\pi r L_{opt} n_{eff}}{m}$$

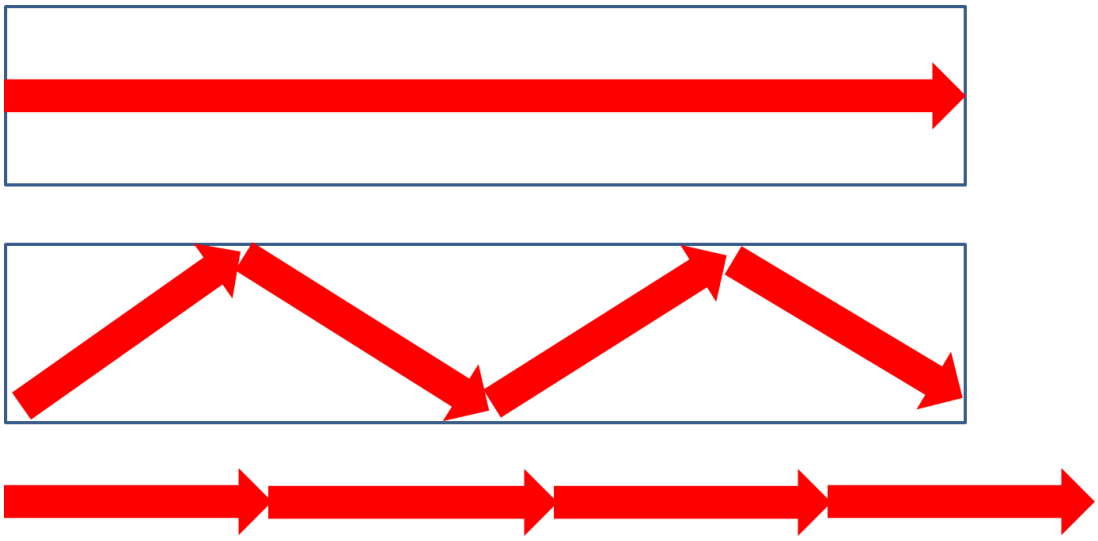

Figure 1-18 – Ray propagation through a waveguide at the lowest possible mode (top) travels the shortest possible distance. Contrary to this, the ray travelling a 'zig-zag' path at the critical angle travels a longer overall distance.

In Equation 1-3, it can also be seen that, with the physical dimensions fixed, the primary dynamic variable is the refractive index, expressed as n_{eff}, or effective refractive index. This term is defined in Equation 1-4 and takes into account the fraction of light that evanescently penetrates beyond the reflecting surface, into the lower RI material(s).

Equation 1-4

$$n_{\text{eff}} = n_{\text{out}}\eta_{\text{out}} + n_{\text{wall}}\eta_{\text{wall}} + n_{\text{core}}\eta_{\text{core}}$$

In Equation 1-4, η_{out},η_{wall}, and η_{core} are the fractions of the resonating guided light present outside the resonator material, in the resonator material, and inside the resonator core, respectively. (Zhu, White, Suter, Dale, & Fan, 2007) In the case of a microsphere resonator, or any solid resonator employing only outer surface detection, the n_{core} term would be neglected. The evanescent field depth of penetration, d_p, is defined in Equations 1-5 and 1-6, and the field strength, E, is 1/e of original at a distance of d_p into the lower RI material according to Equation 1-6. (Harrick, 1979)

Equation 1-5

$$d_{\text{p}} = \frac{\lambda}{2\pi n_1[\sin^2\theta - \left(\frac{n_2}{n_1}\right)^2]^{1/2}}$$

Equation 1-6

$$E = E_0 \text{e}^{-z/d_{\text{p}}}$$

In Equation 1-5, θ is defined as the angle between the incident ray and normal to the reflecting interface. Also, n_1 and n_2 are the RI of the higher and lower RI materials, respectively. In the case of an LCORR, the circulating modes are guided by both the inner and outer wall of the capillary, and thus n_2 could represent either n_{out} or n_{core}. With a change in n_{core}, such as with the introduction of an analyte, the n_{eff} term in Equation 1-4 will not only be affected by the n_{core} term

but also the relative field fractions η_{core} and η_{wall}, as Equations 1-5 and 1-6 predict a relationship between $n_{2/}$ n_1 and evanescent field penetration depth.

References

Arnold, S., Khoshsima, M., Teraoka, I., Hollser, S., & Vollmer, F. (2003). *Opt. Lett., 28*, 272-274.

Ballantine, D., & Wohltjen, H. (1989). *Anal. Chem., 61*, 704-715.

Barone, S. (1963). *J. Appl. Phys., 34*, 831-843.

Berden, G., & Engeln, R. (2009). *Cavity Ring-down Spectroscopy: Techniques and Applications.* Chichester, U.K.: Wiley.

Boisen, A., Dohn, S., Keller, S., Schmid, S., & Tenje, M. (2011). *Rep. Prog. Phys., 74*, 036101.

Bridges, T., & Rigrod, W. (1965). *IEEE J. Quantum Electron., 1*, 303-308.

Campbell, G., & Mutharasan, R. (2007). *Anal. Chem., 79*, 1145-1152.

Chao, C., Fung, W., & Guo, L. (2006). *IEEE. J. Sel. Top. Quantum Electron., 12*, 134-142.

Daly, J. (1984). *Fiber Optics.* Boca Raton: CRC Press, Inc.

Davis, W. (2010). *Radio Frequency Circuit Design.* Hoboken: John Wiley & Sons, Inc.

Deng, M., Tang, C., Zhu, T., Rao, Y., Xu, L., & Han, M. (2010). *Appl. Opt., 49*, 1593-1598.

Ezekiel, S., & Balsamo, S. (1977). *Appl. Phys. Lett., 30*, 478-480.

Fan, X. (2009). *Advanced Photonic Structure for Biological and Chemical Detection.* Dordrecht: Springer.

Fan, X., White, I. S., Zhu, H., Suter, J., & Sun, Y. (2008). *Anal. Chim. Acta., 620*, 8-26.

Fan, X., White, I., Zhu, H., Suter, J., & Oveys, H. (2007). *Proc. SPIE*, 6452-18.

Garrett, C., Kaiser, W., & Bond, W. (1961). *Phys. Rev., 124*, 1807-1809.

Grate, J. (2000). *Chem. Rev., 100*, 2627-2648.

Harrick, J. (1979). *Internal Reflection Spectroscopy.* Ossining: Harrick Scientific Corporation.

Herrmann, K. (1913). *Ber. physik. Ges., 14*, 1836-1837.

Johnston, I. (2009). *Measured Tones: The Interplay of Physics and Music.* Boca Raton: CRC Press.

Kim, G., Lee, H., Park, C., Lee, S., Lim, B. B., & Lee, W. (2010). *Opt. Express, 18*, 22215-22221.

Nave, R. (2012). *Simple Harmonic Motion Frequency*. Retrieved from Hyperphysics: http://hyperphysics.phy-astr.gsu.edu/hbase/shm2.html

Oates, T., & Burgess, L. (2011). *Appl. Spectrosc., 65*, 1187-1192.

Oates, T., & Burgess, L. (2012). *Anal. Chem., 84*, 7713-7720.

Quartz Crystal Microbalance Arrays. (2009). Retrieved from Sandia National Laboratories: http://www.sandia.gov/mstc/MsensorSensorMsystems/documents/Quartz-QCM.pdf

Rao, Y., & Liao, Y. (2007). *Proc. of SPIE, 6830*, 683021.

Rayleigh, L. (1910). *Philos. Mag., 20*, 1001-1004.

Roess, D., & Gehrer, G. (1964). *Proc. IEEE*, 1359-1360.

Sambaraju, R., Galan-Conejos, J., Herrera, J., Griol, A., Oton, C., Sanchis, P., & Martinez, A. (2010). *Proc. of SPIE, 7719*, 771914.

Scholten, K., Fan, X., & Zellers, E. (2011). *Appl. Phys. Lett., 99*, 141108.

Scifinder Scholar Database. (2012, 12 10). *Chemical Abstracts Service*. Columbus, OH.

Suter, J., & Fan, X. (2010). In A. Hawkins, & H. Schmidt, *Handbook of Optofluidics* (pp. 11(1-29)). Boca Raton: Taylor & Francis.

Suter, J., White, I., Zhu, H., & Fan, X. (2007). *Appl. Opt., 46*, 389-396.

Suter, J., White, I., Zhu, H., & Fan, X. S. (2008). *Biosens. Bioelectron., 23*, 1003-1009.

Vollmer, F., & Arnold, S. (2008). *Nat. Methods, 5*, 591-596.

Wang, B., & Anslyn, E. (2011). *Chemosensors.* Hoboken: Wiley.

White, I., Oveys, H., & Fan, X. (2006). *Opt. Lett., 31*, 1319-1321.

Yalcin, A., Popat, K., Aldridge, O., Desai, T., Hryniewicz, J., Cbouki, N., . . . King, O. (2006). *IEEE J. Sel. Top. Quantum Electron., 12*, 148-155.

Yupapin, P., Saeung, P., & Li, C. (2007). *Opt. Commun., 272*, 81-86.

Zhu, H., White, I., Suter, J., Dale, P., & Fan, X. (2007). *Opt. Express, 15*, 9139-9146.

Zougagh, M., & Rios, A. (2009). *Analyst, 134*, 1274-1290.

Zourob, M., & Lakhtakia, A. (2010). *Optical Guided-wave Chemical and Biosensors I.* New York: Springer.

CHAPTER 2

Absorption Detection

Introduction

The ring resonator devices introduced in Chapter 1 are most commonly configured for refractive index sensing. As internally reflected light always exists with a small fraction of light evanescently penetrating into the external material at each reflection point, a ring resonator should inherently be a surface absorption sensor. While a conventional method for resonant device analysis would track a single resonance wavelength, this would provide only limited information, spectrally, about possible chromophores present. (Arnold, et al., 2009) (Boleininger, Lake, Hami, & Vallance, 2010) (Fan X. , White, Zhu, Suter, & Oveys, 2007) (Fan X. , White, Zhu, Suter, & Sun, 2008) (Fan, Advanced Photonic Structure for Biological and Chemical Detection, 2009) (Iqbal, et al., 2010) (Leidner, Zourob, & Lakhtakia, 2010) (Shopova, et al., 2008) (Suter J. , White, Zhu, & Fan, 2008) (Suter & Fan, Handbook of Optofluidics, 2010) (Zhu, White, Suter, Dale, & Fan, 2007) By introducing a broad spectrum of light into a ring resonator, a multitude of resonant wavelengths should be possible, allowing a sufficiently complete spectrum. (Oates & Burgess, 2011)

History and Background

In 1671, Sir Isaac Newton first described the presence of what are now known as evanescent waves. (Newton, 1671) Pictured in Figure 2-1, the interface at a point of total internal reflection includes an interference pattern from incoming and reflected rays, as well as the evanescent field, exponentially decaying beyond the interface. Attenuation total (internal) reflection spectroscopy (ATR), based on the absorption of the evanescent field, has found a niche in industrial process sampling. (Blum & John, 2011) (Chai, Li, & Zhu, 2002) (Chai, Hou, & Verrill,

2005) (Billot, Couty, & Hosek, 2010) (Doyle & Tran, 1999) (Howard, et al., 2009) A variety of biological sensors have also been developed based on evanescent field absorption and/or excitation. (Zourob & Lakhtakia, 2010) (Simhi, Gotshal, Bunimovich, Sela, & Katzir, 1996) (Steiner & Renschen, 1992)

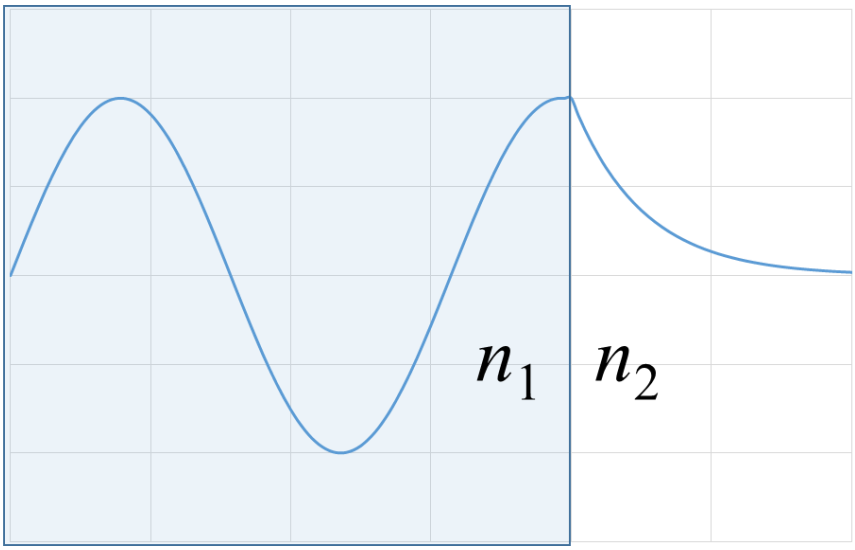

Figure 2-1 - The electric field at the point of total internal reflection includes both a standing wave due to interference between incoming and reflected rays, as well as an exponentially decaying evanescent field into the lower refractive index material.

The mechanism of detection in ring resonators is most commonly refractive index shifting caused by analytes within the evanescent field at the resonator surface. (Fan X. , White, Zhu, Suter, & Oveys, 2007) (Fan X. , White, Zhu, Suter, & Sun, 2008) Therefore, it would be expected that a ring resonator is also well suited for absorption detection for chromophoric analytes at the resonator surface. In most conventional ring resonator applications, however, only a single wavelength is utilized, and for absorption measurements, the intensity loss of a single wavelength would not be particularly useful.

Tarsa, et al. realized the possibility of broad absorption detection, and modified their experiments to observe an overtone absorption band of 1-octyne, which was located in the wavelength range of a tunable communications laser. (Tarsa, Rabinowitz, & Lehmann, 2003) Using the tunable laser source, they scanned across several resonance wavelengths, shown as peaks in Figure 2-2 and constructed a pseudo-absorption spectrum. Note that their ring resonator was considerably larger in diameter than most ring resonator work, and the intensity is actually measured as a ring-down time, based on cavity-ring down spectroscopy techniques, discussed in Chapter 1.

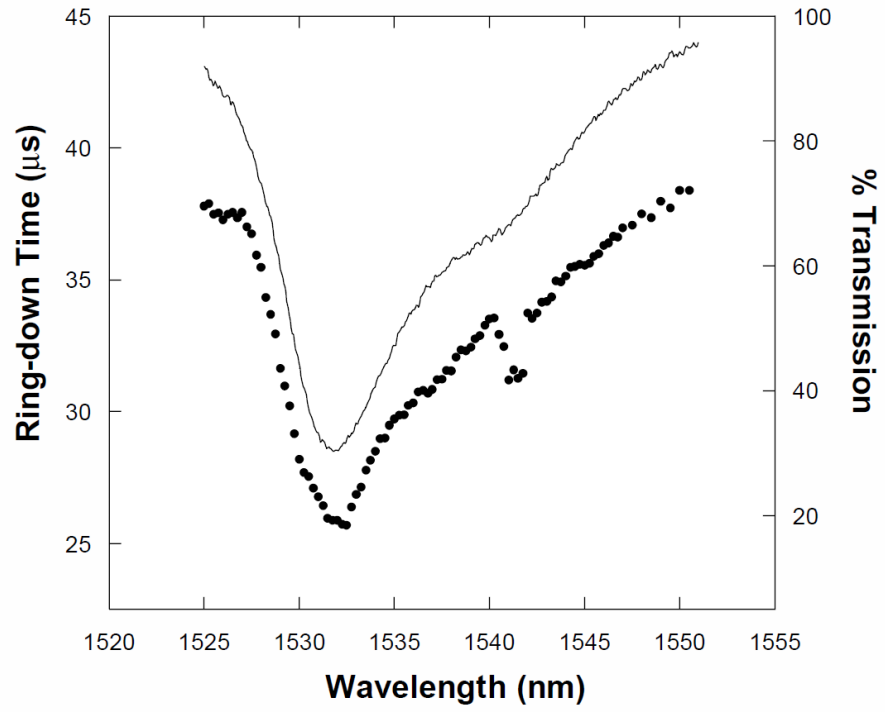

Figure 2-2 - Cavity ring down spectrum compared to a standard transmission measurement. Reproduced with permission. (Copyright 2004 Elsevier)

In calculating a resonance wavelength using Equation 1-3, *m* represents integral numbers. If the rest of the equation were plugged in with the dimensions of a typical ring resonator with a diameter of 250 μm, the *m* values for the visible region of light, for example, would be on the order

of 2000, and the spacing between resonant wavelengths would be on the order of 0.2 nm. What this implies is that a fairly complete spectrum, for the use of broadband absorption measurements, should be available in the case where a broadband source is coupled into a ring resonator.

Westcott, et al. took advantage of the multiple potential resonance wavelengths by launching a white LED into the whispering gallery modes of a microsphere resonator. (Westcott, et al., 2008) The group was able to observe enhanced absorbance levels for dyes that exhibit a strong affinity to the resonator surface. Methylene blue, as a cationic dye, is attracted to the negative charges present at a bare silica surface when in a neutral aqueous environment. (Heger, Jirkovsky, & Klan, 2005) (Tsunoda, Itabashi, & Akaiwa, 1992) (Tsunoda, Umemura, Ueno, Okuno, & Akaiwa, 2003) (Umemura, Kasuya, Odake, & Tsunoda, 2002) This is illustrated in Figure 2-3. Additionally, the group looked at surface functionalization and the corresponding effects on relative absorbance. The work demonstrated the feasibility of broadband absorbance measurements in a ring resonator, and also confirmed the expectation that the absorption being measured is that of the evanescent field near the surface.

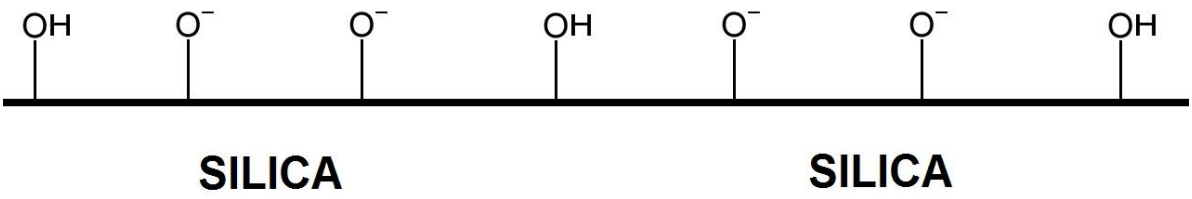

Figure 2-3 – At increasing pH, starting a pH around 2, negatively charged oxygen become increasingly abundant relative to the silanol groups at a silica surface.

To demonstrate the feasibility of taking broadband absorbance measurements in a liquid core optical ring resonator, a proof of concept device was constructed from a 250 μm ID fused silica capillary. In Beer's Law, Equations 2-1 and 2-2, the absorbance value is defined to be a

logarithmic function of the relative transmission loss. (Skoog, Holler, & Nieman, 1998) As transmission loss has a logarithmic relationship with both path length and concentration, the other form of Beer's law is expressed in Equation 2-2. In more intuitive terms, if a path length of 1 cm allowed only 50% transmission, then adding another 1 cm cell in series would allow 50% of the remaining light to pass through, for 25% overall transmission. This is illustrated in Figure 2-4. Expressed in another way, Figure 2-5 illustrates the simulated data for both transmission and absorbance as a function of path length. From this, the logarithmic relationship is confirmed, and the resulting linear relationship between absorbance and path length is observed.

Equation 2-1

$$A = -\log(\frac{T}{T_0})$$

Equation 2-2

$$A = \varepsilon c l$$

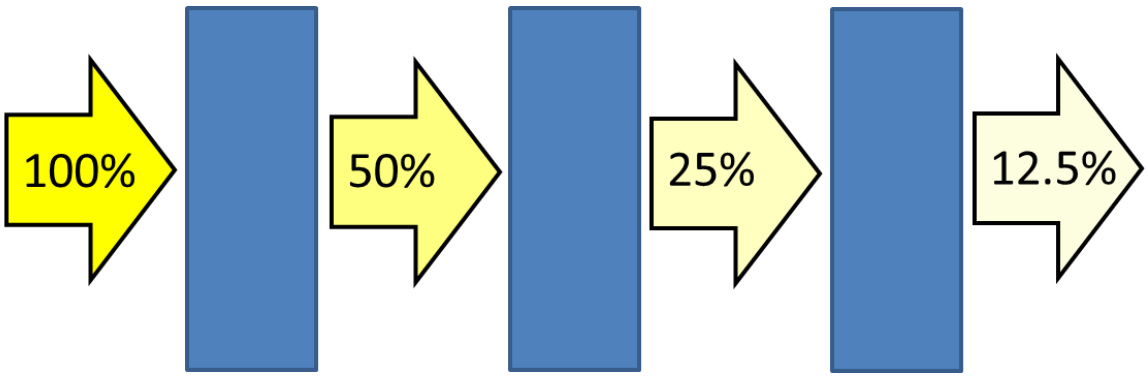

Figure 2-4 - Exponential transmission loss with increasing pathlength.

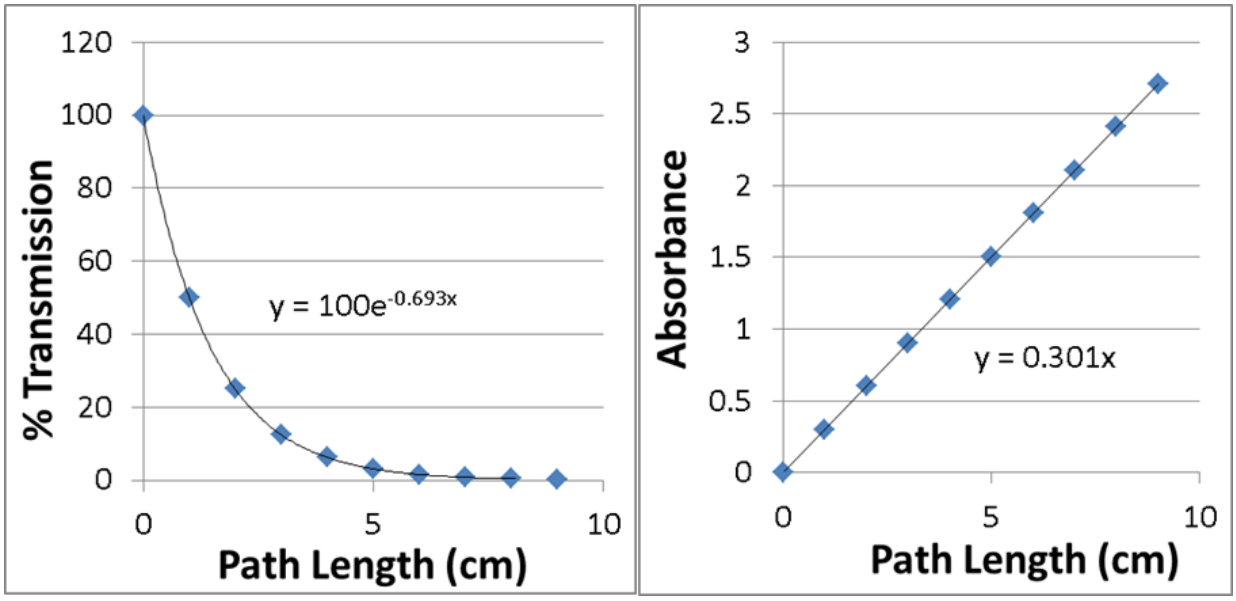

Figure 2-5 - (Left) Simulated plot of %transmission vs. path length where a 1cm path length allows 50% transmission. (Right) Plot of absorbance vs. path length of the same data produces a linear slope.

In traditional absorption measurements, a collimated beam of light is sent though a sample cell of known path length. By doing so, it can be assumed that every photon being detected has travelled through the sample cell, and has had the opportunity to become absorbed by a corresponding chromophore of sufficient concentration. When attempting absorption measurements in the very dissimilar format of a ring resonator, consideration must be taken for minimizing the amount of light that has not interacted with the sample- and would not under any circumstances. In Figure 1-17, the various schemes for coupling light into and out of a ring resonator were shown. As 1-17 (D) utilizes a drop port, per Figure 1-16, for measurement, it is clearly the most suitable for taking absorption measurements. This method was also found to be fairly easy to construct and install.

Experimental

A proof of concept device was constructed and is shown in Figure 2-6. A thinned capillary is epoxied to a block of poly methyl methacrylate (PMMA). A channel is carved out of the block to give clearance to the tapered optical fibers used to couple light into and out of the capillary wall. The fibers are epoxied to extension rods, secured in optical positioning mounts.

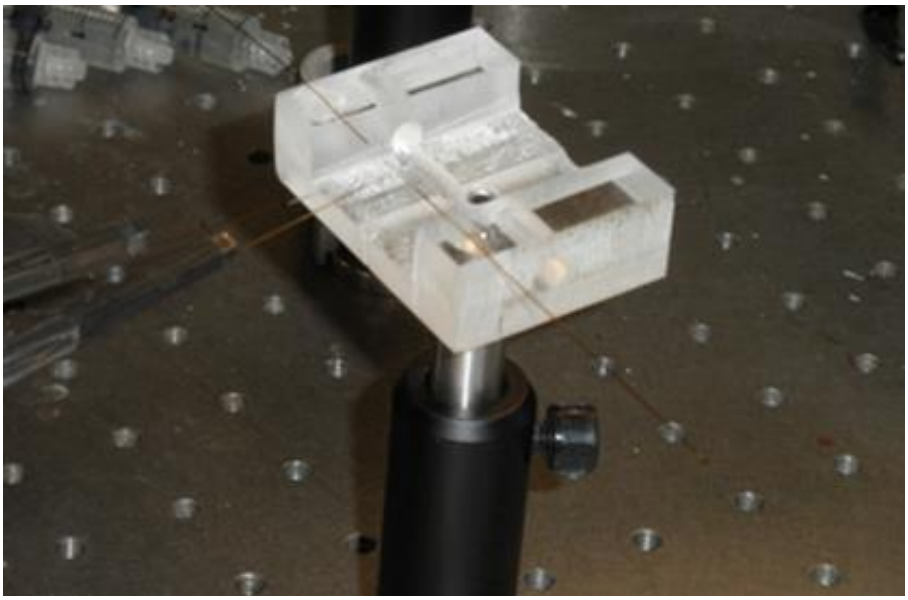

Figure 2-6 - Photo of LCORR

In Figure 2-7, the photo is taken directly overhead to show more detail in the coupling region. In this image, the capillary is pictures left to right and the illuminated fiber, shown vertically, is the input fiber. At a slight angle to this, primarily for ease of construction, is the output fiber. Note that in the Z-direction, looking into the image, the input fiber is making contact with the bottom of the capillary, whereas the output fiber is on the top of the capillary, closer in perspective to the viewer.

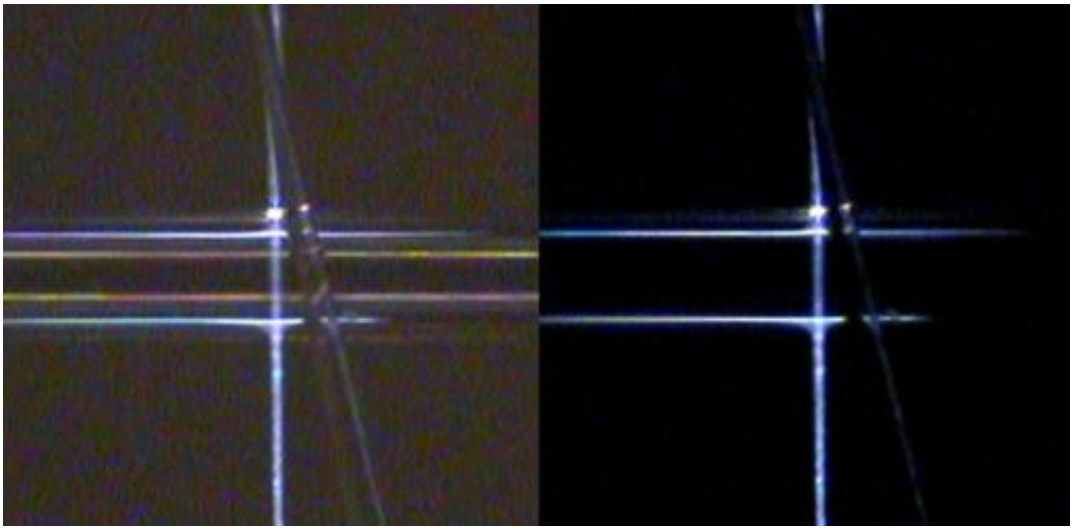

Figure 2-7 – Overhead photo of LCORR in coupling region with room lights on (Left) and off (Right).

Thinning of Capillary

In Chapter 1, it was illustrated in Figure 1-9 that light could propagate in a ring resonator in whispering gallery modes or waveguide modes. In the case of an LCORR, where sample analyte is located beyond the inner wall surface, it becomes clear that only waveguide modes are useful for evanescent absorption detection. Therefore, it becomes crucial to sufficiently maximize the relative abundance of waveguide modes. Fan and coworkers, using similar but smaller diameter LCORRs for RI detection, found that wall thickness of approximately 4 μm or less was necessary for achieving significant interaction with the sample analytes in the core. (Fan X. , White, Zhu, Suter, & Oveys, 2007) (Fan X. , White, Zhu, Suter, & Sun, 2008) (Fan, Advanced Photonic Structure for Biological and Chemical Detection, 2009) (Suter J. , White, Zhu, & Fan, 2008) (Suter & Fan, Handbook of Optofluidics, 2010)

Thinning of the capillary wall was accomplished by etching with dilute Buffer-HF (Transene Company). Both internal and external etching methods were attempted, and external etching was

found to produce a somewhat more sensitive device. More details and characterization of etch methods will be discussed in Chapter 4. For the absorption detection described in this chapter, external etching was used exclusively.

Standard 250 μm ID/360 μm OD (Polymicro technologies) fused silica capillary was used. Thinning of the wall was accomplished by first removing a 1 cm section of the polyimide protective coating by heating and charring it off with a small coil of Ni-chrome resistive wire, as illustrated in Figure 2-8. Then, the exposed section of capillary was placed in a Teflon vessel and etched with Buffer-HF. In 30 minute increments, the capillary was removed, rinsed with deionized water to halt the etching process, and its thickness was determined on a standard imaging microscope (Zeiss). The etchant was also replenished, as to maintain an excess concentration, and linear etch rate with time. From this data, presented in Figure 2-9, the estimated etch times could be determined for subsequent thinning. Therefore, to achieve wall thickness of approximately 4 μm, etch times on the order of 5-6 hours were found to be necessary. The capillary used for the absorption studies in this chapter was verified to have a wall thickness of 4 μm. Capillaries thinned much beyond this were found to be considerably fragile and difficult to use during experimentation.

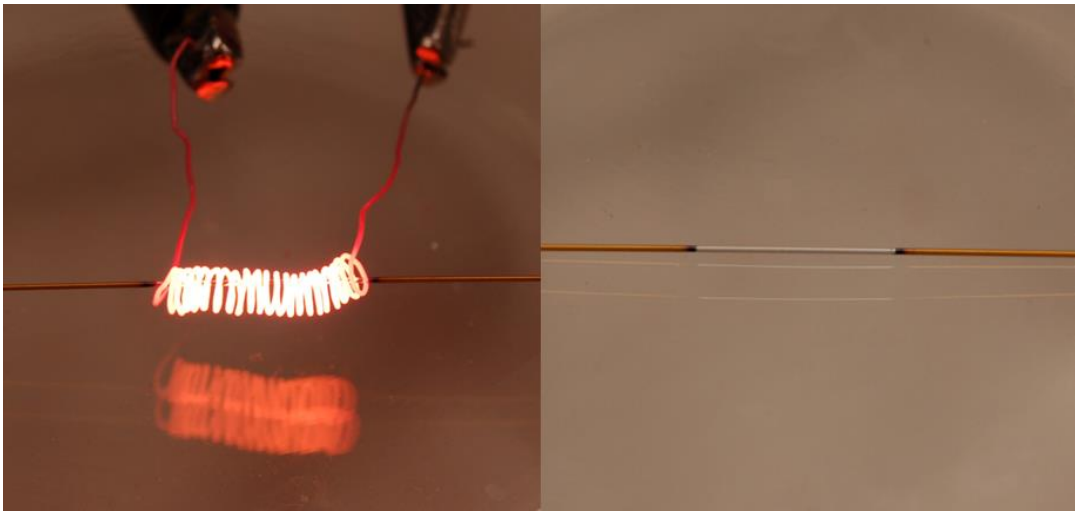

Figure 2-8 – (Left) - Removal of polyimide protective coating from capillary by heating. (Right) – Finished product.

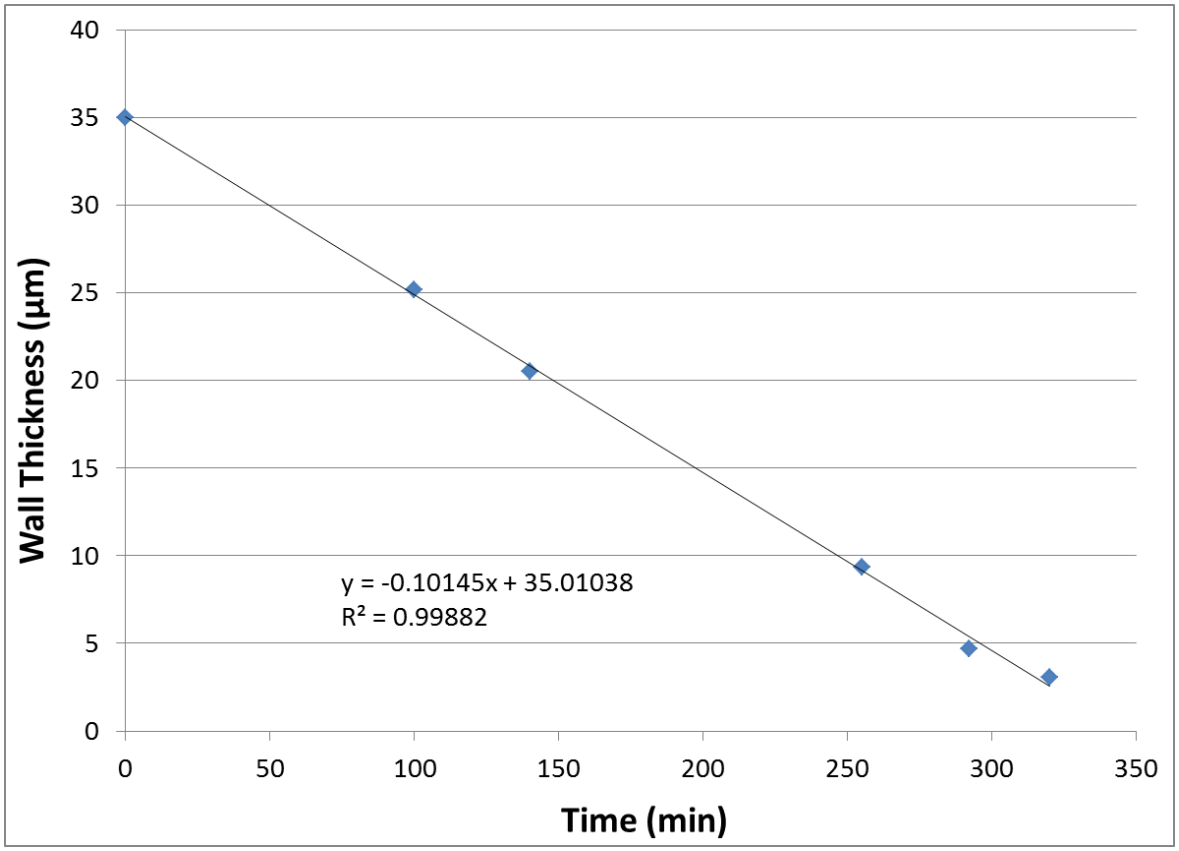

Figure 2-9 – Wall thickness of capillary as a function of etch time using Buffer-HF.

Tapering of Fibers

Tapering of input and output fibers was accomplished with a simple heating and pulling method. A 0.5 m section of 300 μm core/330 μm clad/ 370 μm coating, multi-mode fused silica fiber (Polymicro) was secured in a fiber chuck and suspended from a ring stand. A small weight was fastened to the bottom end of the fiber to provide a pulling force. Then, a small butane torch was used to gently heat a section of fiber until the bottom piece dropped away, leaving the suspended piece with a fully tapered end. A schematic of this operation is shown in Figure 2-10. For the absorption work in this chapter, the taper widths in the region of coupling with the capillary were 11 μm and 28 μm for the input and output fibers, respectively.

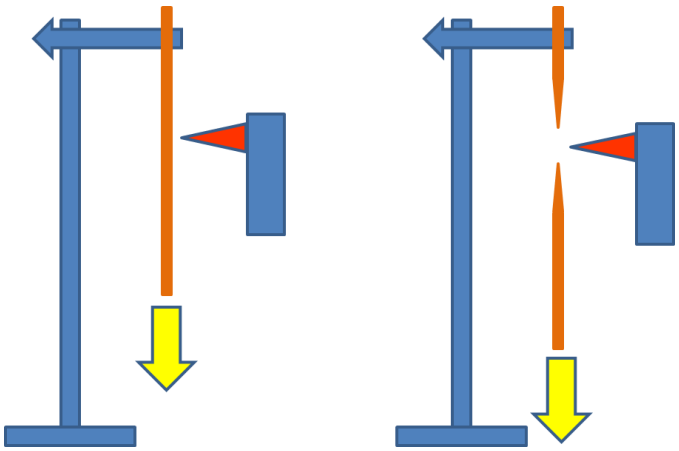

Figure 2-10 – Forming of tapered optical fibers by heating with butane torch and pulling.

Equipment

For the work in this chapter, a 700 mW white 'Rebel Star' LED was used as a light source (Luxeon Star LEDs). The "white" light in this particular model is produced from a blue LED with a yellow phosphor coating, resulting in the native output spectrum shown in Figure 2-11, containing a band around 450 nm and a wider band around 550 nm.

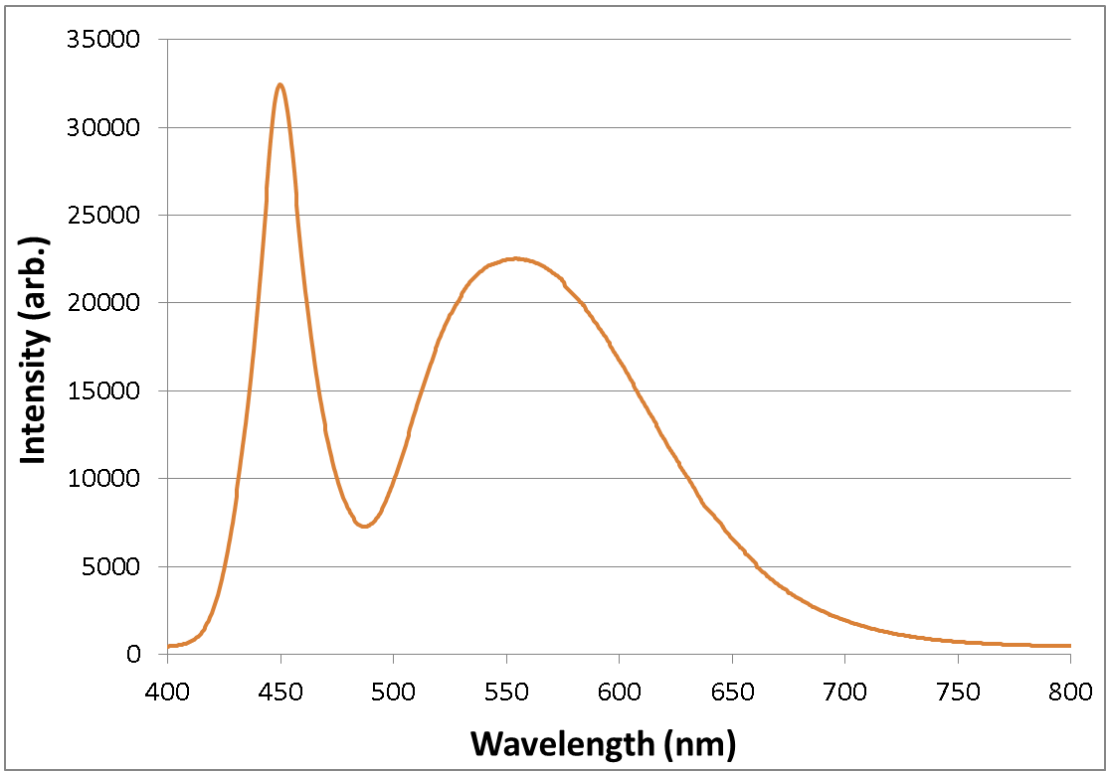

Figure 2-11 – Raw spectral output from "white" LED.

A 10X microscope objective was used to focus light from the LED onto the end face of the fiber leading to the input taper, shown in Figure 2-12. The output fiber was connected to a UV/Vis imaging spectrometer (Microspec 2300i, Acton Research Group) with a CCD camera (Pixis 100, Princeton Instruments). The gratings installed varied widely in resolution, from 150 to 2400 grooves/mm (g/mm). For the absorption work in this chapter, the 150 g/mm grating was used. Detector integration times ranged from milliseconds for cuvette readings up to seconds with the ring resonator, based on the amount of light being detected. Multiple spectral accumulations were taken where improved data quality was desired.

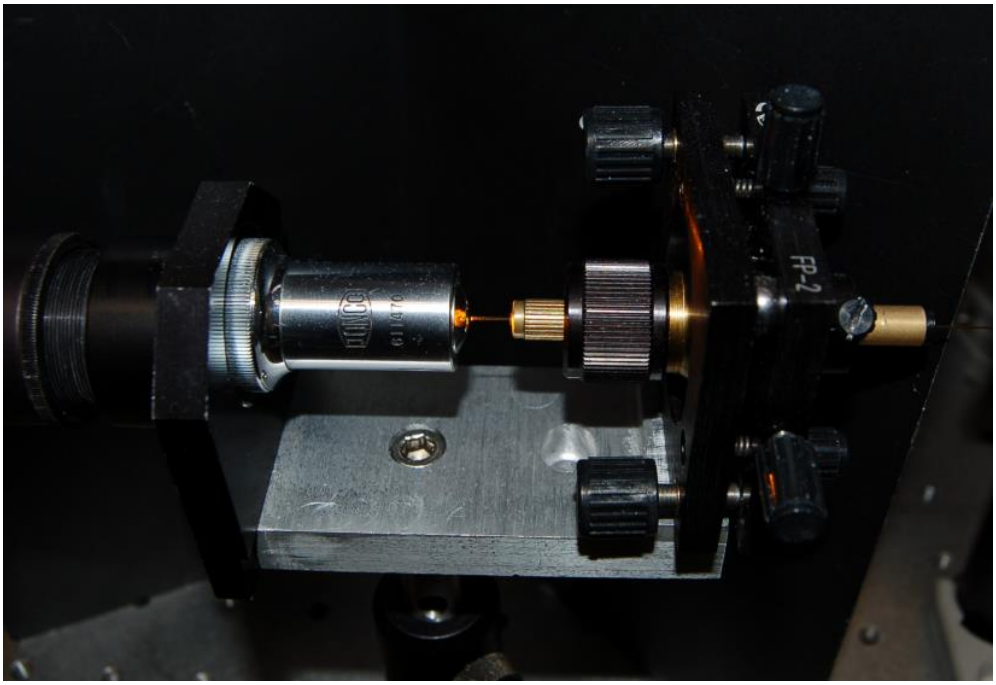

Figure 2-12 – Coupling light from LED to optical fiber using a microscope objective.

Cuvette

For comparison with conventional cuvette-based measurements, an apparatus was constructed that would use the same light source and spectrometer, but instead pass collimated light through a cuvette cell, as shown in Figures 2-13 and 2-14. In the photo, the two metal cylinders are collimating lenses and the cuvette is shown between them. This cuvette has a path length of 4 mm and holds a sample volume of 3 mL. The direction of the light path in the photo is left to right, towards the detector.

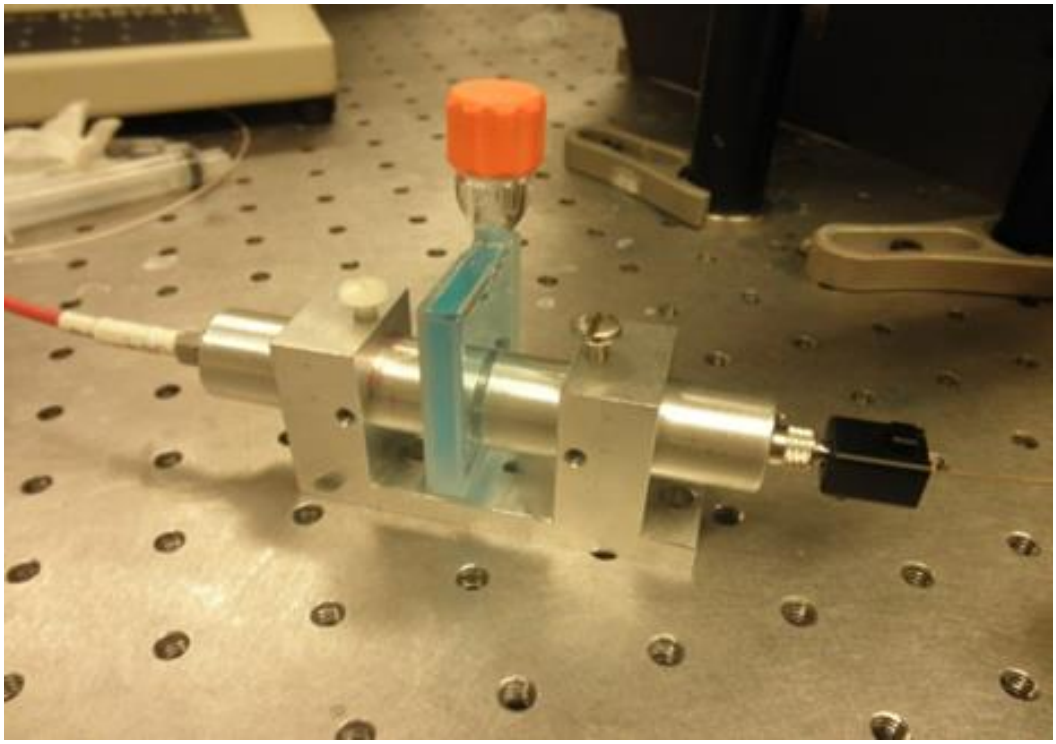

Figure 2-13 – Photo of cuvette cell used for comparisons.

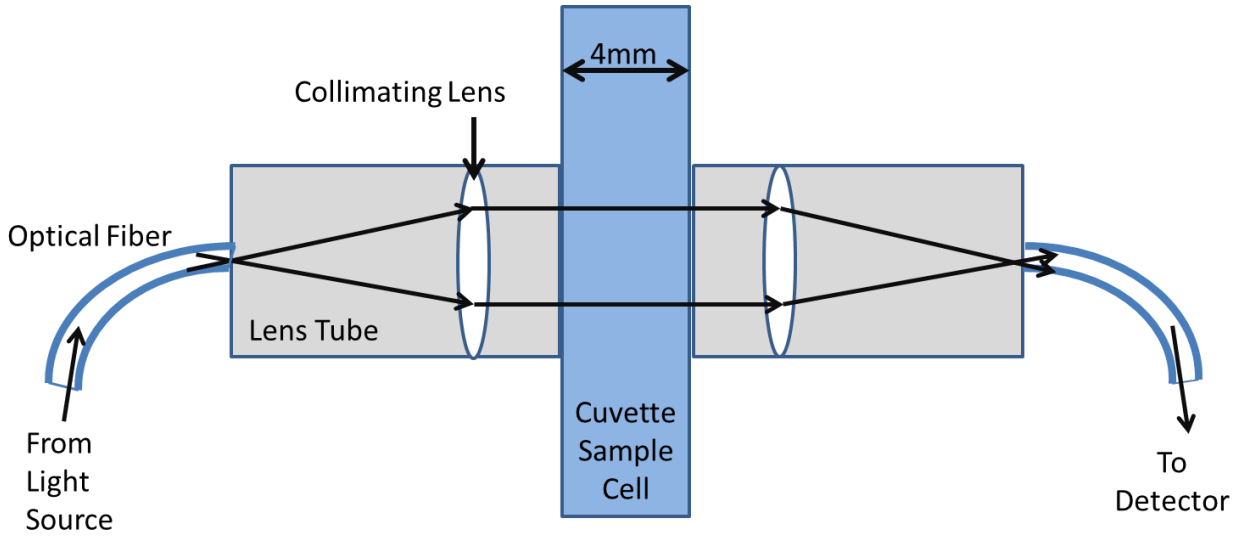

Figure 2-14 – Schematic of cuvette cell used for comparisons.

Chemicals

An initial stock solution of methylene blue was prepared to 10^{-3} M from powdered form (Sigma-Aldrich) in deionized water. All subsequent concentrations were prepared from serial dilutions of this stock. The Bromothymol blue stock solution of 10^{-2} M was also prepared from powdered form (Sigma Aldrich). However, due to the halochromic nature of BTB, the primary absorption band location is a function of solution pH. (Puschett, Rao, Karandikar, & Matyjaszewski, 1991) Therefore, all BTB solutions were prepared from 0.05 M dibasic sodium phosphate (JT Baker) to buffer the solutions at pH 8, where BTB solutions exhibit a blue appearance with a λ_{max} of 610 nm. (Tsunoda, Itabashi, & Akaiwa, 1992)

Reference blanks of deionized water or 0.05 M DSP, for MB or BTB solutions respectively, immediately preceded each set of experiments. Dilutions series were analyzed from lowest to highest concentration.

Results and Discussion

The spectral output from the ring resonator's drop port appeared to be considerably distorted from the original white LED output spectrum. In Figure 2-15, the original and ring resonator output spectra are pictures. By taking the ratio of intensity of the two spectra, Figure 2-16 is produced. This demonstrates a highly linear relationship between intensity and wavelength for the ring resonator output. Looking back at Equation 1-5, the evanescent penetration depth is a linear function of wavelength. In other words, longer wavelength light should be more readily coupled evanescently. As the coupling by the fiber tapers, into and out of the ring resonator, is

expected to be primarily done by the overlapping of evanescent fields, the linear distortion is therefore logical and expected.

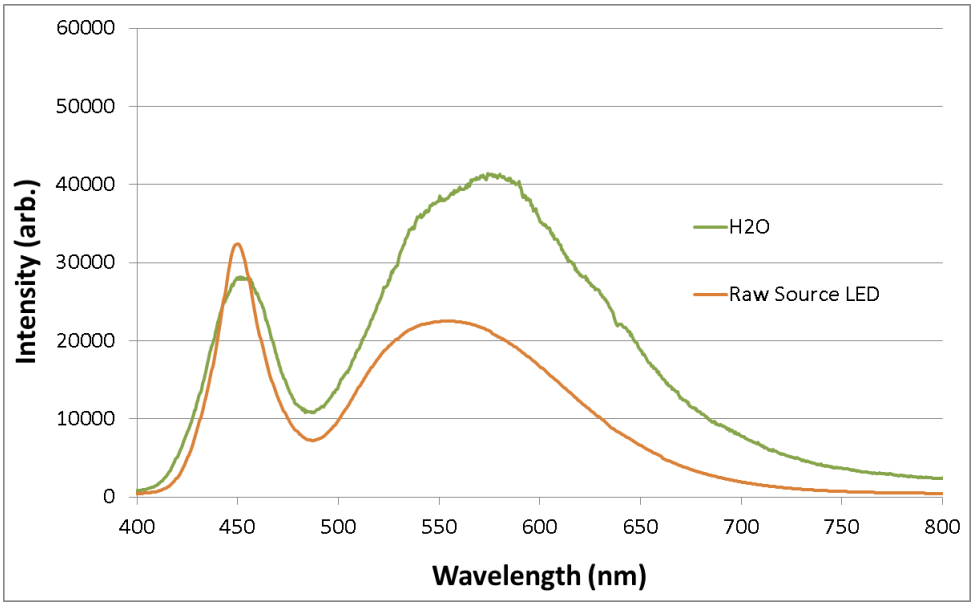

Figure 2-15 – Spectral shape of raw source LED and LCORR output with DI water in core. Overall intensity is adjusted for comparison

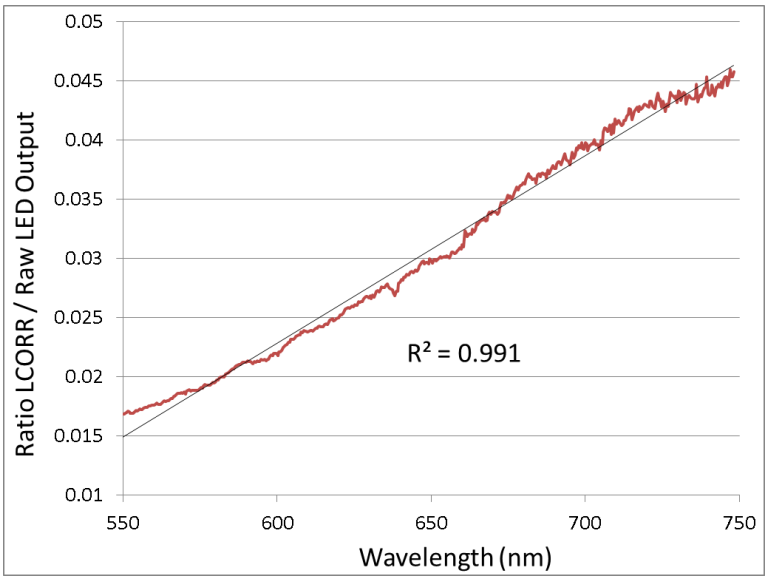

Figure 2-16 – Ratio of LCORR output to raw LED output produces a linear relationship with wavelength. Note that the scale only includes wavelengths above 550nm due to the complex spectral features below this point (i.e. peaks, valleys).

If broadband ring resonator coupling and operation were successful in the LCORR, an enhancement would be observed for a dye that has attraction to the surface and undergoes preconcentration. In aqueous solutions, methylene blue will dimerize with increasing concentration, and likewise at surfaces where preconcentration occurs. (Bergmann & O'Konski, 1963) (Heger, Jirkovsky, & Klan, 2005) The structure of methylene blue is shown in Figure 2-17. As a result of exciton splitting, the absorption band of the MB dimer is blue-shifted from the monomer band. Exciton splitting refers to the splitting of possible excited-state energy levels when a molecular aggregate, such as a dimer, forms. (Kemnitz, Tamai, Yamazaki, Nakashima, & Yoshihara, 1986) For a simple molecule that forms a 'side-by-side' dimer, lengthwise, a diagram of these energy levels is illustrated in Figure 2-18. In the figure, the 'head to head' dimer has a higher energy excited state than the 'head to tail' dimer, however only the 'head to head' form is allowed, as it is the only of the two that preserves the transition state dipole. This results in a 'blue shift', or shortening of the absorption band wavelength. Exciton splitting theory is presented in much more detail by others, such as Kasha, et al. (Kasha, Rawls, & Ashraf, 1965) This blue-shift, from approximately 660 nm to 610 nm, allows for identification and quantification of the two species.

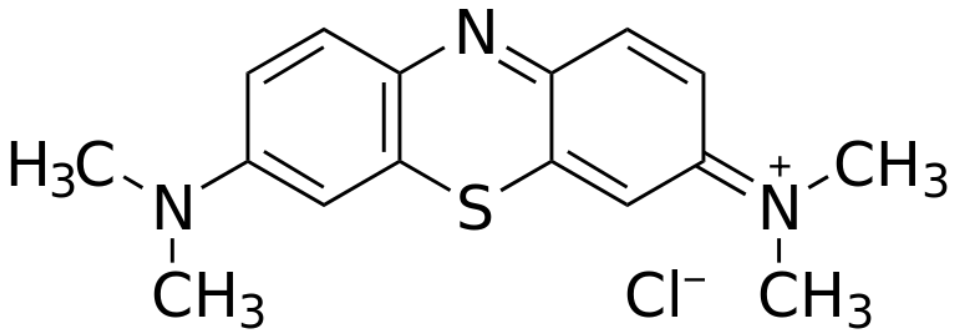

Figure 2-17 – Methylene blue molecule.

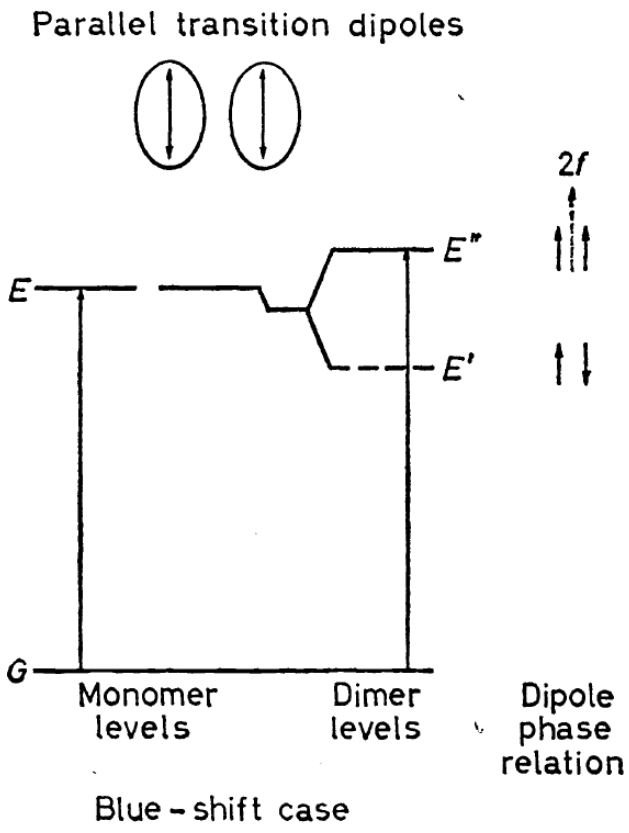

Figure 2-18 – Exciton splitting theory shows a shift in electronic energy levels as a result of dimerization. © IUPAC, 1965

In an aqueous solution, above pH 2, silanol groups on a bare silica surface will be primarily negatively charged. (Hubbard, 2001) (Papirer, 2000) This is illustrated in Figure 2-3. As a result, the positively charged MB is attracted to the bare silica surface. With increased concentration near the surface, the dimerization and band shift of MB occurs more readily at the surface than in the bulk solution. Also a contributing factor to the surface dimerization is the minimized repulsion between the positive charges on MB molecules. The increased presence of the dimer form of MB was observed by in surface detection applications, such as ATR spectroscopy (Tsunoda).

As described earlier, the mechanism for absorbance detection in a ring resonator is the attenuation of the evanescent field very near the surface. If the constructed broadband LCORR

device was truly functioning as a ring resonator, it would be expected that a solution of MB would exhibit absorption spectra dominated by the dimer absorption band around 610 nm. If this were not the case, other mechanisms for absorption detection might be based on scattered and/or stray light, such as a direct radial transmission through the capillary from the light scattered out of the fiber taper.

Shown in Figure 2-19 are the absorption spectra of MB solutions from 10^{-7} M to 10^{-5} M. This plot also includes the absorption spectra for the same solutions when analyzed in a 4 mm standard cuvette cell. From this plot, two important features appear to confirm the success of the broadband LCORR. First, the absorbance measured at the lower concentrations, 10^{-6} M and 10^{-7} M, is greater in the 250 μm diameter LCORR than in the 4mm cuvette. As the diameter, or theoretical straight-through transmission path, of the LCORR is approximately $1/16^{th}$ that of the cuvette cell, this implies an enhancement achieved by recirculating, resonating light. The non-linearity of concentration to absorbance in the LCORR is also shown in Figure 2-20, which also includes an order of magnitude higher concentration, to 10^{-4} M. Secondly, the increased dominance of the dimer peak at approximately 610 nm further confirms the mechanism as surface sensing. In bulk solution, as detected with a standard cuvette, the monomer and dimer absorbance peaks are of equal intensity around 10^{-4} M. In Figure 2-19, the LCORR spectra show the dimer peak reaching the intensity of the monomer around a bulk sample concentration of 10^{-6} M, two orders of magnitude lower. This further confirms surface-based detection from on the surface attenuation chemistry described above.

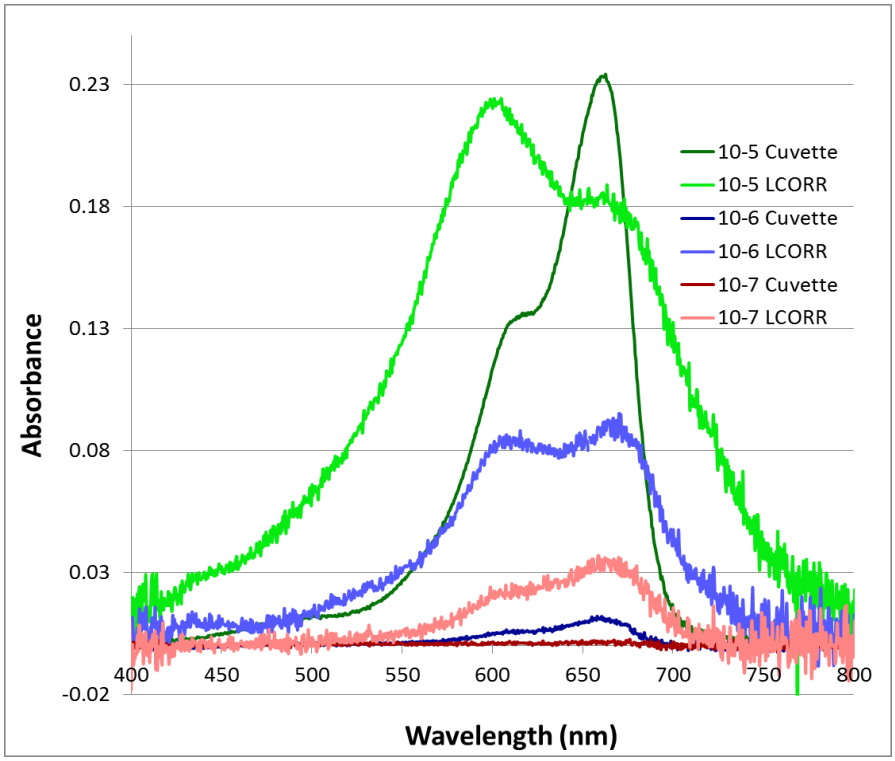

Figure 2-19 – Absorption spectra of methylene blue in both the LCORR and the 4mm cuvette cell.

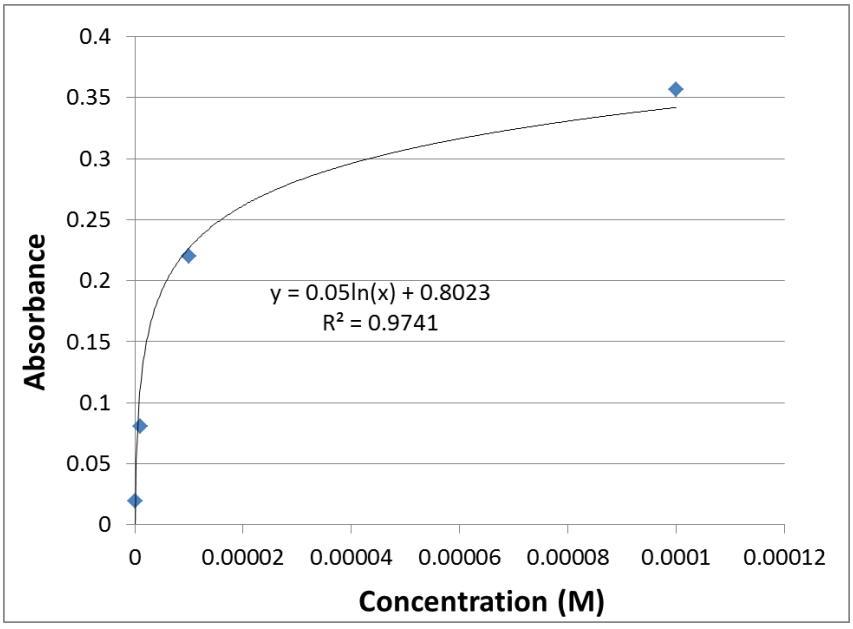

Figure 2-20 – Absorbance as a function of methylene blue sample concentration. Note the non-linear shape of this plot, as a linear relationship would be predicted for a standard transmission measurement according to Beer's law.

For a comparison to methylene blue, bromothymol blue (BTB) was chosen for its similar λ_{max} (in basic solution) and dissimilar surface activity. BTB is a halochromic pH indicator dye, appearing yellow in acidic solutions and blue in basic solutions. (Puschett, Rao, Karandikar, & Matyjaszewski, 1991) Shown in Figure 2-21 the blue form contains deprotonated oxygen atoms and a slight negative charge, thus it actually can exhibit a slight amount of repulsion to the bare silica surface.

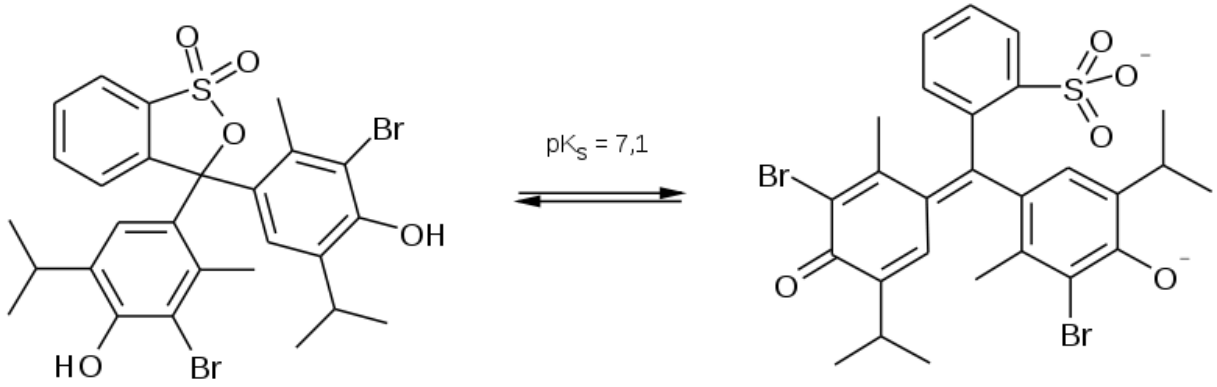

Figure 2-21 – Bromothymol blue molecule in acidic solution (Left), and basic solution (Right).

Shown in Figure 2-22 is a dilution series of BTB in both the LCORR and cuvette cell. Note that the concentrations being analyzed are an order of magnitude higher than those shown previously for MB. This is due to the reduced detectability of a non-surface active analyte in the LCORR. As expected, the LCORR does not outperform the cuvette cell for BTB absorbance, in contrast to MB.

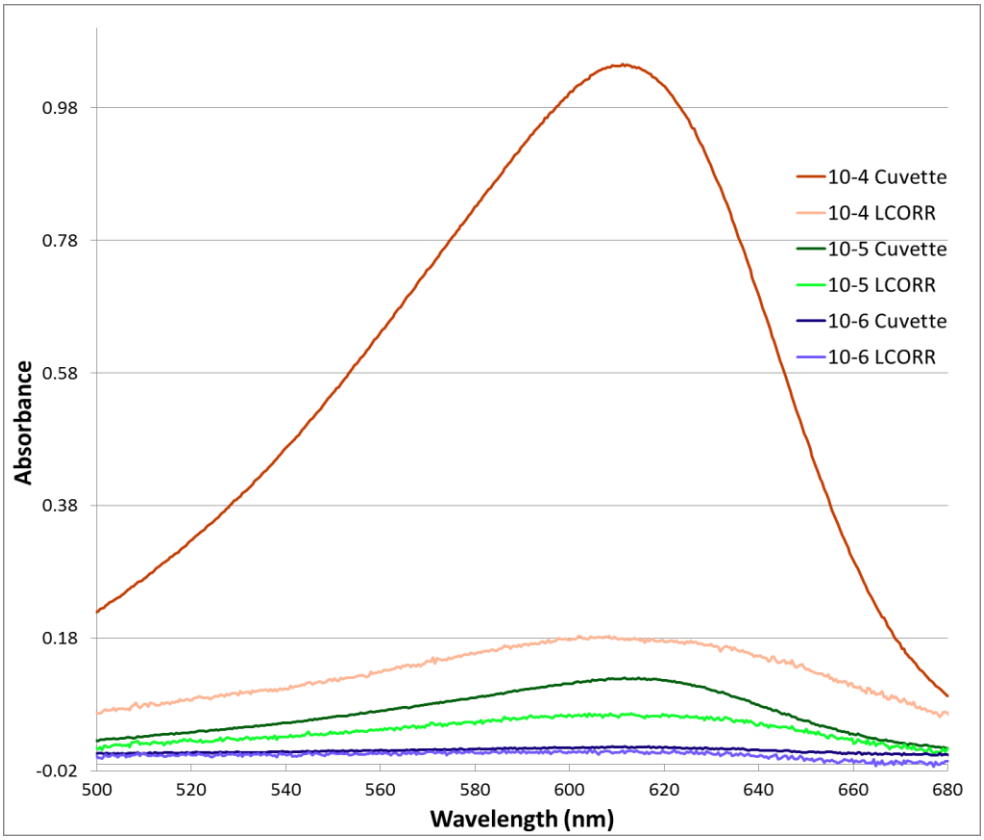

Figure 2-22 – Absorption spectra of Bromothymol blue in both the LCORR and the 4mm cuvette cell.

Tsunoda, et al. used the term "apparent path length", L_{app}, to quantify the enhancement factor in the absorbance of a surface attracted chromophores in an ATR cell. (Tsunoda, Itabashi, & Akaiwa, 1992) If absorbance measurements were taken both in a surface sensing device, as well as in a cuvette cell of known path length, then the L_{app} can be simply estimated from Equations 2-3 and 2-4. What this represents is the size, or path length, of a cuvette cell that would produce an equal absorbance response.

Equation 2-3

$$\frac{A_{\mathrm{LCORR}}}{A_{\mathrm{Cuvette}}} = \frac{\varepsilon c L_{\mathrm{app(LCORR)}}}{\varepsilon c L_{\mathrm{Cuvette}}}$$

Equation 2-4

$$L_{\mathrm{app(LCORR)}} = \frac{A_{\mathrm{LCORR}}}{A_{\mathrm{Cuvette}}}(L_{\mathrm{Cuvette}})$$

Another term often used in the context of ring resonators and other surface sensors is "effective path length". (Fan X. , White, Zhu, Suter, & Sun, 2008) The effective path length represents the equivalent amount of a cuvette-style transmission path length that would equal the light penetration in a surface sensor when all evanescent interaction is summed in total. (Tsunoda, Itabashi, & Akaiwa, 1992) As discussed earlier, the mechanism for absorption in a surface sensor, such as a ring resonator, is the attenuation of the evanescent field at the reflecting surface. Looking back at Equation 1-6, the electric field strength exponentially drops to 36.8% of original at a distance d_p away from the reflecting surface. (Harrick, 1979) Plugging in a wavelength of 600 nm, with n_1 and n_2 of fused silica and water, into Equation 1-5 produces d_p on the order of 200-900 nm, depending on incident angle. Although this appears to be a very short penetration into the sample, depending on the design of the sensor, many reflection points can be utilized to sum together towards a much greater L_{eff}. This in itself would still present a fairly short effective path length. Applications involving ATR probes actually embrace this limitation for analysis of highly concentrated and/or murky samples. (Blum & John, 2011) (Chai, Li, & Zhu, 2002) (Chai, Hou, & Verrill, 2005) (Howard, et al., 2009) (Billot, Couty, & Hosek, 2010) (Doyle & Tran, 1999) In a ring resonator, however, the light is circulating many times and building resonance, increasing effective path length dramatically. In the case where the analyte concentration is homogenous throughout the capillary, both axially and radially, the effective path length should be approximately equal to the apparent path length observed, calculated from Equations 2-5 and 2-6.

Equation 2-5

$$A_{\mathrm{LCORR}} = \varepsilon c l_{\mathrm{eff}}$$

Equation 2-6

$$l_{\mathrm{eff}} = \frac{A_{\mathrm{LCORR}}}{\varepsilon c}$$

Diminished resonator quality with high chromophore (sample) concentration can cause reduction in L_{eff} as analyte concentration is increased. (Westcott, et al., 2008) (Oates & Burgess, 2011) Therefore, L_{eff} is a dynamic variable. Additionally, any changes in real refractive index that alter the resonance conditions, described in more detail in Chapter 1, would also affect the evanescent penetration depth, in Equation 1-5, and modal propagation geometry, therefore altering L_{eff}.

Perhaps, a more intuitive approach to analyze the absorption enhancement in a ring resonator is to estimate an "effective concentration." As the L_{eff} in the sample core should be fairly consistent, at a low analyte concentration and stable RI, the greater L_{app} observed for surface-active analytes can be assumed to be a function of increased concentration at the reflecting surface (the capillary inner-wall, in this case). To estimate an effective surface concentration, C_{eff}, Beer's law, Equation 2-2, can be modified to Equation 2-7.

Equation 2-7

$$C_{\mathrm{eff}} = \frac{A}{\varepsilon L_{\mathrm{eff}}}$$

In this equation, the L_{eff} is estimated to be approximately equal to L_{app} for the case of a non-surface active dye. Tsunoda, et al. made the assumption that bromothymol blue (BTB) can be used in this situation. (Tsunoda, Itabashi, & Akaiwa, 1992) Using this assumption, L_{eff} for BTB, and therefore estimated L_{eff} for the LCORR, was found to 1.38mm. As BTB in a basic solution

should contain deprotonated oxygen, and thus it likely carries a slight repulsion to the bare silica surface, Sudan Black B (SB) was used for an additional verification of L_{eff}. Shown in Figure 2-23, SB has high solubility in hydrophobic, non-polar samples. (Bjerrum, Bhakdi, & Rieneck, 1980) Because of this, it is very insoluble in water, and therefore ethanol was used as a solvent. The L_{app} of SB, and therefore estimated L_{eff} of the LCORR, averaged to be 1.54 mm, comparable to the results for BTB. As the two values are similar, for C_{eff} estimation, a value equal to the average L_{eff} between BTB and SB, 1.46 mm, will be used.

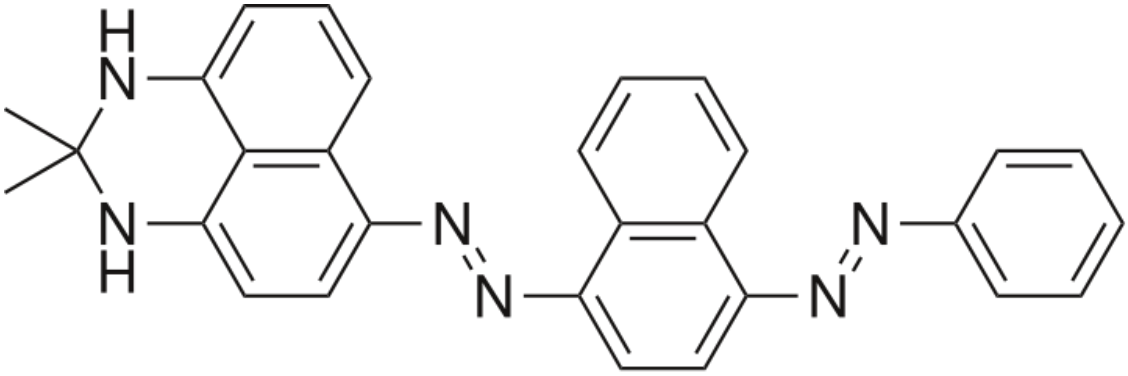

Figure 2-23 – Sudan black molecule.

With an estimated L_{eff} for the LCORR, the only other variable needed to estimate the effective surface concentration using Equation 2-7 is the molar absorptivity, ε. This value represents how absorbent the analyte is for a particular wavelength of light, independent of both the solution concentration and sample path length. Therefore, ε must be determined using a method where both the actual concentration and path length are known. The 4 mm cuvette cell, shown earlier in Figures 2-13 and 2-14, was used to analyze a dilution series of MB. Shown in Figure 2-24 are absorption spectra for MB concentrations from 10^{-4} M down to 10^{-7} M. Molar absorptivity, ε is solved for in Equation 2-8, producing a value with units $M^{-1}cm^{-1}$.

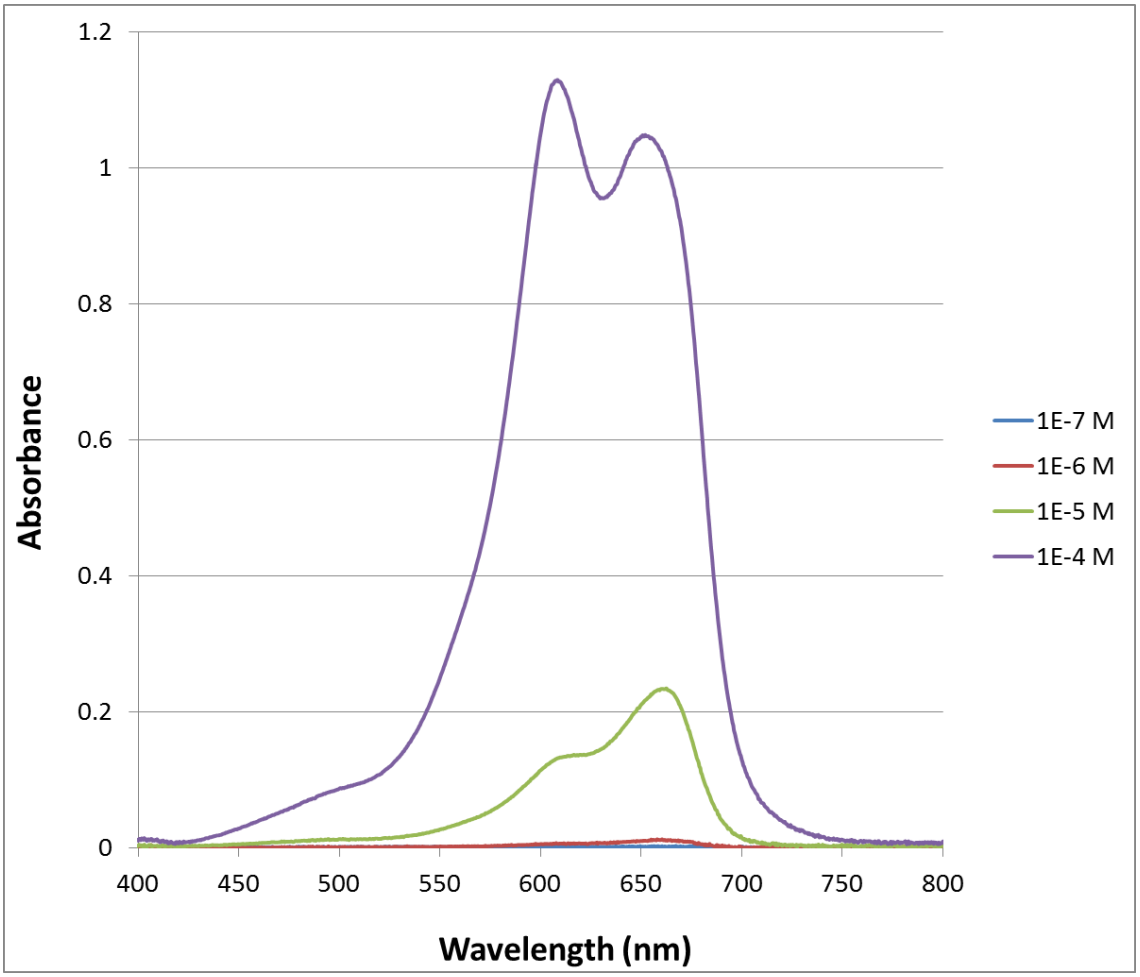

Figure 2-24 - Absorption spectra of methylene blue dilution series in 4mm cuvette, for molar absorptivity measurement.

Equation 2-8

$$\varepsilon = \frac{A_{\text{cuv}}}{cL_{\text{cuv}}}$$

The L_{cuv} is constant, 4 mm, and thus according to Beer's law, Equation 2-2, the plot of absorbance, A, vs. concentration, c, has the slope of ε. At sufficiently low concentrations, where the only mechanism for light attenuation can be assumed as absorption, the ε value should theoretically be constant, determined from the linear slope of an absorbance vs. concentration plot. As concentrations increase, both the detection limit of the spectrometer as well as the potential for

other attenuation mechanisms, such as scatter from incomplete dissolution for example, will affect the absorptivity. In the case of MB, or any other analyte that exhibits concentration-dependent oligomerization, the slope representing ε is only expected to be linear only at concentrations where the monomer is the only detectable species. While in a cuvette this might not be a serious issue, shown earlier in Figure 2-20, both the dimerization and surface preconcentration produce a non-linear relationship between absorbance and bulk concentration.

For calculations of L_{eff}, taking individual ε values per concentration is not a valid option to overcome the variability of ε with concentration. By the basis for determining C_{eff}, it is expected that the surface concentration of MB will not be equal to the bulk concentration- where ε values are derived from. Therefore, some error in C_{eff} can be expected and attributed to the variability of ε.

Shown in Figure 2-25, the effective surface concentration of MB in the capillary is plotted against the actual bulk sample concentration being introduced into the capillary. On observing the shape of this plot, the relationship between effective and bulk concentrations appears to be logarithmic. With surface attraction acting to preconcentrate the MB, this is the expected relationship. The availability of surface sites dictates the relative enhancement of surface concentration to bulk solution concentration. (Duff, Ross, & Vaughan, 1988) At lower solution concentrations, the relative surface preconcentration is more significant because of the greater availability of surface sites. With higher solution concentrations, the relative availability of surface sites is decreased until approximately 10^{-4} M, where the surface sites become saturated to the extent that no apparent difference between the surface and bulk solution absorbance is observed.

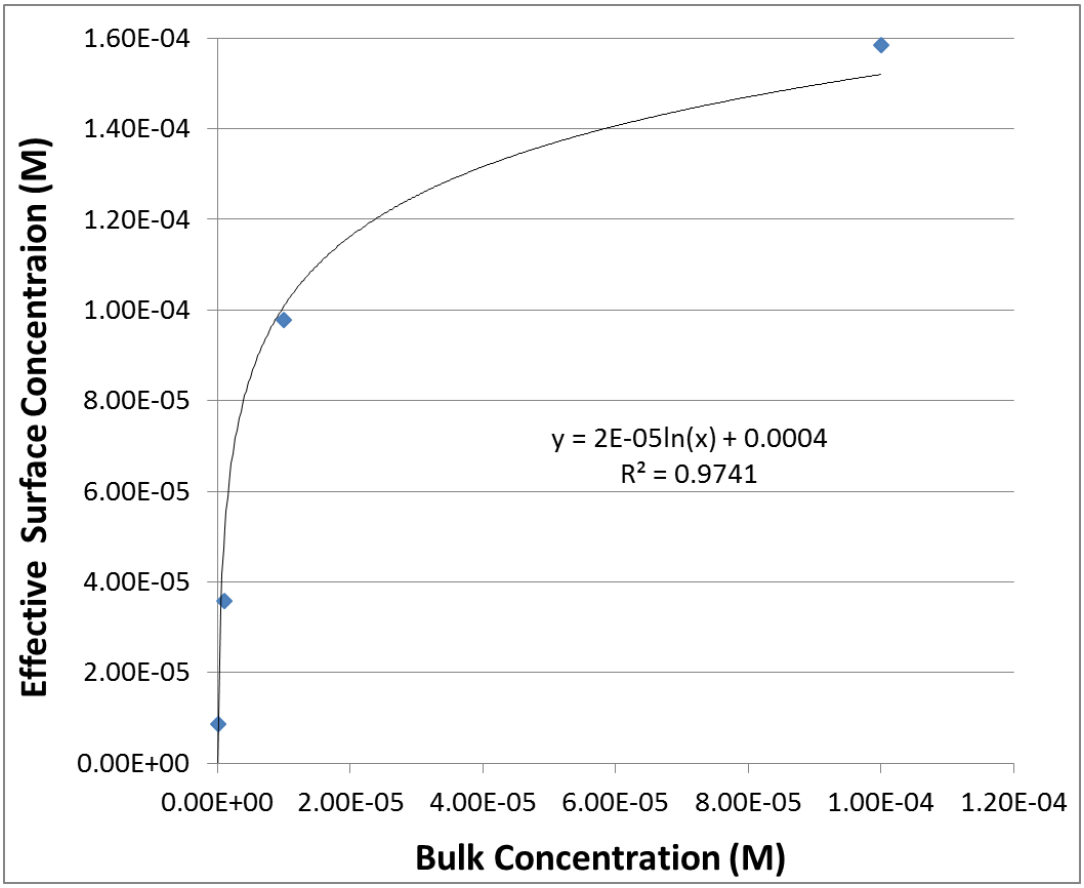

Figure 2-25 – Effective surface concentration, determined by Equation 2-7, vs. bulk sample concentration.

Surface adsorption kinetics have been studied and modeled extensively, in particular by the Langmuir and Freundlich models. (Sharma, 2012) Both models were attempted for this data, however the latter gave a slightly better fit. This is possibly due to the model accounting for surface heterogeneity, something very likely in a system that exhibits varying degrees of oligomerization. The Freundlich model takes the general form shown in Equation 2-9. Therefore a plot of $\log(C_{eff})$ vs. $\log(C_{bulk})$ should take a linear form with the slope of 1/n, which is a dimensionless heterogeneity factor, and an intercept of $\log(K_f)$, representing the Freundlich constant. (Sharma, 2012) (Proctor & Toro-Vazquez, 1996)

Equation 2-9

$$\log(C_{\text{surface}}) = \log(K_f) + \frac{1}{n}\log(C_{\text{bulk}})$$

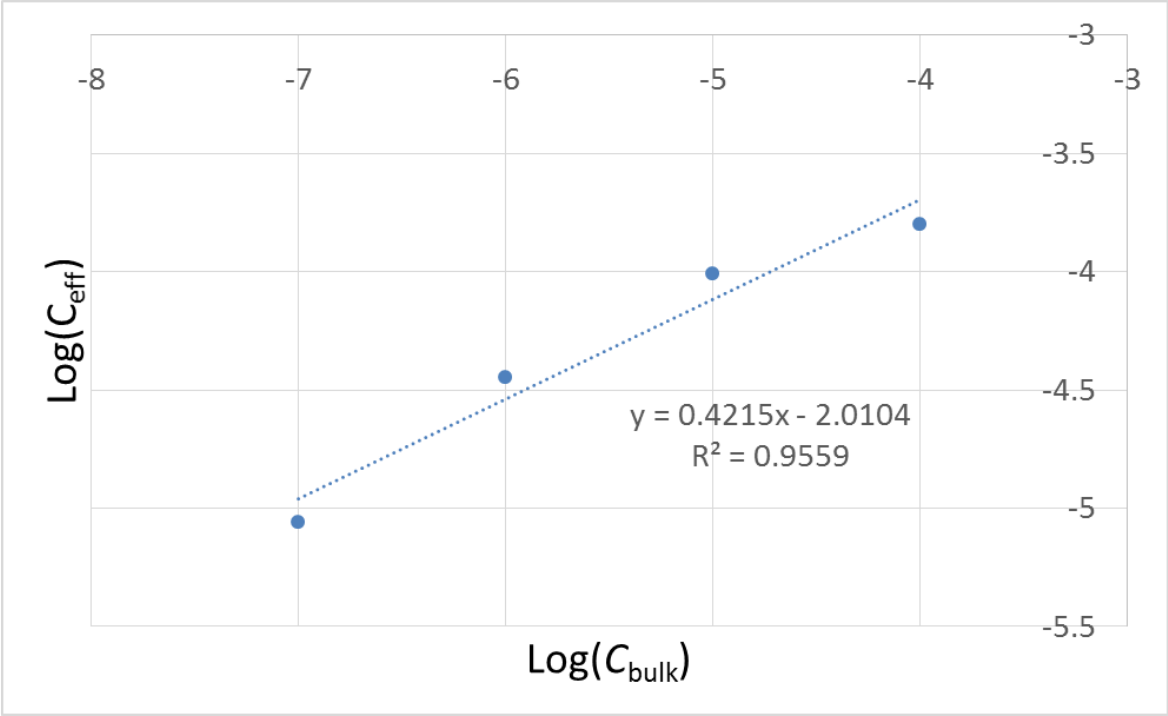

Figure 2-26 – Freundlich adsorption model for data presented in Figure 2-25.

Being able to observe and estimate the surface pre-concentration and C_{eff} through absorbance measurements further confirms the successful operation of a broadband LCORR, because as discussed earlier, the absorption being detected should theoretically be within the evanescent field very near the surface.

Conclusion

This chapter introduced broadband absorption sensing in a liquid core optical ring resonator. Circumferential light propagation and resonance in the device is confirmed though the distinct enhancement observed for surface-active dye. This enhancement is observed in comparison with both a non-surface active dye as well as when compared to cuvette-based results.

References

Arnold, S., Keng, D., Shopova, I., Holler, S., Zurawsky, W., & Vollmer, F. (2009). *Opt. Express, 17*, 6230-6238.

Bergmann, K., & O'Konski, C. (1963). *J. Phys. Chem., 67*, 2177.

Billot, P., Couty, M., & Hosek, P. (2010). *Org. Process Res. Dev., 14*, 511-523.

Bjerrum, O., Bhakdi, S., & Rieneck, K. (1980). *J. Biochem. Biophys. Methods, 3*, 355-366.

Blum, M., & John, H. (2011). *Drug Test. Anal., 4*, 298-302.

Boleininger, A., Lake, T., Hami, S., & Vallance, C. (2010). *Sensors, 10*, 1765-81.

Chai, X., Hou, Q., & Verrill, C. (2005). *J. Pulp Pap. Sci., 31*, 81-84.

Chai, X., Li, J., & Zhu, J. (2002). *J. Pulp Pap. Sci, 28*, 105-109.

Doyle, W., & Tran, L. (1999). *Spectroscopy, 14*, 46-54.

Duff, D., Ross, S., & Vaughan, D. (1988). *J. Chem. Educ., 65*, 815.

Fan, X. (2009). *Advanced Photonic Structure for Biological and Chemical Detection.* Dordrecht: Springer.

Fan, X., White, I. S., Zhu, H., Suter, J., & Sun, Y. (2008). *Anal. Chim. Acta., 620*, 8-26.

Fan, X., White, I., Zhu, H., Suter, J., & Oveys, H. (2007). *Proc. SPIE*, 6452-18.

Harrick, J. (1979). *Internal Reflection Spectroscopy.* Ossining: Harrick Scientific Corporation.

Heger, D., Jirkovsky, J., & Klan, P. (2005). *J. Phys. Chem. A, 109*, 6702.

Howard, K., Nagy, Z., Saha, B., Robertson, A., Steele, G., & Martin, D. (2009). *Cryst. Growth. Des., 9*, 3964-3975.

Hubbard, A. (2001). *Encyclopedia of Surface and Colloid Science.* Taylor & Francis.

Iqbal, M., Gleeson, M., Spaugh, B., Tybor, F., Gunn, W., Hochberg, M., et al. (2010). *IEEE J. Sel. Top. Quantum Electron., 16*, 654-661.

Kasha, M., Rawls, H., & Ashraf, M. (1965). *Pure Appl. Chem., 11*, 371-392.

Kemnitz, K., Tamai, N., Yamazaki, I., Nakashima, N., & Yoshihara, K. (1986). *J. Phys. Chem, 90*, 5094-5101.

Leidner, L., Zourob, M., & Lakhtakia, A. (2010). *Optical Guided-wave Chemical and Biosensors II.* Berlin: Springer-Verlag.

Newton, I. (1671). *Philos. Trans. R. Soc. London, 6*, 3075-3087.

Oates, T., & Burgess, L. (2011). *Appl. Spectrosc., 65*, 1187-1192.

Papirer, E. (2000). *Adsorption on Silica Surfaces.* New York: Marcel Dekker.

Puschett, J., Rao, B., Karandikar, B., & Matyjaszewski, K. (1991). *Talanta, 38*, 335-338.

Shopova, S., White, I., Sun, Y., Zhu, H., Fan, X., Frye-Mason, G., et al. (2008). *Anal. Chem.*, 2232-2238.

Simhi, R., Gotshal, Y., Bunimovich, D., Sela, B., & Katzir, A. (1996). *Appl. Opt., 35*, 3421-3425.

Skoog, D., Holler, F., & Nieman, T. (1998). *Principles of Instrumental Analysis.* United States: Thomson Learning.

Steiner, G., & Renschen, C. (1992). *Proc. SPIE, 1796*, 26-33.

Suter, J., & Fan, X. (2010). In A. Hawkins, & H. Schmidt, *Handbook of Optofluidics* (pp. 11(1-29)). Boca Raton: Taylor & Francis.

Suter, J., White, I., Zhu, H., & Fan, X. S. (2008). *Biosens. Bioelectron., 23*, 1003-1009.

Tarsa, P., Rabinowitz, P., & Lehmann, K. (2003). *Chem. Phys. Lett., 383*, 297-303.

Tsunoda, K., Itabashi, H., & Akaiwa, H. (1992). *Bull. Chem. Soc. Jpn., 65*, 1581.

Tsunoda, K., Umemura, T., Ueno, H., Okuno, E., & Akaiwa, H. (2003). *Appl. Spectrosc., 57*, 1273.

Umemura, T., Kasuya, Y., Odake, T., & Tsunoda, K. (2002). *Analyst, 127,* 149.

Westcott, S., Zhang, J., Shelton, R., Bruce, N., Gupta, S., Keen, S., et al. (2008). *Rev. Sci. Instrum., 79,* 033106.

Zhu, H., White, I., Suter, J., Dale, P., & Fan, X. (2007). *Opt. Express, 15,* 9139-9146.

Zourob, M., & Lakhtakia, A. (2010). *Optical Guided-wave Chemical and Biosensors I.* New York: Springer.

CHAPTER 3

Refractive Index Detection

Introduction

In Chapter 1, the conventional methods for refractive index detection in a resonant device were shown to be based on the tracking of a single resonance frequency or wavelength as the resonator conditions (e.g. mass, RI) changed. By introducing a broad spectrum of light into a ring resonator, a multiplicity of wavelengths and therefore propagating modes should be present. In this chapter, analytical approaches will be shown to demonstrate the extraction of useful information from the resulting complex spectra produced by the broadband ring resonator.

History and Background

In 984 A.D., Persian mathematician and physicist Ibn Sahl produced a manuscript "On Burning Mirrors and Lenses" (translated) that first described the laws of refraction. (Rashed, 1990) In Figure 3-1, translated to Figure 3-2, Sahl explains that if the ratio of the ray path lengths L_1/L_2 is kept equal to n_1/n_2, then the rays satisfy the Law of Sines, in Equation 3-1. (Skurnick & Javadi, 2006) This is fundamentally what is now known as Snell's Law, as modern credit was given to Dutch astronomer Willebrord Snellius, who studied and mathematically derived the same concepts over 600 years later.

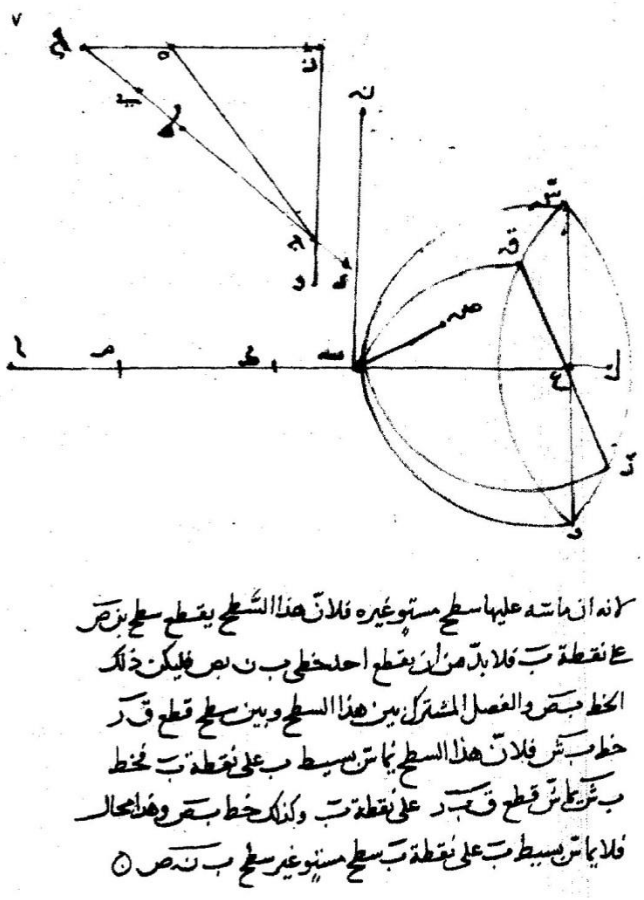

Figure 3-1 – Ibn Sahl's illustration of light refraction from "(On Burning Mirrors and Lenses)," 984 A.D.

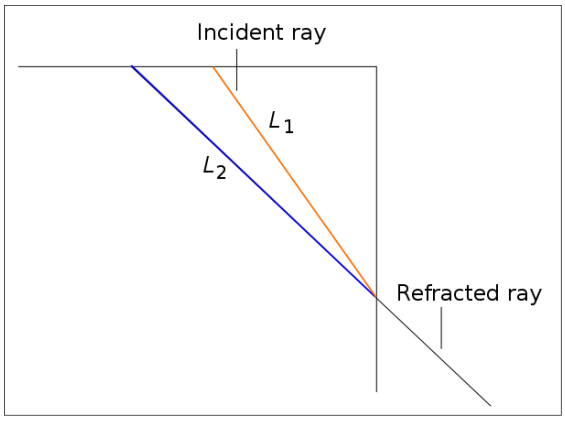

Figure 3-2 – Simplified and translated version of Figure 3-1.

Equation 3-1

$$\frac{\sin \theta_1}{\sin \theta_2} = \frac{v_1}{v_2} = \frac{n_2}{n_1}$$

The physical property dictating Snell's Law is the refractive index (RI). This is defined, in Equation 3-2, as the ratio of the speed of light, *c*, in a vacuum, over the speed of the light in the material, *v*. In a vacuum, light travels approximately 2.998 x 10^8 ms^{-1} with a refractive index, by definition, of 1.000. (NIST, n.d.) For electromagnetic radiation to be transmitted through matter the radiation must be absorbed and re-emitted in the path of transmission, and the electric and magnetic field oscillation of the radiation must be perpetuated by the matter. This process slows down the group velocity, or phase speed, of the radiation travelling through in the material, thus altering *n* in Equation 3-2. Depending on the degree of this deceleration, the refractive index can vary from approximately 1 for air to well over 1.5 for certain glasses and other visibly transparent materials.

Equation 3-2

$$n = \frac{c}{v}$$

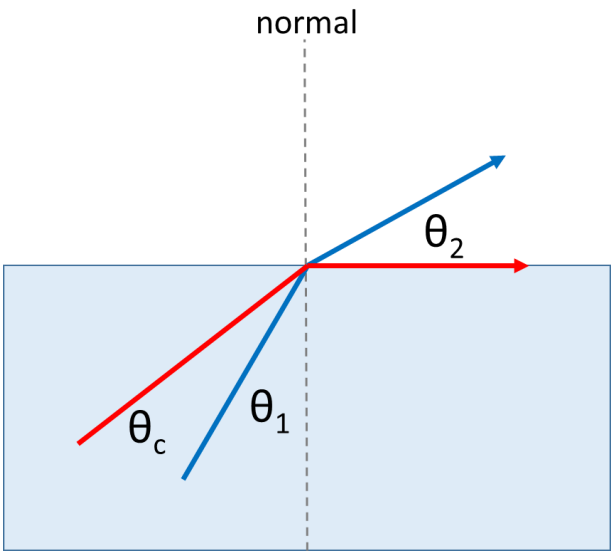

Figure 3-3 – Refraction through an interface is caused by a change in refractive index between the two materials.

Snell's Law predicts a minimum "critical" angle for total internal reflection, and thus waveguide or whispering gallery modes, to occur. (Dakin & Culshaw, 1988) (Daly, 1984) (Gibb, 1942) (Harrick, 1979) Shown in Figure 3-3 a light ray is approaching an interface with a lower RI material. In the lower RI material, the wavelength is increased, increasing phase speed, while the frequency remains the same. This results in the bending of the ray path from its original propagation angle. At a great enough angle perpendicular to the interface, the reflected angle reaches 90 degrees and does not transmit into the lower RI material. As the ray is totally reflected at the interface, this phenomenon is known as "total internal reflection". The reflected angle is determined by the Snell's law equation, Equation 3-1. To find the minimum critical angle where TIR occurs, θ_2 in Equation 3-1 is set to 90 degrees and therefore the equation can be rearranged to Equation 3-3. As RI varies with wavelength, and Snell's law predicts the allowed angles of reflection to be a function of RI, a multiplicity of propagating modes is expected for an incident ray of broadband (white) light.

Equation 3-3

$$\theta_{\text{crit}} = \arcsin\left(\frac{n_2}{n_1}\sin\theta_2\right) = \arcsin\frac{n_2}{n_1}$$

RI as detection method

As refractive index is a function of the electrons in the material, RI is considered to be a universal detection method. (Katz, 1998) Being a universal detection method also makes RI naturally nonselective. This can be overcome by employing a pre-separation and/or selective surface-binding chemistry. Additionally, in tightly controlled systems, where only a limited number of analytes are possible, a non-selective detector is perfectly acceptable. One example of this might be the production of fermented beverages, where RI is estimated to be only a function of sugar content, and other sources are assumed to be negligible. (Palmer, 2006)

Refractive index based detection has been used for decades in a wide variety of applications. (Fan X. , White, Zhu, Suter, & Sun, 2008) (Katz, 1998) (Scott, 1996) (Liang, Huang, Xu, Lee, & Yariv, 2005) Before optical ring resonators, RI detection was employed in SPR, Bragg Fibers, and in detectors for HPLC, to name a few. The distinction should be made that in a ring resonator the RI detection is at the surface, while this is not necessarily the case with all of the previous methods listed above. (Arnold, et al., 2009) (Boleininger, Lake, Hami, & Vallance, 2010) (Fan, Advanced Photonic Structure for Biological and Chemical Detection, 2009) (Fan X. , White, Zhu, Suter, & Sun, 2008) (Fan X. , White, Zhu, Suter, & Oveys, 2007) (Iqbal, et al., 2010) (Gibb, 1942) (Shopova, et al., 2008) (Suter & Fan, Handbook of Optofluidics, 2010) (Suter J. , White, Zhu, & Fan, 2008) (Vollmer & Arnold, 2008) (Zhu, White, Suter, Zourob, & Fan, 2007) (Zhu, White, Suter, Dale, & Fan, 2007) (Leidner, Zourob, & Lakhtakia, 2010) In applications utilizing

RI, much of the attractiveness comes from the ability to non-destructively detect analytes without the need for chromophores or fluorophores.

Theoretically, as a broad spectrum of light is introduced into a ring resonator, an interference pattern should be formed as a result of the constructive and destructive wavelengths. (Oates & Burgess, 2012) If the output from this ring resonator is taken from a drop port, the spectral output should be analogous to an interferogram. Therefore, rather than taking a single resonance wavelength, as in conventional ring resonator methods, a more appropriate means of data analysis is to measure the spacing between constructive resonance peaks, or fringes. By taking the derivative of Equation 1-3 to determine the theoretical wavelength spacing between integral numbers, $d\lambda/dm$, the result is an expression that would vary with wavelength. Instead, if spectra are viewed in the frequency domain, constructive frequencies in wavenumber are given in Equations 3-4 and 3-5. Taking the derivative of this equation to find wavenumber spacing per integral number, $d\tilde{\nu}/dm$, produces an expression in Equation 3-5 that is dependent only on the resonator's dimensions and RI. As a result, all collected spectra in this chapter will be displayed in terms of wavenumber rather than wavelength.

Equation 3-4

$$\tilde{\nu} = \frac{10^7 m}{2\pi r L_{\text{opt}} n_{\text{eff}}}$$

Equation 3-5

$$\frac{d\tilde{\nu}}{dm} = \frac{10^7}{2\pi r L_{\text{opt}} n_{\text{eff}}}$$

Fourier transform analysis is a widely used mathematical technique employed in several analytical chemistry technologies. (Skoog, Holler, & Nieman, 1998) Mathematically, an algorithm is used to extract periodic frequency components from a time-domain spectrum.

(Brigham, 1974) A simplified example is shown in Figures 3-4, 3-5, and 3-6. In one of its most well-known applications, Fourier Transform Infrared (FT-IR) spectroscopy, the spectrometer is essentially an interferometer, as shown in Figure 3-7. In this device, one channel is used as a stationary reference and the other employs an adjustable mirror to vary the path length. This process creates a complex output of interference spectra as a function of mirror position. In turn, the frequency of light can be extracted from the interference spectra, and therefore also the absorption as a result of intensity loss. In the current work, as the spectral output is already given in terms of frequency, the periodic 'frequency' component being extracted is the fringe spacing $d\tilde{\nu}/dm$ that is a result of the interfering wavelengths of light circulating the resonator.

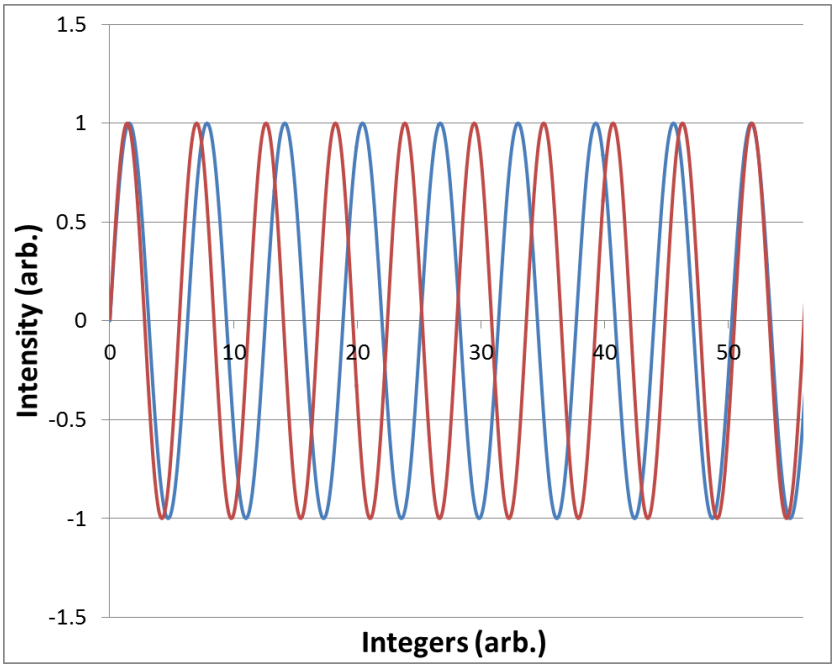

Figure 3-4 – Arbitrary sine waves with varying wavelengths. Note that the waves are nearly in-phase at the beginning and nearly out of phase in the center of the plot.

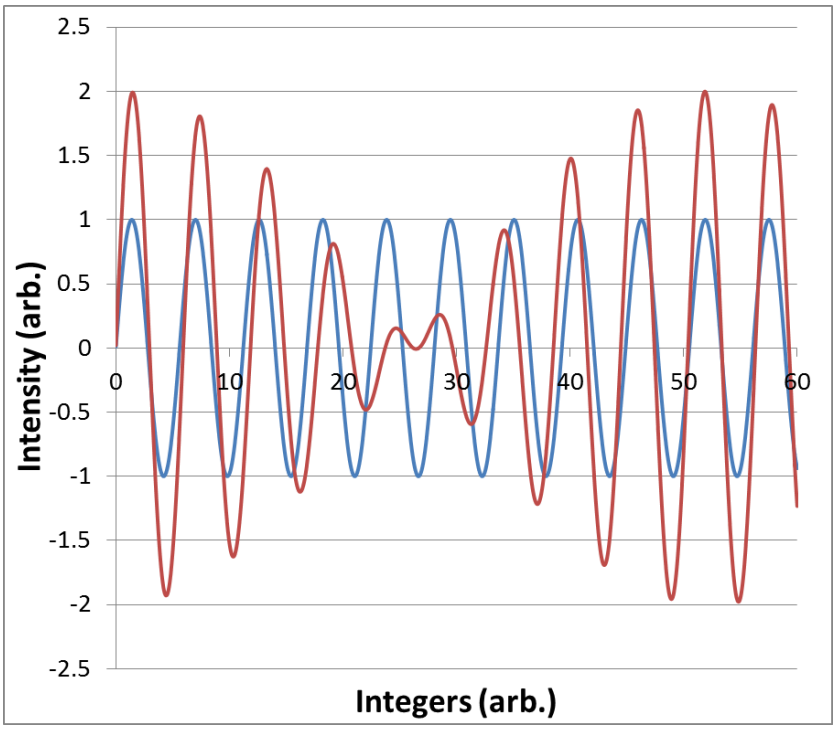

Figure 3-5 – From Figure 3-4, one plot (in blue) is kept the same and a second plot (red) is the sum of the two original waves.

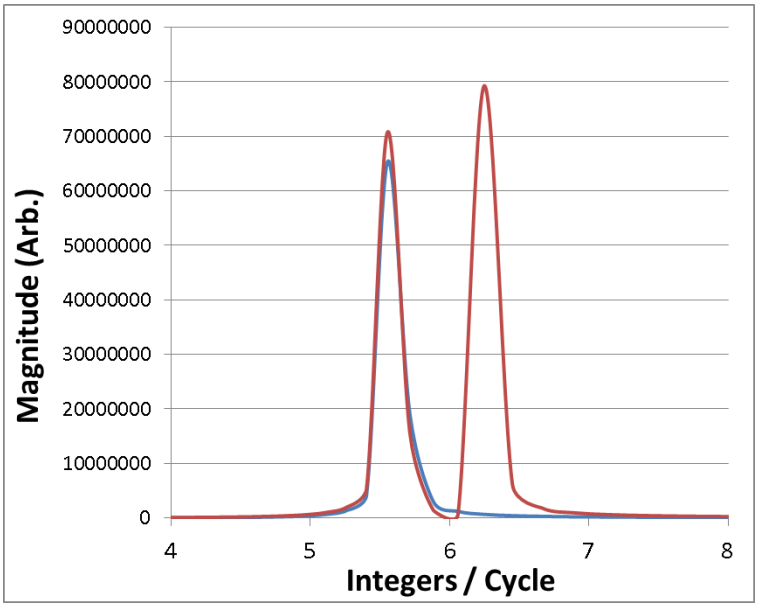

Figure 3-6 – Fourier transform of the plots in Figure 3-5.

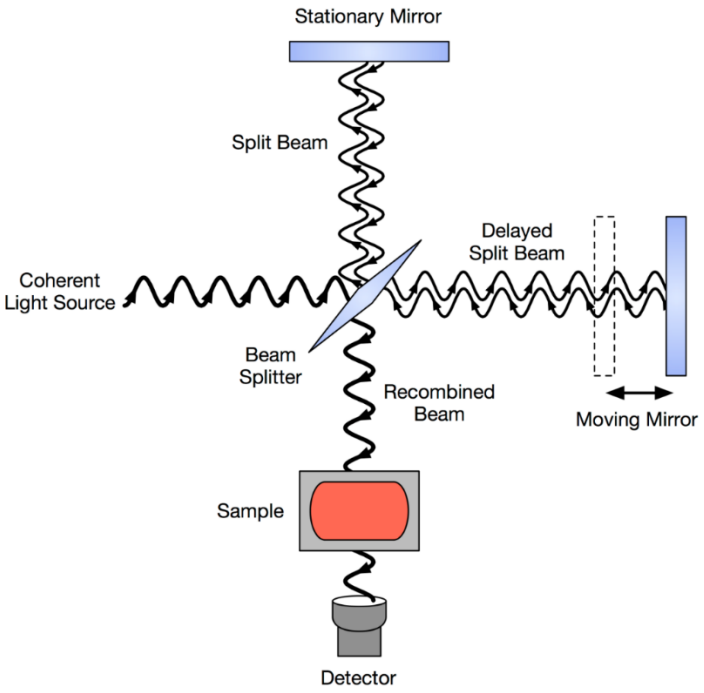

Figure 3-7 – Schematic of Fourier transform infrared spectrometer, based on Michelson interferometer.

While Equation 3-5 reduces the variables down to the resonator's dimensions and RI, it must be noted that any technique utilizing a spectral range to extract a frequency component will result in broadening as a result of material dispersion by the resonator. Material dispersion is essentially the variability of refractive index with wavelength. (Daly, 1984) Shown in Figure 3-8 is the dispersion plot of fused silica. This plot is based on the dispersion equation, shown in Equation 3-6, experimentally determined by Malitson. (Malitson, 1965) In the range of 16667 cm^{-1} (~600 nm), the RI of fused silica varies approximately 1.3 x 10^{-6} RIU/cm^{-1}. Across a spectrum of 400 cm^{-1} (~15 nm), typical with a 2400 g/mm grating, this presents a range (broadening) of approximately +/- 3 x 10^{-4} RIU. If frequency spacing, $d\tilde{\nu}/dm$, are presented in terms of average peak positions, this broadening may be of negligible concern.

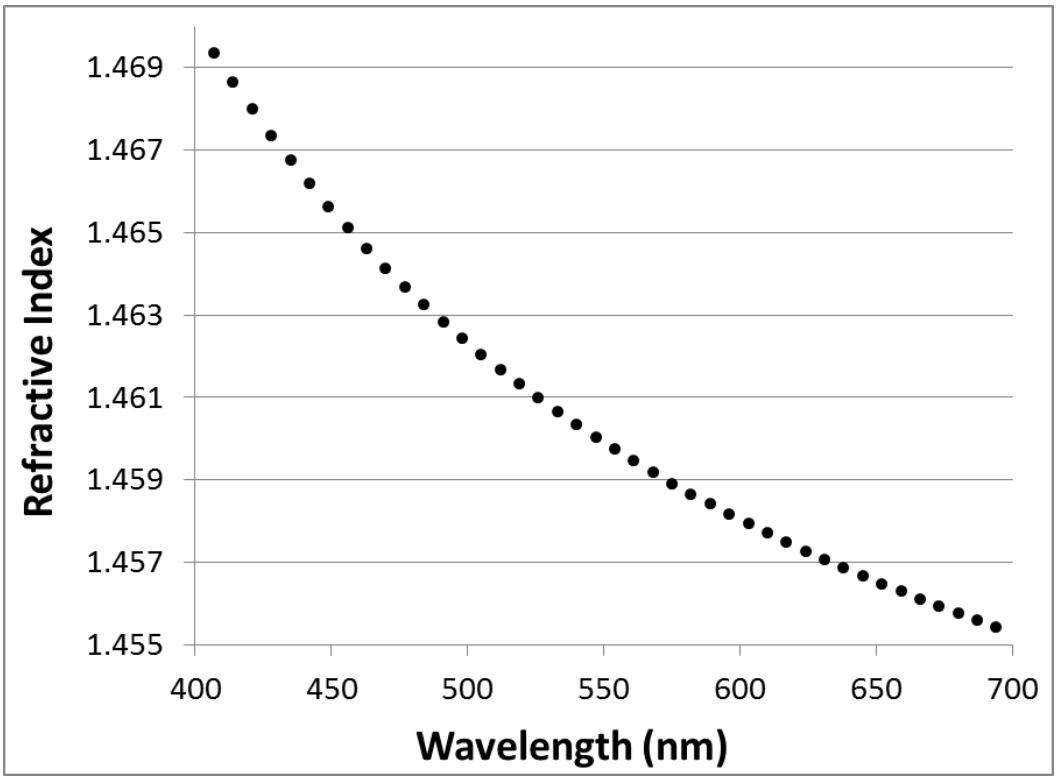

Figure 3-8 – Dispersion plot (RI vs. wavelength) of fused silica at 20c.

Equation 3-6

$$n^2 - 1 = \frac{0.6961663\lambda^2}{\lambda^2 - (0.0684043)^2} + \frac{0.4079426\lambda^2}{\lambda^2 - (.1162414)^2} + \frac{0.8974794\lambda^2}{\lambda^2 - (9.896161)^2}$$

With regard to sample sensitivity, as Snell's Law is dependent on RI, it is expected that the distribution of propagating modes will vary with a change in sample RI in the capillary core. With this shift in propagation angles comes a change in evanescent field penetration depth, per, Equations 1-5. Altering d_p will, in turn, change the relative field fractions in Equation 1-4. In a complex manner, the interdependent optical relationships present in a multimode resonator further enhance the RI sensitivity beyond the theoretical single-mode shift approximated in Equation 3-5.

Experimental

For initial experiments, a basic proof of concept device was constructed based on the liquid core optical ring resonator (LCORR) geometry. (Fan X. , White, Zhu, Suter, & Oveys, 2007) (Fan X. , White, Zhu, Suter, & Sun, 2008) (Suter J. , White, Zhu, & Fan, 2008) This device was also designed based on a coupling scheme shown in Figure 1-17 where two fibers with tapered ends are brought into contact with opposite sides of the capillary. In this manner, one fiber acts as an input and the other acts as an output, or "drop" port, as shown earlier in Figure 1-16. In the device, the capillary is epoxied to a squared U-shape block of PMMA. The block started out as a cube, and a wide channel was simply carved out of the center to give clearance to the input and output fibers. Shown in Figure 3-9 is an overhead photo of the device, next to a schematic illustration. In the photo, the capillary appears left to right, and the illuminated fiber, shown vertically, is the input fiber. This fiber is actually beneath the capillary, on the opposite side from the observer taking the photo. On top of the capillary is the output fiber, positioned at a slight angle primarily for ease of construction. Both the input and output fibers are epoxied to extensions rods that are secured in optical positioning mounts.

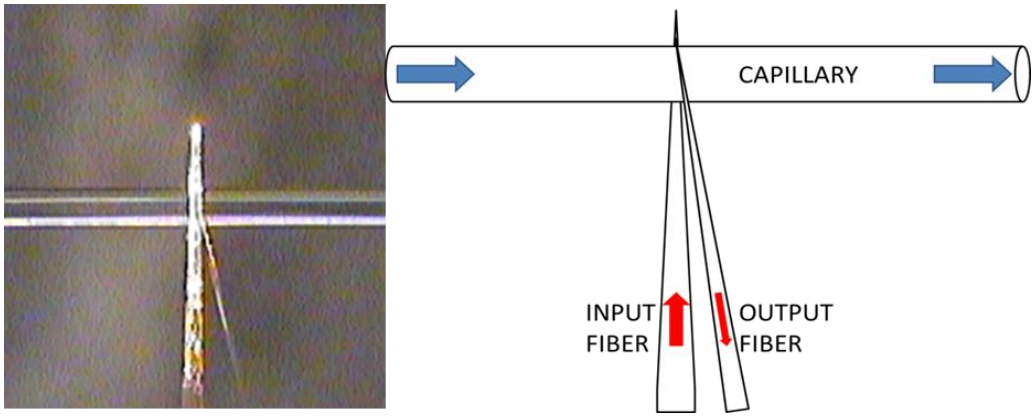

Figure 3-9 – Overhead photo (Left) and schematic (Right) of the LCORR used in this chapter. © 2012 American Chemical Society

Resonating light can be guided by whispering gallery modes or waveguide modes, as illustrated earlier in Figure 1-9. In the case of an LCORR, reflection off of the inner wall surface is necessary for evanescent penetration of the core, where the sample is located. Therefore, waveguide modes become crucial. Achieving a very thin capillary wall is necessary to promote these modes. Using smaller diameter, but relatively similar LCORRs, Fan and coworkers found that wall thicknesses of approximately 4 μm or less were necessary to gain sufficient interaction with the sample core. (Fan X. , White, Zhu, Suter, & Oveys, 2007) (Fan X. , White, Zhu, Suter, & Sun, 2008) Using methods to be fully explained later, in Chapter 4, RI sensitivity as a function of wall thickness confirmed an inverse relationship. In other words, thinner walls allowed for greater RI sensitivity.

Thinning of the capillary was accomplished by etching with dilute buffered hydrofluoric acid (Buffer-HF, Transene Company, Inc.). Due to the poisonous and corrosive nature of HF, even at lower concentrations, appropriate safety precautions were taken during use. Standard 250 μm ID/ 360 μm OD fused silica capillary (Polymicro Technologies, Inc.) was used. A protective polyimide coating, common on most fused silica capillaries and many fibers, was removed by heating with a coil of NiCr resistive wire, as shown earlier in Chapter 2, Figure 2-9. Etch times on the order of 6 hours were found to reduce the wall thickness down to 3-4 μm, from 35 μm initially. Thinning beyond this point resulted in walls that were considerably more fragile and difficult to handle in construction and experimentation. The capillary used for the experiments in this chapter was found to have a wall thickness of 4 μm using a standard imaging microscope (Zeiss).

Tapering of input and output fibers was accomplished simply by heating and pulling. A section of fused silica fiber, 300 μm core/330 μm clad/370 μm coating (Polymicro Technologies,

Inc.), was secured at one end in a fiber chuck. This was suspended from a ring stand, and a small weight was fastened to the hanging bottom end to provide a pulling force. Using a butane torch, one spot in the middle of the fiber was gently heated until the bottom piece dropped away, leaving the top piece with a tapered end. A schematic of this apparatus was shown earlier in Figure 2-10.

Both input and output fibers end in a very small point. The optimal locations for coupling into and out of the capillary were found to be slightly up from the end points, however. At the region of contact, the input and output fiber diameters were approximately 60 μm and 15 μm, respectively. This is larger than would be expected for a single mode/wavelength resonator. As this device utilizes multiple wavelengths and modes, it was found that the wider parts of the fiber tapers allowed more flexibility in finding optimal resonance positioning. Additionally, this allowed for greater quantities of light to couple in and out of the resonator for improved data quality and sample throughput.

The light source used in the high-resolution RI shifting experiments was primarily an amber, 591 nm, Rebel LED (Luxeon Star LEDs). A white LED, containing a 450 nm diode with yellow phosphor, was also used when a wider spectrum was desired. Additionally, where an even wider spectrum was desired, particularly in the red part of the spectrum, a standard 150 W tungsten halogen source (Osram Sylvania) was used. In all cases, the light was focused on to the end face of a fiber, leading to the input fiber taper, using a 20X microscope objective.

At the other end of the system, the output fiber was connected to a MicroSpec 2300i UV/Vis imaging spectrometer (Princeton Instruments). This instrument includes a turret with 150, 300, and 2400 grooves/mm (g/mm) gratings and a PIXIS 100 charge coupled device (CCD) camera

as a detector. During data collection, integration times generally ranged between 0.1 to 2 seconds, with multiple accumulations collected when better data quality was desired.

A syringe pump (Harvard Apparatus) was used to draw samples of IPA and water into the capillary. Flow rates ranged from 10-100 μL/min. Using deionized water, the flow rates were verified gravimetrically. The end of the capillary was placed in a sample solution, and the syringe pump was turned on, pulling the sample into the capillary and into the LCORR region. As a syringe pump was used in "pulling" mode, the waste was simply collected by the syringe connected to the capillary, as illustrated in Figure 3-10. Continuously drawing sample through the capillary at a set flow rate was one sample introduction method used. In another method, more appropriate for small sample volumes, sample was drawn into the capillary up to the LCORR region and then the flow was stopped. When comparing the two methods, in terms of noise and drift, no significant difference was observed.

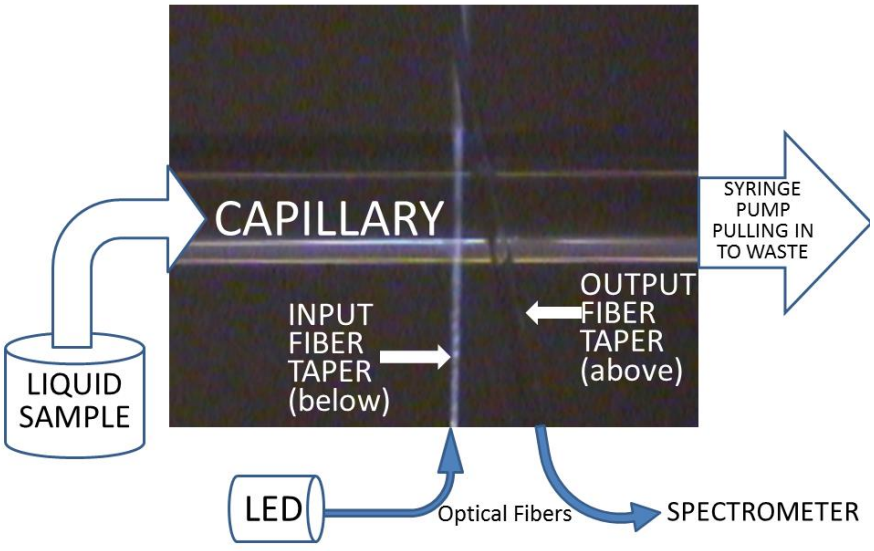

Figure 3-10 – Basic schematic of LCORR system used.

A sample solution mixing apparatus was assembled for experiments involving a dynamic RI. Shown in Figures 3-11 and 3-12, this involved a two-port flask situated on a stir plate. The two ports accommodated input and output capillaries. A second syringe pump (Bioanalytical Systems, Inc.) was used to feed the input capillary with solution or solvent to be added to the flask at a fixed rate. The output capillary was simply the sample intake for the LCORR system, drawing the mixed sample for analysis. The initial and final RI of the sample solution mixture was measured using an Abbe refractometer (Milton Roy Company). For the production of data as a function of RI, a good estimate of RI at any given time is necessary. A linear estimate for the rate d*n*/d*t* would be highly prone to error as the mixing flask has input and output flows operating at the same time. Therefore, to get a better fit, Equations 3-7 through 3-15 were used, factoring the gravimetrically verified input and output flow rates. Shown in Figure 3-13 is an example of a resulting d*n*/d*t* relationship. In this plot, an IPA/water mixture is being added to pure deionized water with an initial refractive index of 1.333.

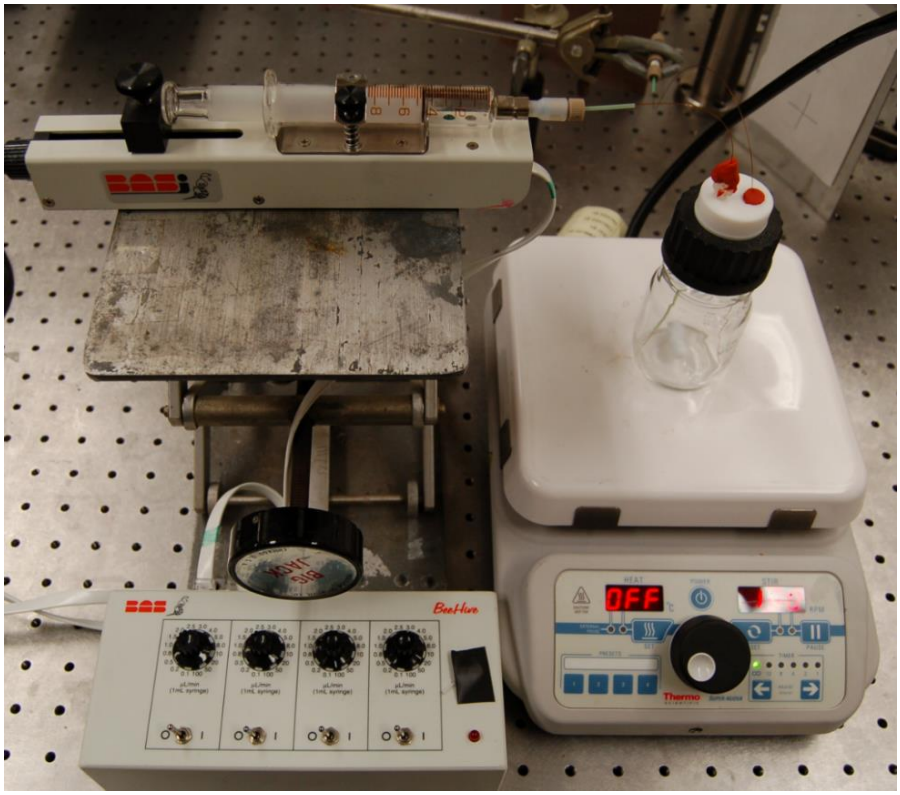

Figure 3-11 – Photo of sample mixing apparatus. On the left is a syringe pump containing of glass syringe of liquid to be added to the sample vessel sitting on the stir plate, to the right.

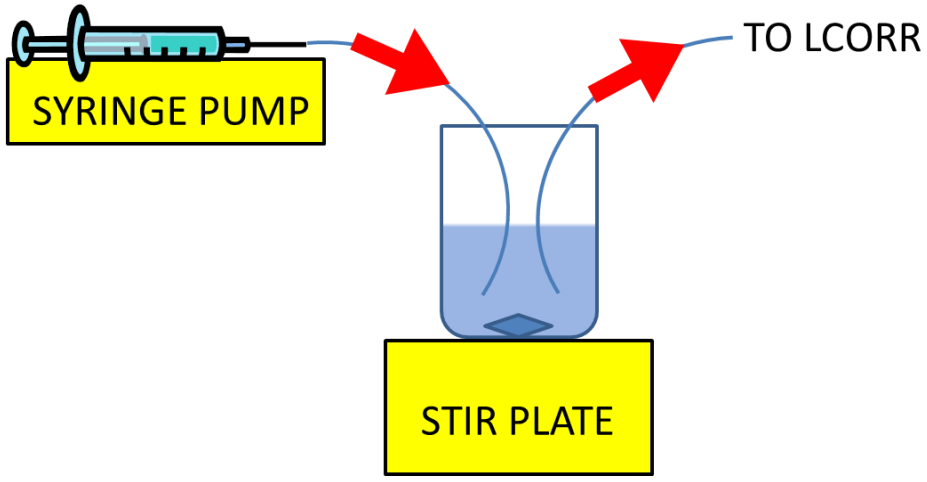

Figure 3-12 – Schematic of sample mixing apparatus pictured in Figure 3-11

Equation 3-7

$$\frac{d(n_{\text{samp}})}{dt} = n_{\text{add}}Q_{\text{add}} - n_{\text{samp}}Q_{\text{samp}}$$

Equation 3-8

$$\frac{d(n_{\text{samp}})}{dt} = -Q_{\text{samp}}(n_{\text{samp}} - n_{\text{add}}Q_{\text{add}})$$

Equation 3-9

$$\frac{d(n_{\text{samp}})}{n_{\text{samp}} - n_{\text{add}}Q_{\text{add}}} = -Q_{\text{samp}}dt$$

Equation 3-10

$$\int \frac{d(n_{\text{samp}})}{n_{\text{samp}} - n_{\text{add}}Q_{\text{add}}} = -\int Q_{\text{samp}}dt$$

Equation 3-11

$$\ln\left|n_{\text{samp}} - n_{\text{add}}Q_{\text{add}}\right| = -Q_{\text{samp}}t + C$$

Equation 3-12

$$n_{\text{samp}} - n_{\text{add}}Q_{\text{add}} = C\text{e}^{-Q_{\text{samp}}t}$$

Equation 3-13

$$@t = 0,\ \ C\text{e}^{Q_{\text{samp}}t} = C\ \ and\ \ n_{\text{samp}} = n_{\text{samp(init)}}$$

Equation 3-14

$$C = n_{\text{samp(init)}} - n_{\text{add}}Q_{\text{add}}$$

Equation 3-15

$$n_{\text{samp}} = n_{\text{add}}Q_{\text{add}} + [n_{\text{samp(init)}} - n_{\text{add}}Q_{\text{add}}]\text{e}^{-Q_{\text{samp}}t}$$

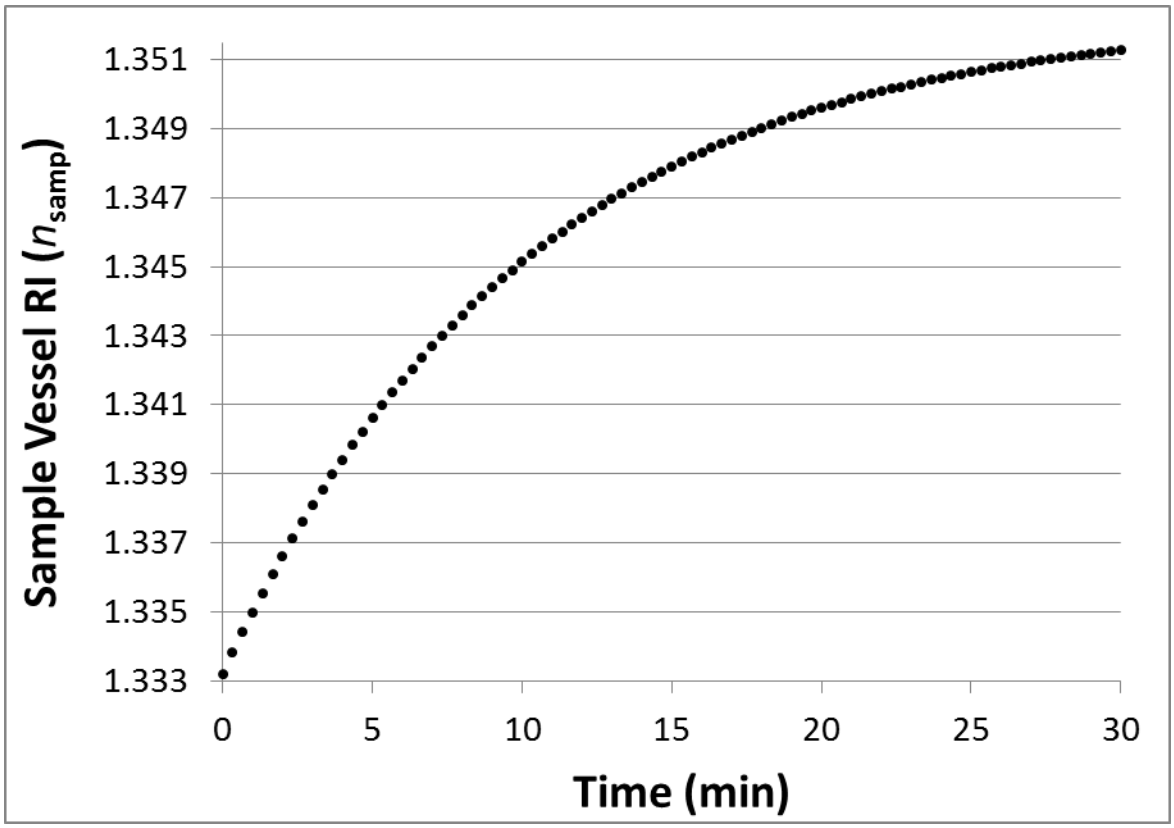

Figure 3-13 – Calculated sample RI vs. time

Unless otherwise specified, all chemicals were purchased from Sigma Aldrich. Isopropyl alcohol was of HPLC grade. Deionized water was purified to 18 MΩ using a Barnstead system.

Results and Discussion

Spectra obtained using the relatively high resolution, 2400 g/mm, grating produced clear and distinct interference fringes. Taking another look at Equation 3-5, these fringes were thought to be a function of the calculated spacing in resonance frequencies, $d\tilde{\nu}/dm$. To extract a periodic function, or frequency, from an interferogram, Fourier Transform (FT) analysis is commonly used. (Brigham, 1974) (Skoog, Holler, & Nieman, 1998) As discussed earlier, the original spectra were already in terms of "frequency" in wavenumbers, and therefore the FT output can be thought of simply as fringe spacing, or $d\tilde{\nu}/dm$.

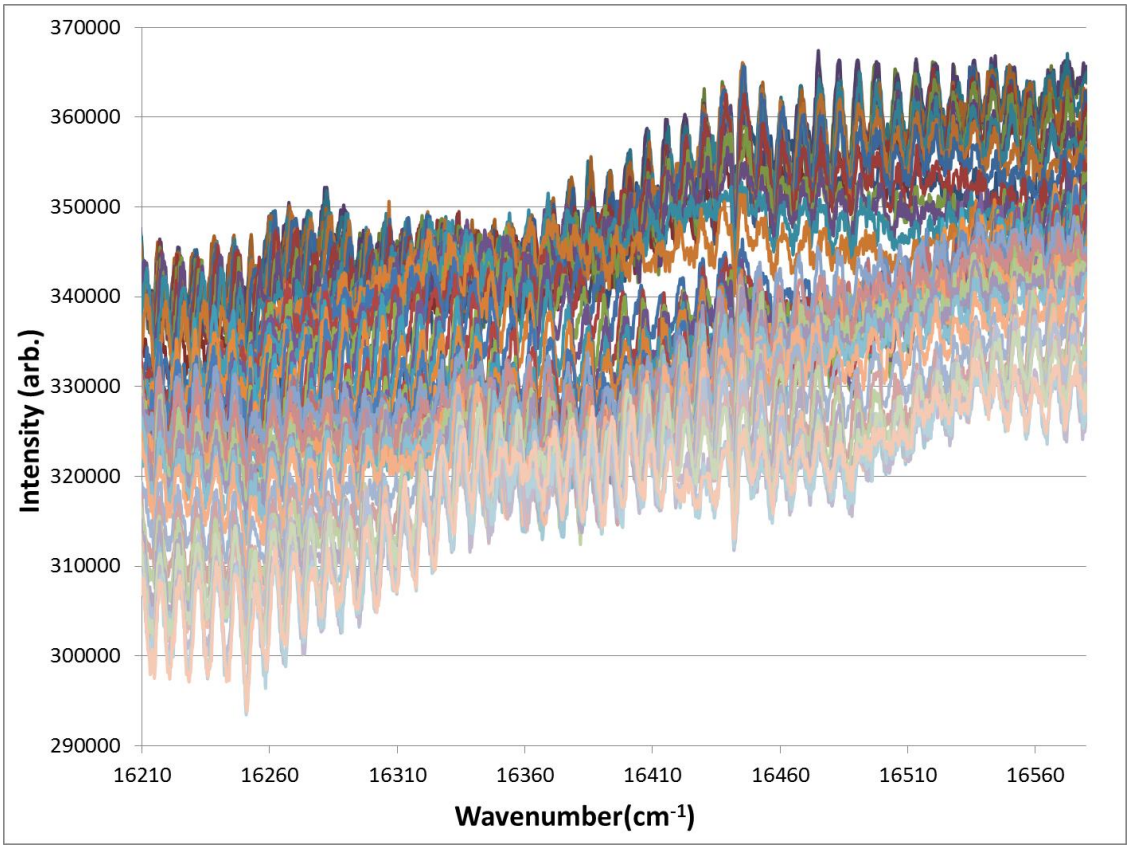

Figure 3-14 – Raw output using 2400g/mm grating for samples of 40 incremental RI steps.

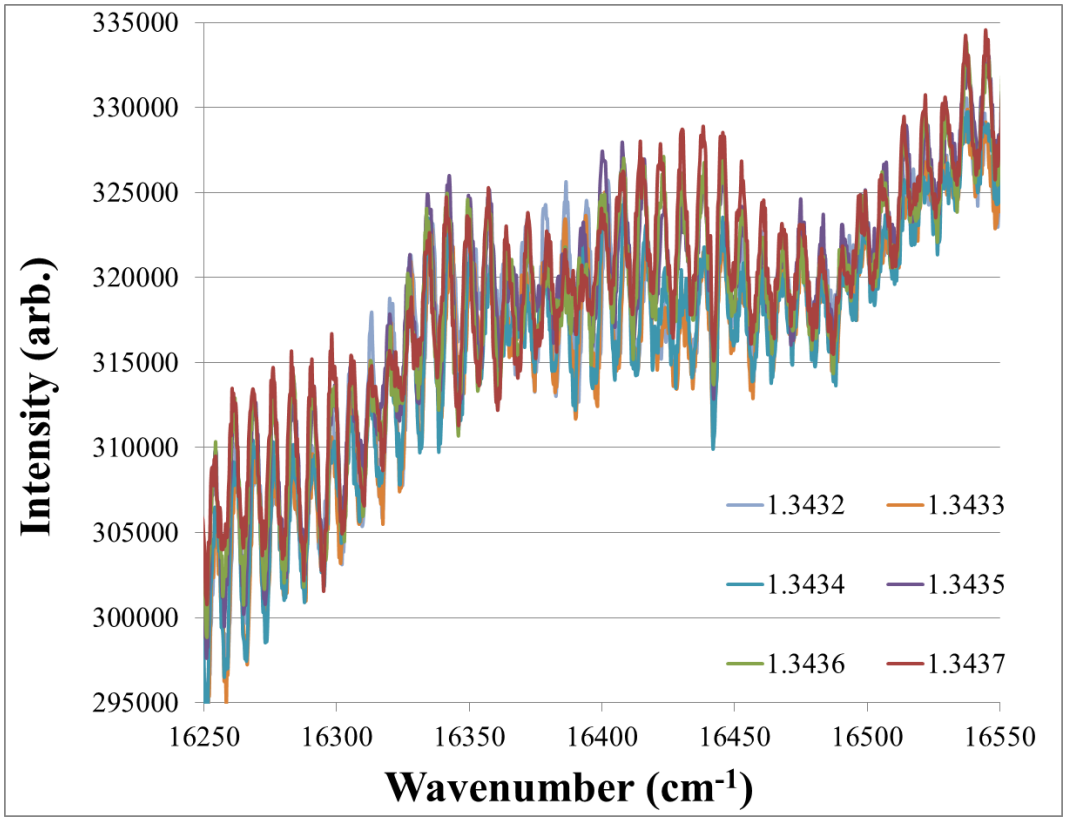

Figure 3-15 – For clarity, only six of the output spectra from Figure 3-14 were selected for display.

Using a mixing apparatus, the sample mixing flask ranged from an RI of 1.3432-1.3409 over the course of 60 minutes. Each minute, a spectrum was collected. The collection of spectra is shown in Figure 3-14. As this output is very complex, the first six spectra are shown in Figure 3-15, ranging from 1.3432-1.3437. The complexity remaining in this figure illustrates the dynamic response of the output as a function of RI; however the data is clear enough to see an interference pattern. If Figure 3-15 were studied carefully, one would measure the spacing between the peaks, or fringes, to be approximately 7-9 cm^{-1}. On taking a closer look at Equation 3-5, plugging in 1.27 x 10^5 nm for the radius of the resonator (this is the average radius inside the 4 μm thick wall of a 250 μm ID capillary) and 1.455 for n_{eff} (estimating a slight decrease from the pure fused silica RI of 1.457 due to aqueous sample contribution), the calculated $d\tilde{\nu}/dm$ fringe spacing ranges from

7.90 cm^{-1}/fringe, for the critical mode (propagating at the critical angle), to 8.61 cm^{-1}/fringe for the minimum-order mode (taking the shortest possible ray path). (Daly, 1984) This agrees with the observed spacing in interference fringes from Figure 3-15.

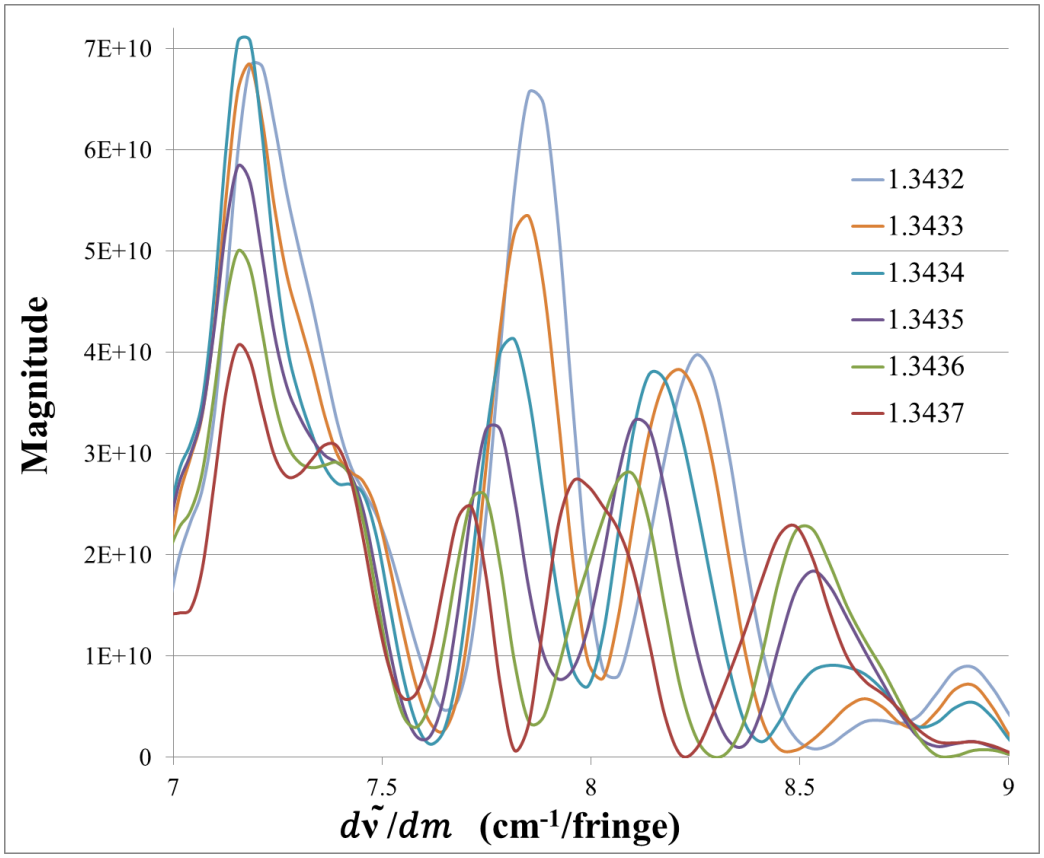

Figure 3-16 – Fourier transform output of the six spectra pictured in Figure 3-15. © 2012 American Chemical Society

Having verified Equation 3-5 to likely be a valid estimation of interference fringe spacing, the variables were studied further. In particular, as the dynamic n_{eff} term represents effective refractive index it gives the $d\tilde{\nu}/dm$ spacing a variable nature. Due to the inverse relationship between $d\tilde{\nu}/dm$ and n_{eff}, it can be expected that an increase in sample refractive index, for example, would result in a decrease in $d\tilde{\nu}/dm$ fringe spacing. With this dynamic nature, plotting the Fourier

transform was an appropriate means to express $d\tilde{\nu}/dm$ and its response to external factors such as RI. Shown in Figure 3-16 is the FT power spectrum of the seven raw spectra displayed in Figure 3-15. The peaks in this plot represent the most abundant periodic functions, or $d\tilde{\nu}/dm$ fringe spacing, in the raw spectra. It is observed that the abundant $d\tilde{\nu}/dm$ peaks are located approximately in the range of 7-9 cm^{-1}/fringe. With the exception of those around 7.2 cm^{-1}/fringe, the peaks also agreed approximately with the 7.90-8.61 cm^{-1}/fringe calculated earlier using Equation 3-5 with the estimated resonator parameters. Also worth noting at this point is the clear shifting of peak locations towards smaller $d\tilde{\nu}/dm$ values with an increasing sample RI. This also agrees with Equation 3-5, as the relationship between n_{eff} and $d\tilde{\nu}/dm$ is inverse.

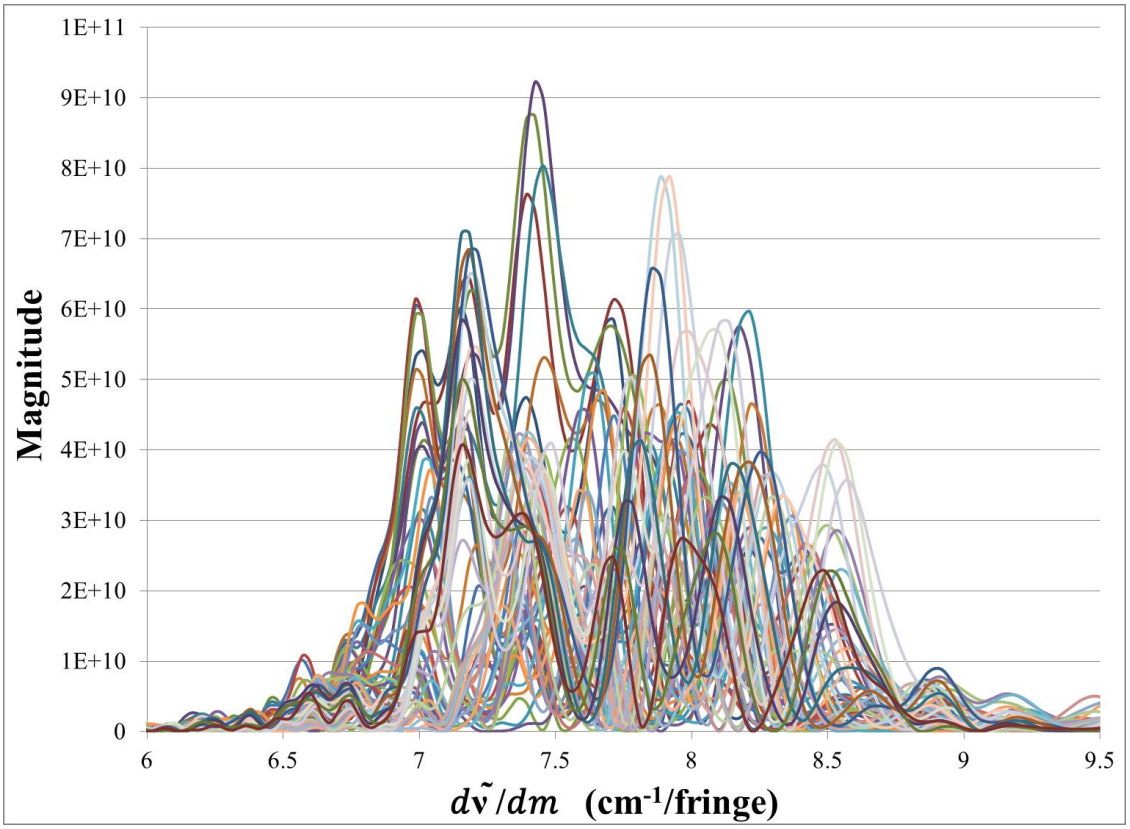

Figure 3-17 – Fourier transform output of all 40 spectra pictured in Figure 3-14.

Due to the complexity and overlapping nature of all 40 FT plots, shown in Figure 3-17, for the complete series of RI steps, a three-dimensional graph is necessary for a clear display. Shown in Figure 3-18 is a surface plot, where $d\tilde{\nu}/dm$ is still displayed on the x-axis, but magnitude is now shown on the z-axis in shades of greyscale in the color-mapping. On the surface plot, the y-axis now represents the RI range of the 40 original spectra. In this plot, there is a great deal of complexity with regard to both peak location and intensity. However, at least one relatively clear relationship can be observed, particularly in the range of 7.5-8.5 cm^{-1}/fringe. Shifting of peak locations towards smaller $d\tilde{\nu}/dm$ values with an increasing n_{core} can be seen with an average relationship of -400 (cm^{-1}/fringe)/RIU. Although this agrees with the inverse relationship between $d\tilde{\nu}/dm$ and n_{eff}, the shift is vastly greater than theoretically predicted using the same equation. If n_{eff} were hypothetically assumed to be equal to n_{core}, something impossible as it would assume all light intensity was in the evanescent field and none was guiding around the wall circumference, the $(d\tilde{\nu}/dm)/n_{eff}$ would still be only around -6 (cm^{-1}/fringe)/RIU.

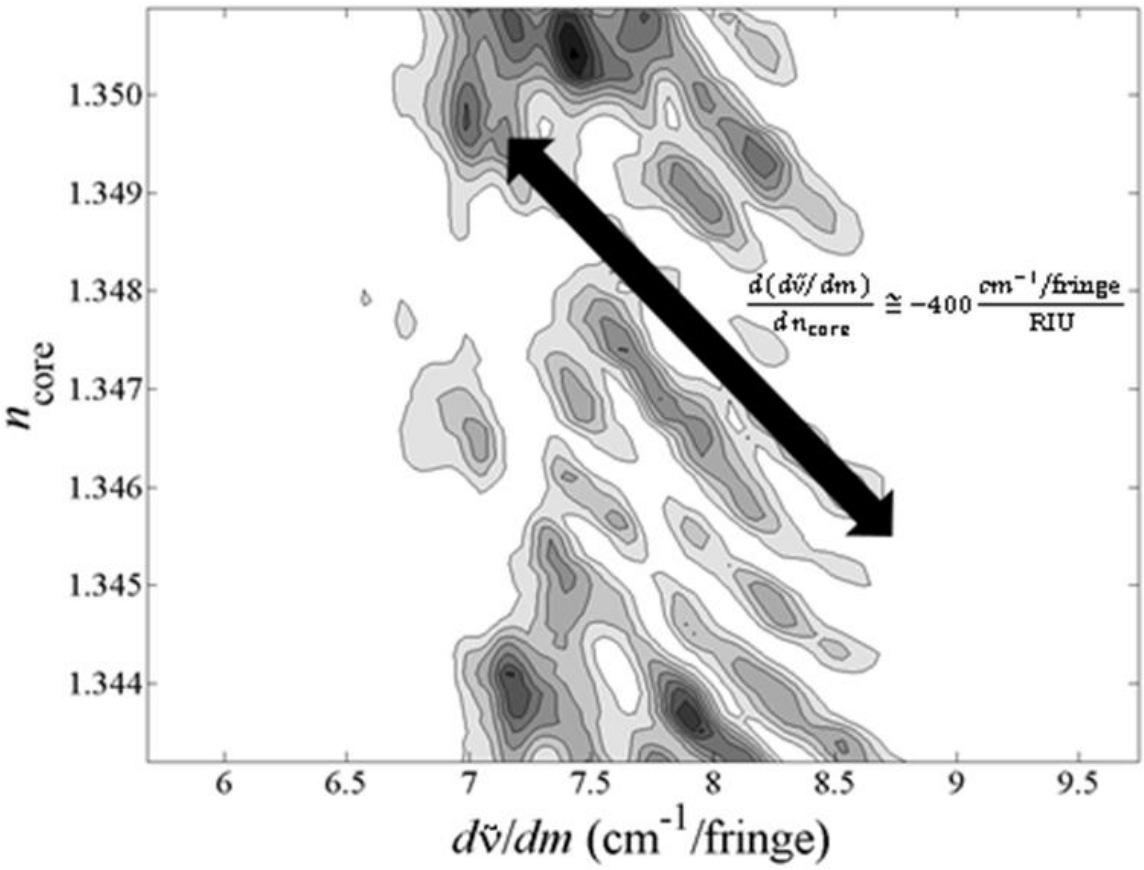

Figure 3-18 – Surface plot of Figure 3-17. For clarity, magnitude is expressed on the z-axis, as elevation expressed through greyscale mapping. A relationship can be observed as a peak shifting of approximately -400 (cm^{-1}/fringe)/RIU. © 2012 American Chemical Society

To explain the greatly enhanced RI sensitivity of the broadband LCORR over the theoretical single mode/single wavelength shift predicted in Equation 3-5, several optical mechanisms should be considered. A change in core RI will alter the allowed angles of reflected rays of light, according to Snell's Law, Equation 3-1. With a shift in angles come varying evanescent penetration depths and relative field fractions in each material, per Equations 1-4 and 1-5. One possibility for the greatly enhanced RI sensitivity is that a small number of dominant modes are present and are altered significantly by the simultaneous optical properties affected by RI. Another possibility is that an unknown number of optical modes are present and the

appearance of Figure 3-18 is a secondary interference pattern resulting from the varying degrees of overlap between these modes. With either scenario, the most straightforward means of quantification of an RI shift would be to track the location of one or more of these peaks. As the peak center location recycles, according to the surface plot, approximately every 0.001 RIU, this type of analysis would only be valid for a small RI range. In many detection scenarios this would be acceptable, where detecting a shift in RI is all that is needed. An example would be a specific binding assay application, where only the analyte of interest is expected to adsorb to the surface and cause the potential RI shift. The majority of conventional ring resonator devices and methods only detect an RI shift, and are therefore limited in this manner. (Fan, Advanced Photonic Structure for Biological and Chemical Detection, 2009) (Suter & Fan, Handbook of Optofluidics, 2010) To calibrate for absolute RI detection, all peak locations and intensities would be included. A chemometric approach could be taken, in which case RI would be correlated to mathematical fitting of either the interference spectra or the resulting FT plots. (Dahlberg, Lee, Wenger, & Vargo, 1997) (Pereira, et al., 2008)

In order to estimate a detection limit for a simple FT peak tracking method, the noise of the FT peak location was determined. This was performed by drawing a single RI solution through the capillary for 30 minutes and collecting an interference spectrum once per minute. From these spectra, FT plots were produced, and the center of one particular dominant peak was plotted as a function of time, displayed in Figure 3-19. A minimum detectable response is generally accepted to be a signal to noise ratio of three. (Skoog, Holler, & Nieman, 1998) Based on this acceptance, Equation 3-16 can be used to estimate a detection limit. In this equation, the standard deviation of the noise is required. The noise is taken simply to be the baseline $d\tilde{\nu}/dm$ value throughout the 30 minute period, 3.86 x 10-4 cm^{-1}/fringe, as theoretically no RI shifting or other external influences

are acting on the $d\tilde{\nu}/dm$ during this time. Therefore, the minimum detectable shift, three times this value, is 1.16 x 10^{-3} cm^{-1}/fringe. Based on a sensitivity of -400 (cm^{-1}/fringe)/RIU shown earlier in Figure 3-18, the detection limit using a peak tracking method is estimated to be 2.9 x 10^{-6} RIU.

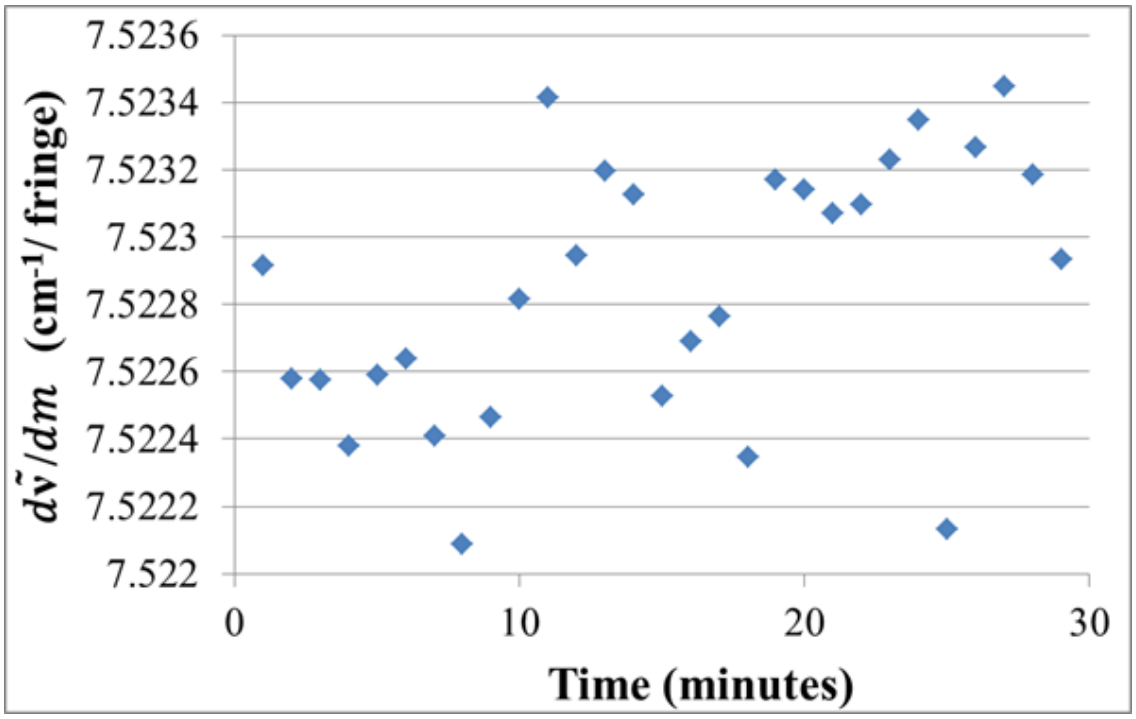

Figure 3-19 – FT peak position as a function of time for a fixed sample solution, used for noise determination.

Equation 3-16

$$Detection\ Limit(\mathrm{RIU}) = \frac{3\sigma_{\mathrm{noise}}(\mathrm{cm^{-1}fringe^{-1}})}{Sensitivity(\mathrm{cm^{-1}fringe^{-1}RIU^{-1}})}$$

Conclusion

In this chapter, a novel method for refractive index detection in a ring resonator was presented. Based on the extraction of interference fringe components from a broad spectrum of resonant wavelengths, RI detection limits were presented on the order of 10^{-6} RIU. This is comparable to existing RI sensing devices, and therefore presents an alternative method worthy of further study.

References

Arnold, S., Keng, D., Shopova, I., Holler, S., Zurawsky, W., & Vollmer, F. (2009). *Opt. Express, 17*, 6230-6238.

Boleininger, A., Lake, T., Hami, S., & Vallance, C. (2010). *Sensors, 10*, 1765-81.

Brigham, E. (1974). *Fast Fourier Transform.* Englewood Cliffs: Prentice-Hall.

Dahlberg, D., Lee, S., Wenger, S., & Vargo, J. (1997). *Appl. Spectrosc., 51*, 1118-1124.

Dakin, J., & Culshaw, B. (1988). *Optical Fiber Sensors.* Boston: Artech House.

Daly, J. (1984). *Fiber Optics.* Boca Raton: CRC Press, Inc.

Fan, X. (2009). *Advanced Photonic Structure for Biological and Chemical Detection.* Dordrecht: Springer.

Fan, X., White, I. S., Zhu, H., Suter, J., & Sun, Y. (2008). *Anal. Chim. Acta., 620*, 8-26.

Fan, X., White, I., Zhu, H., Suter, J., & Oveys, H. (2007). *Proc. SPIE*, 6452-18.

Gibb, T. (1942). *Optical Methods of Chemical Analysis.* New York: McGraw-Hill Book Company, Inc.

Harrick, J. (1979). *Internal Reflection Spectroscopy.* Ossining: Harrick Scientific Corporation.

Iqbal, M., Gleeson, M., Spaugh, B., Tybor, F., Gunn, W., Hochberg, M., et al. (2010). *IEEE J. Sel. Top. Quantum Electron., 16*, 654-661.

Katz, E. (1998). *Handbook of HPLC.* New York: Marcel Dekker.

Leidner, L., Zourob, M., & Lakhtakia, A. (2010). *Optical Guided-wave Chemical and Biosensors II.* Berlin: Springer-Verlag.

Liang, W., Huang, Y., Xu, Y., Lee, R., & Yariv, A. (2005). *Appl. Phys. Lett, 86,* 151122.

Malitson. (1965). *J. Opt. Soc. Am., 55,* 1205-1209.

NIST. (n.d.). *Speed of Light in Vacuum*. Retrieved 01 04, 2013, from The NIST Reference on Constants, Units, and Uncertainty: http://physics.nist.gov/cuu/index.html

Oates, T., & Burgess, L. (2011). *Appl. Spectrosc., 65,* 1187-1192.

Oates, T., & Burgess, L. (2012). *Anal. Chem., 84,* 7713-7720.

Palmer, J. (2006). *How to Brew.* Boulder: Brewers Publications.

Pereira, A., Pontes, M., Neto, F., Santos, S., Araujo, M., & Galvao, R. (2008). *Food Res. Int., 41*, 341-348.

Rashed, R. (1990). *Isis, 81,* 464-491.

Scott, R. (1996). *Chromatographic Detectors: Design, Function, and Operation.* New York: Marcel Dekker.

Shopova, S., White, I., Sun, Y., Zhu, H., Fan, X., Frye-Mason, G., et al. (2008). *Anal. Chem.*, 2232-2238.

Skoog, D., Holler, F., & Nieman, T. (1998). *Principles of Instrumental Analysis.* United States: Thomson Learning.

Skurnick, R., & Javadi, M. (2006). *Math. and Comp. Edu., 40,* 70-73.

Suter, J., & Fan, X. (2010). In A. Hawkins, & H. Schmidt, *Handbook of Optofluidics* (pp. 11(1-29)). Boca Raton: Taylor & Francis.

Suter, J., White, I., Zhu, H., & Fan, X. S. (2008). *Biosens. Bioelectron., 23,* 1003-1009.

Vollmer, F., & Arnold, S. (2008). *Nat. Methods, 5,* 591-596.

Zhu, H., White, I., Suter, J., Dale, P., & Fan, X. (2007). *Opt. Express, 15,* 9139-9146.

Zhu, H., White, I., Suter, J., Zourob, M., & Fan, X. (2007). *Anal. Chem, 79,* 930-937.

CHAPTER 4

Device Characterization and Optimizations

Introduction

In its current form, the broadband LCORR is very much still in the basic research phase. On a number of fronts, improvements can be made to the design and operation of the device. In order to make significant improvements, however, experimentation and interpretation of the device's functionality is a necessary prerequisite. The influence of wall thickness on results is one such topic of study. Others include sources of noise, resolution limitations, possible fluidic improvements, methods of etching and fabrication, and the dynamic range of detection.

Wall Thickness

Revisiting Figure 1-9, the dependence of wall thickness on mode distribution is reemphasized. The mechanisms described earlier for both absorbance and refractive index detection are functions of the evanescent penetration of the sample core. (Oates & Burgess, 2011) (Oates & Burgess, 2012) For this penetration to occur, internal reflection must occur off of the surface sharing a boundary with the sample. (Harrick, 1979)

The relative abundance of waveguide modes, interacting with both wall surfaces, increases with a decreasing wall thickness. Fan and coworkers found a wall thickness of approximately 4 μm or less to be necessary to achieve useful sample core sensitivity in LCORRs of approximately 100 μm in diameter. (Fan X. , White, Zhu, Suter, & Oveys, 2007) (Suter J. , White, Zhu, & Fan, 2008) (Fan X. , White, Zhu, Suter, & Sun, 2008) (Fan, Advanced Photonic Structure for Biological and Chemical Detection, 2009) (Suter & Fan, Handbook of Optofluidics, 2010) As these are smaller in diameter than the 250 μm LCORRs used in this current work, the maximum wall thickness is expected to be a bit thicker. For an estimation, the necessary wall thickness of 4 μm

represented 4% of the 100 μm capillary diameter used by Fan and coworkers, while the same aspect ratio in a 250 μm capillary would be achieved with a 10 μm wall thickness.

Using dilute buffered HF as an etchant, as described earlier in the experimental sections of Chapters 2 and 3, wall thinning down to approximately 4 μm was achieved. Thinning beyond this produced walls that were very fragile and thus difficult for experimental use.

In order to accurately determine the RI sensitivity as a function of wall thickness, all other variables must remain constant. This includes the exact positioning of the input and output fiber tapers. Therefore, any method in which the LCORR device is disassembled would be unsuitable. This would obviously be the case if successive external etchings were performed on the capillary surface. For the determination of wall thickness sensitivity, an internal etching technique was used. This basically entailed the use of 9% Buffer-HF (Transene) in place of a sample solution. This etchant was shown in Chapter 2 to produce a fairly linear etch rate with time, even in the case of external etching- where a relatively small volume of etchant concentration of HF was used. In the case of internal etching, the etchant is continuously replenished simply by having the sample pump operating. Therefore, a virtually constant HF concentration and etch rate is available. With a constant etch rate, wall thickness can be very accurately estimated at any point in time, without the need for additional measurement. To determine the etch rate, a fixed flow rate of 4 mL/hr was set, and the time required to completely etch through the wall of the capillary was determined. Occurring at 210 minutes, this revealed an etch rate of 0.167 μm/min, based on Equation 4-1.

Equation 4-1

$$Internal\ Etch\ Rate\ \left(\frac{\mu\text{m}}{\text{min}}\right) = \frac{Wall\ Thickness\ (\mu\text{m})}{Time\ to\ Etch\ Through\ (\text{min})}$$

To determine RI sensitivity, an unetched capillary was positioned with the fiber tapers. An RI mixing apparatus, per Chapter 3, was set up with water and IPA for a continuously changing RI. Briefly, a two port flask containing IPA and water was mixed on a stir plate. A capillary leading into the flask from a syringe pump introduced additional sample, in this case deionized H_2O, to slowly change the RI of the mixing flask contents. The flow rate of the syringe pump introducing additional H_2O was verified gravimetrically. A second capillary in the flask was the sample intake for the LCORR, ultimately leading to the waste syringe. Spectra were collected over an RI range and processed in the same manner as described in the previous chapter.

A series of fixed-time etches were performed, each followed by an RI sensitivity determination. Shown in Figure 4-1 is a plot of RI sensitivity as a function of wall thickness. Quite a bit of variability is present in this plot, but the overall trend does confirm an inverse relationship between wall thickness and sensitivity. Both this relationship and its variability are expected. As described in detail earlier, the thinner walls are expected to encourage core-interacting waveguide modes, thus increasing core sensitivity. Although the number of experimental variables was reduced by using an internal-etching method for wall thinning, leaving the LCORR untouched on the outside, a number of complex optical relationships affect RI sensitivity. Described in more detail in Chapter 3, these include the varying modal distribution of resonating light, the varying field fractions of evanescent penetration into the resonator materials, and the complex manner in which the multiple propagating modes and wavelengths interfere with each other.

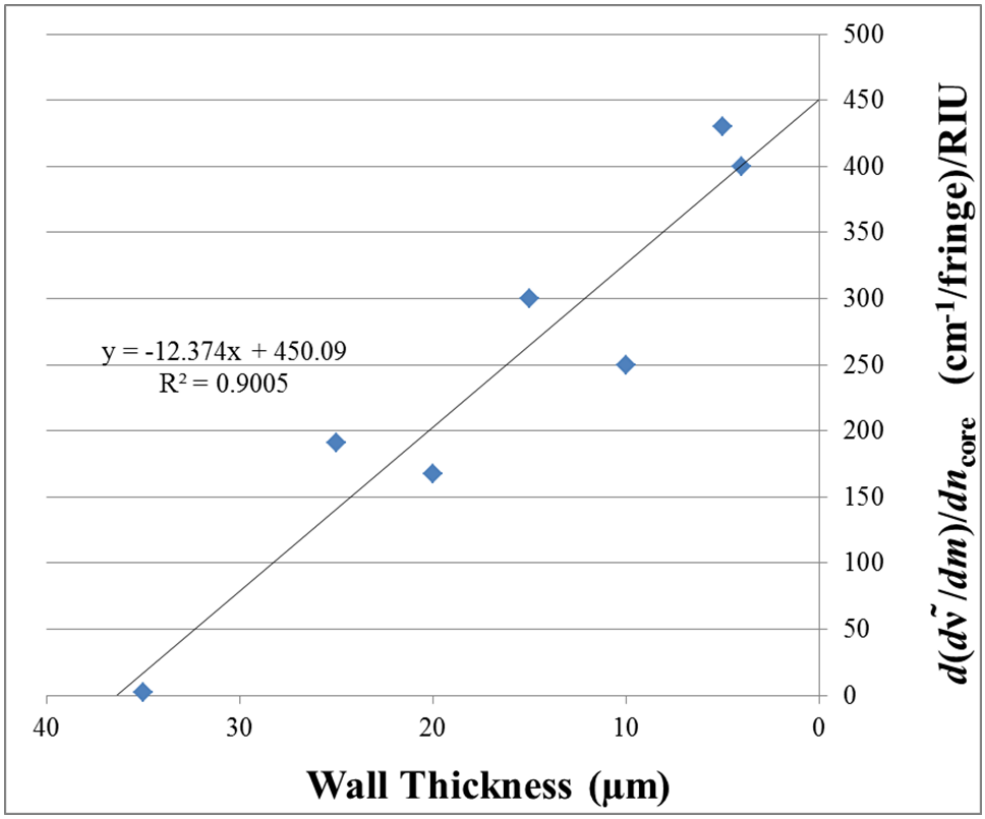

Figure 4-1 – RI sensitivity vs. wall thickness.

Internal vs. External Etching

On choosing a capillary-based ring resonator format, the next decision comes in the method to use for wall thinning. Capillaries with very thin walls are not commercially available partly due to their limited usefulness beyond LCORRs, which are still very much in the research phase. Although one might argue that LCORRs could jump into commercialization if not for this unavailability, another limitation is the fragility of very thin-walled capillary. Capillary thinning methods are generally based on some degree of chemical etching and also possibly heating and pulling. (White, Oveys, & Fan, 2006) (Fan X. , White, Zhu, Suter, & Oveys, 2007)

In a pulling method, a capillary of larger diameter is heated and pulled to reduce its diameter. Although capillaries with thin (single microns) walls are not commercially available, larger capillaries with the proper standard dimension ratio (SDR) are available. This is simply the ratio of the outside diameter over the wall thickness. (Standard Dimension Ratio - SDR, 2012) If a capillary can be pulled down to 1:10 of its original diameter, then the original wall thickness can be approximately 10 times greater than the desired final wall thickness. For example, if a 100 μm OD capillary with a 10 μm wall thickness were desired, a 1 mm OD capillary with a 100 μm thickness wall could be the starting material. This concept is illustrated in Figure 4-2, where the largest capillary has the same aspect ratio as the smaller two, which could have been fashioned from the larger one by heating and pulling.

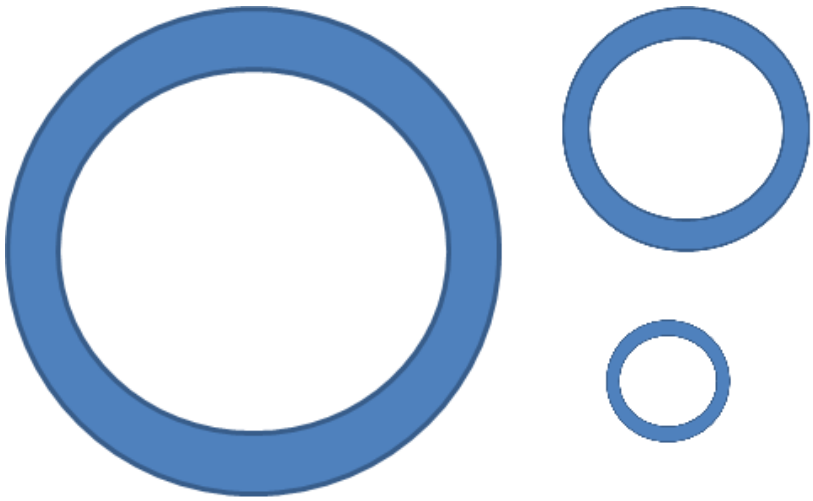

Figure 4-2 – If the capillary on the left maintains its standard dimension ratio (wall thickness to overall diameter) when heated and pulled to a smaller diameter, the wall thickness is reduced.

Pulling as a method for capillary thinning does have several limitations. When reducing an object down to $1/10^{th}$ or $1/20^{th}$ of its original dimensions through melting and pulling, some possibly significant degree of variability in the exact pulled dimensions is expected. This is a function of the pulling instrument or apparatus used. In a pulled capillary, both the inner and outer

diameters have obviously changed from their original dimensions. Therefore, to determine the wall thickness optically, an axial measurement (looking down the bore of the capillary) is necessary for good accuracy. Taking an axial measurement requires cleaving, and therefore destroying, of the capillary. (White, Oveys, & Fan, 2006) Instead, to estimate diameter without optically measuring each thinned capillary, a series of capillaries thinned with identical method parameters would need to be optically measured and sacrificed, with a standard deviation produced for error estimation.

In addition to the limitations with regard to measurement and reproducibility, the flow dynamics though a pulled capillary can complicate construction and operation. As shown in Figure 4-3, the pulled section has a narrow "waist," where the inner diameter is much smaller than that of the sections before and after. This change in inner diameter presents a dramatic change in linear velocity and a potentially significant backpressure. Fan and coworkers overcame this by carefully cleaving the thinned section and discarding the ends. (White, Oveys, & Fan, 2006) (Fan X. , White, Zhu, Suter, & Oveys, 2007) (Fan X. , White, Zhu, Suter, & Sun, 2008) This is a manual process and must be done with extreme care. The end result is also subject to some degree of variability, as a function of how the capillary was cleaved.

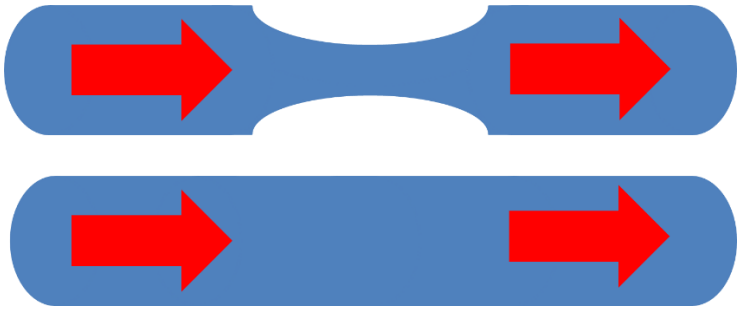

Figure 4-3 – The heated and pulled capillary, on top, still has the original dimensions at both ends, thus creating a flow restriction at the taper. This is not seen with the capillary on bottom, which could be envisioned as being etched rather than pulled.

Etching methods are also prone to a number of challenges. These vary based on the etch method, whether it be internal or external. As for etching in general, the concentration of etchant is a variable in the etch rate, and therefore a potential for variability and/or error, depending on how the capillary dimensions are determined. One of the most significant issues with etching is the very hazardous and corrosive nature of etchant chemicals such as hydrofluoric acid. Very deliberate and meticulous safety measures must be taken to ensure the safety of the operators in these methods. (UW, 2009)

External capillary etch methods have specific advantages and disadvantages. Internally etched capillaries can be fully installed in a ring resonator device prior to etching. Externally etched capillaries, on the other hand, must be separately etched, then installed. Depending on the installation method permanence (e.g., epoxies used), external etching is unlikely to be feasible after installation.

In terms of procedural robustness, the internal etching method is very straightforward and repeatable, as the etchant is pulled in though the sample line and rate is controlled simply by flow rate and concentration. With external etching methods, the etchant volume is generally finite, and therefore theoretically of decreasing concentration. If a constant etch rate were desired, three different approaches could be taken- replenishing the etchant periodically, using a large etchant volume, or placing the capillary somehow in a larger flow stream of etchant.

For dimensional determination, both internal and external etching methods benefit from the fact that only one surface is being modified. With external etching, for example, the internal diameter can be determined by sacrificing an adjacent piece of capillary for an axial measurement. Therefore, after etching, only the external diameter would need to be determined in order to

estimate the new wall thickness. This benefit is likely not as valuable for internally etched capillaries, as the external diameter is generally easier to measure optically. In this case, internal diameter, and thus wall thickness, can be estimated from a sacrificial etch rate determination, as described in the "Wall Thickness" section, above.

In the following section, the theoretical sensitivity of internally versus externally etched capillaries will be investigated in more detail. Briefly, internally etched capillaries are apt to be less sensitive in the capillary core.

While the etch process when using dilute Buffer-HF is steady and slow, literally hours, some amount of imperfection and/or roughness is still expected at the surface. (Deyl & Svec, 2001) (Fan, Advanced Photonic Structure for Biological and Chemical Detection, 2009) Shown in Figure 4-4 is the axial profile of a surface etched capillary with an exaggerated amount of surface roughness. The two illustrated ray paths represent a waveguide mode on the left and a whispering gallery mode on the right. In the figure, although both modes are affected by the outer wall surface roughness, the WGM is severely attenuated as a result. This is due to its reflection mode being exclusive to the outer surface.

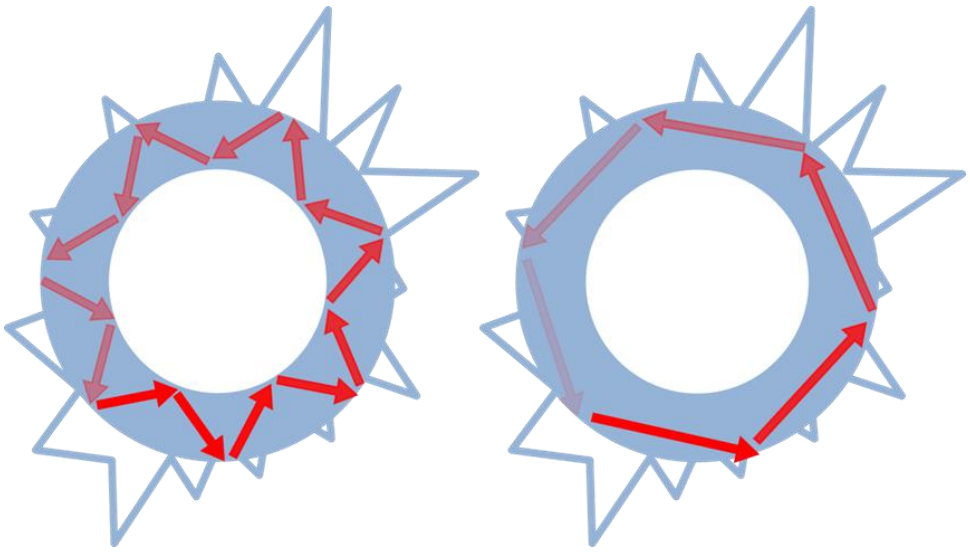

Figure 4-4 – Exaggeration of external surface roughness as a result of external etching. The whispering gallery mode, pictured on the right, is much more susceptible to attenuation as its reflection is entirely off of the outer surface.

In contrast to Figure 4-4 is an internally etched capillary, shown in Figure 4-5. In this scenario, the WGM mode, on the right, is relatively free to resonate by reflecting off of the smooth and blemish-free outer surface. The waveguide mode reflecting off of both the inner and outer wall surface is still somewhat hindered this case.

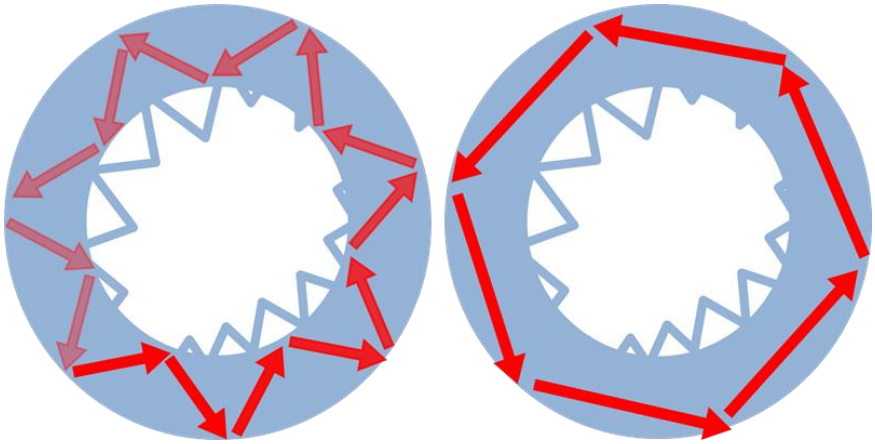

Figure 4-5 – Exaggeration of internal surface roughness as a result of internal etching. In contrast to Figure 4-4, the whispering gallery mode (Right) is unaffected by the internal surface and is therefore allowed to build strong resonance.

An experiment was devised to confirm this theoretical model. To exclusively filter out waveguide modes, introducing a very strong absorber into the sample core should be effective. Through absorption, this would cause the attenuation of modes reflecting off of the inner wall surface and evanescently penetrating the core. Preventing the resonance of these modes should allow only WGMs, without any core interaction, to dominate. Shown in Figure 4-6 is the axial profile of two capillaries, one internally etched and the other, externally. In this figure, a strong absorber is present at the inner wall surface. From these illustrations, the internally etched capillary will still support non-interacting WGM resonance modes while the externally etched capillary will support much less of these modes. Therefore, the expected result of the experiment is to see greater resonance achieved for the internally etched capillary.

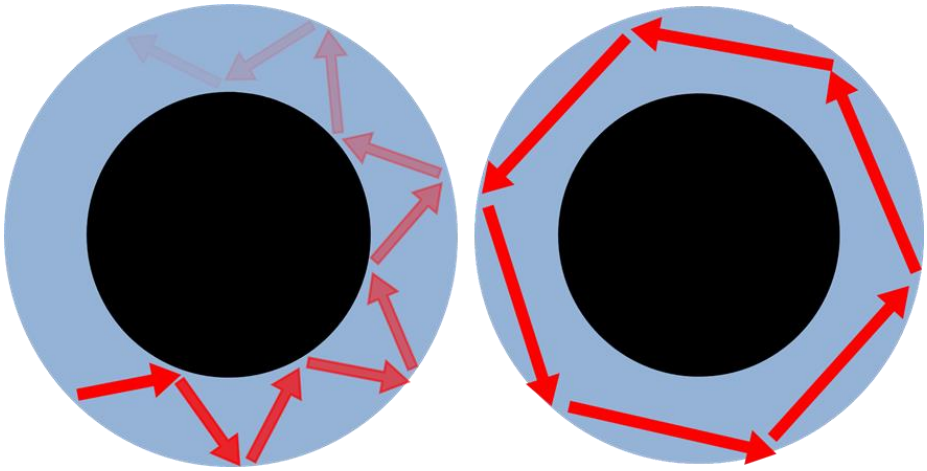

Figure 4-6 – This figure neglects surface roughness and simply compares a waveguide mode (Left) to a whispering gallery mode (right) in the presence of a strong absorber in the capillary core. As the whispering gallery mode is unaffected by the core, it is allowed to resonate freely, while the waveguide mode is attenuated.

Shown in Figure 4-7 is the result of the above experiment. As expected, the FT for the concentrated dye solutions is relatively more intense for the internally etched capillary. Rather surprising, however, was the resonance clarity and intensity relative to that seen with lower

concentration dye solutions. This is possibly a result of the detector's greater ability to resolve the interference peaks with the simpler spectra that are produced when fewer propagating modes are present.

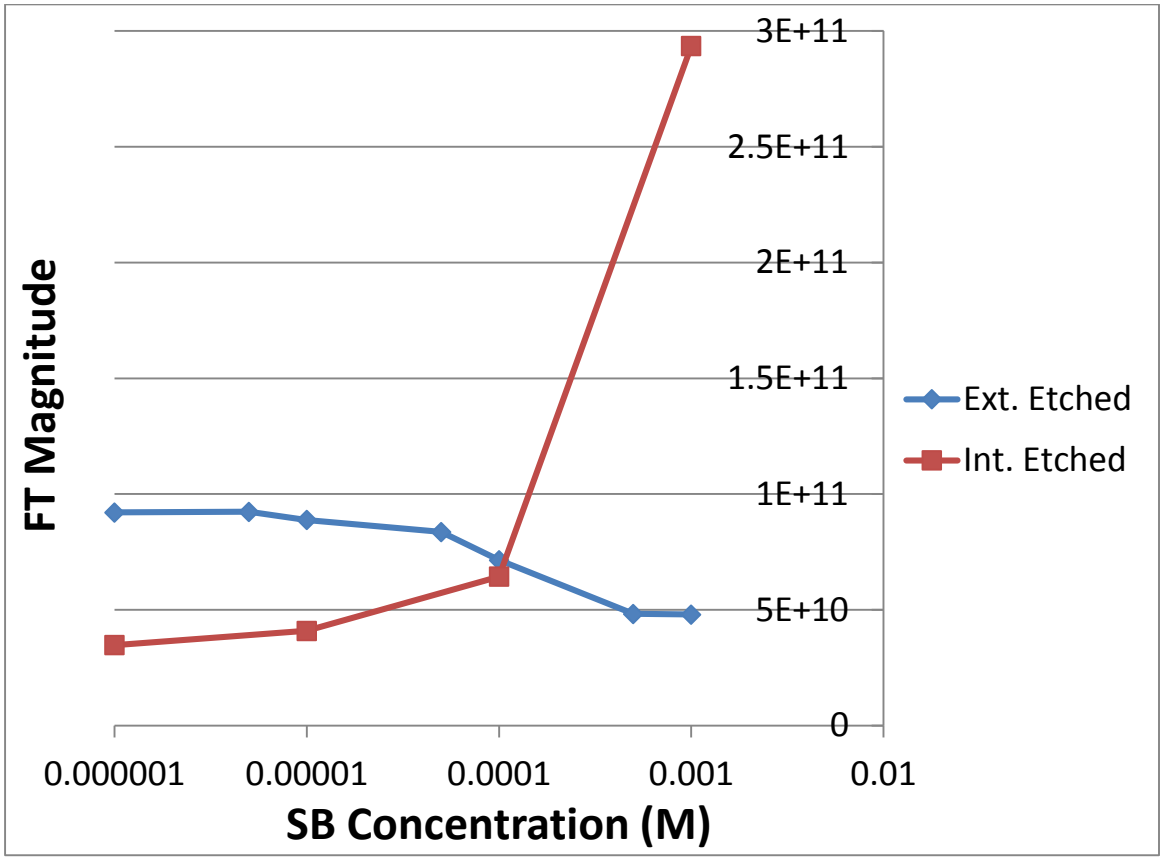

Figure 4-7 – Maximum FT peak intensity as a function of SB dye concentration in the core. As the internally etched capillary is more supportive of whispering gallery modes, the resonance clarity is actually strengthened as dye concentration is increased and waveguide modes are rapidly attenuated. In contrast, the externally etched capillary is less supportive of whispering gallery modes and appears to lose resonance with increasing dye concentration.

There are various reasons for choosing a particular LCORR fabrication method. If that method involves chemical etching, there are also reasons for choosing between internal and external etching. One factor needing to be taken into account is how the particular surface being etched will affect the relative abundance of different types of propagating modes, as demonstrated in the previous experiment.

FT Methods

As an additional validation of the data analysis method based on Fourier Transform extraction of fringe components, the average FT peak position was investigated. The original unetched capillary had a 250 μm inner diameter and a 320 μm outer diameter. Therefore, with external etching, as in Chapter 3, the thinned capillary approached an overall diameter of just over 250 μm. The experimentally found fringe spacing of 7.6-8.4 cm^{-1}/fringe agreed with Equation 3-5 in the case of a resonator of that particular diameter. The relationship between fringe spacing and resonator diameter is shown in Equation 3-5 to be inverse. As shown in Figure 4-8, with the larger diameter in the internally etched LCORR, the dominant $d\tilde{\nu}/dm$ fringe spacing dropped to 5.5-7.0 cm^{-1}/fringe as the diameter approached 320 μm. This agrees with the expected $d\tilde{\nu}/dm$ predicted in Equation 3-5 further validating the equation.

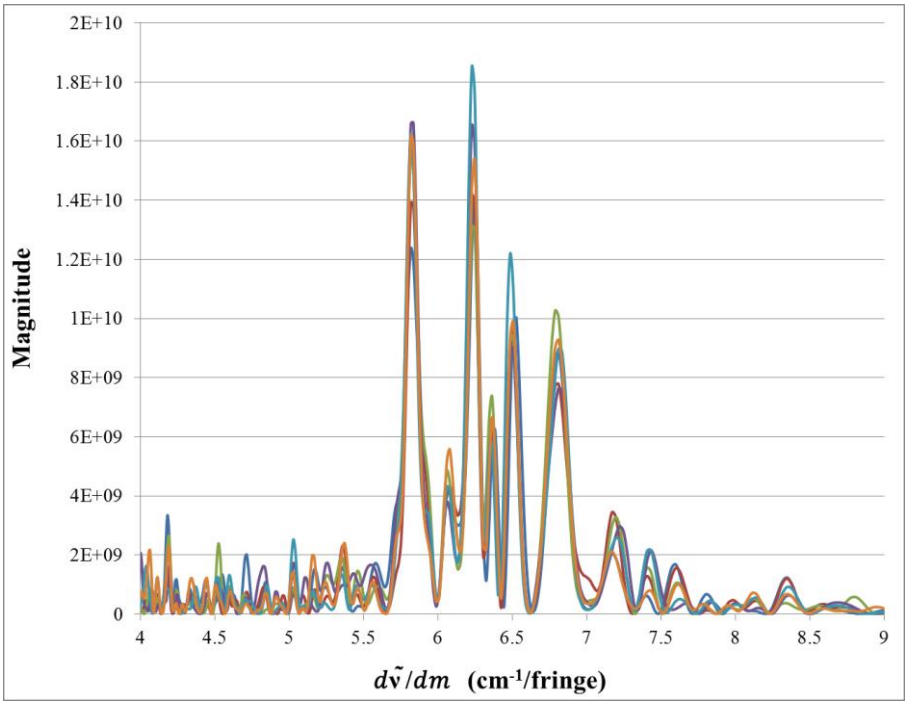

Figure 4-8 – FT output of samples using internally etched (~320μm diameter) capillary. Note the majority of fringe components are now in the range of approximately 5.5-7.0 cm^{-1}/fringe.

Sources of Noise

Instrumental Noise

With any analytical method employing instrumentation, some degree of error can be attributed to the instrumentation. (Skoog, Holler, & Nieman, 1998) In the LCORR device presented, a spectrometer is used for spectral measurements. This primarily consists of a series of mirrors, a grating to spatially diffract the different wavelengths, and an imaging CCD camera for measuring this resulting spectrum.

CCD detectors, along with other semiconductor-based sensors, are prone to "dark current" noise. Dark current is current produced randomly and not as a result of photon activity. (Understanding CCD Read Noise, 2012) As the level of dark current is a function of temperature, cooling the CCD chip significantly reduces its noise contribution. (Hamamatsu, 2012) The CCD is thermoelectrically cooled to -60º C for experiments in this work. Without this cooling, the increased noise was clearly observed. Depending on the cost and design of a spectrometer, the degree of detector cooling may be variable or absent, affecting the spectral quality of the data produced.

Beyond dark current, other sources of noise in CCD detectors include pixel non-uniformity, shot noise, read noise, and electronic interference. (Understanding CCD Read Noise, 2012) (Hamamatsu, 2012) For the most part, these additional sources of noise are a function of CCD design quality, and therefore cost.

Environmental Noise

In comparison to a potential portable field device, environmental noise is somewhat minimized in the proof-of-concept design being used, as it is secured on an optics bench and surrounded by light shielding. In a sensitive optical device, such as the LCORR, physical vibration in particular could produce significant problems in the quality of results. In the current form, two fiber tapers are placed in contact with the thinned capillary. Any movement of either one of these fibers would likely result in a changing of the resonance conditions, potentially leading to significant changes in output spectra. Any previously determined calibration would likely be void in this case, requiring an operator capable of recalibrating the device to the particular method parameters being used. As vibration with the fiber taper coupling method presents such a potential problem, the proof-of-concept device used in this work is installed on a vibration-resistant optics bench.

For potential field sensors, or in other applications where a more robust deign is necessary, the coupling method relying on fiber tapers is likely in need of an alternative. In Chapter 1, a small selection of possible ring resonator coupling methods was presented. Ring resonators can also be micro-fabricated, as discussed earlier. (Scholten, Fan, & Zellers, 2011) For a truly portable device, such a design with no moving parts and little or no tuning or positioning would be attractive, if not essential.

As discussed earlier, in Chapter 1, the sensitivity of a ring resonator is within the evanescent field, very near the reflecting surface. In circulating resonance modes, of both whispering gallery and waveguide nature, some fraction of the total internal reflection will need to be off of the outer wall surface. Therefore, even in the case of a liquid-core resonator, with the

analysis sample in the core, the outer surface will always be responsive, detecting any changes on the outer surface. This naturally leads to precautionary steps to avoid environmental contamination to the outer surface, most likely in the form of dust or other particulates. One could envision two approaches to solve this issue. In the first, encapsulation of the entire LCORR and tapers in a clear polymer or gel would protect the surfaces from environmental contamination. (Sumetsky, Windeler, Dulashko, & Fan, 2007) The problem that it would introduce is the out-coupling, or refraction, of light from both the ring resonator and the fiber tapers that was previously guided. This is rather unavoidable, as the lowest RI polymers have an index of refraction around 1.29, whereas air is nearly 1.00. The other approach would be to seal the ring resonator and the fiber tapers in a hollow cell, such that no contamination could enter, but the surfaces still benefit from the cladding of the surrounding air. Both of these solutions seal in place the components, fiber tapers and capillary in the case of an LCORR, without the ability to be adjusted. For this reason, both of these solutions are inappropriate in the current proof-of-concept device, as tuning and adjustments are needed for conducting research.

Fluidic 'Noise'

When analyzing small sample volumes in a relatively long capillary, it becomes necessary to have fluidic control that allows for smooth linear sample flow as well as stability when stopped. Typical fluidic pumps used for analytical instrumentation include peristaltic pumps and syringe pumps. Both types of pumps generally have elastic components. For a peristaltic pump, the tubing is flexible. For a syringe pump, the syringe septum and/or any air bubbles trapped inside the syringe provide an elastic component. In other terms, the pump "elasticity" is what prevents rigid

starting and stopping- something that is very helpful when analyzing very small samples. As an example, when a 1 μL sample is drawn into the capillary the linear distance occupied by the sample is approximately 20 mm (ignoring any diffusion, mixing, etc.). With either type of pump, the lag time due to elasticity is several seconds. This lag time is the delay when starting or stopping the pump, until full speed or full stop is achieved, respectively. At most flow rates, trying to stop a 20mm sample plug precisely at the LCORR with a lag time of several seconds proves challenging.

In the proof-of-concept device, a 3-way solenoid valve was installed to allow near-instantaneous fluidic stoppage for microliter and sub-microliter samples. This is pictured in Figures Figure 4-9 and Figure 4-10. To draw sample into the LCORR, the valve connects the pump, either peristaltic or syringe, to the sample intake and LCORR region. To instantaneously stop flow, and trap a sample in the LCORR region, the valve is switched to connect the pump to an open pressure relief tube (open to room air). This seals the capillary line leading to the LCORR and sample.

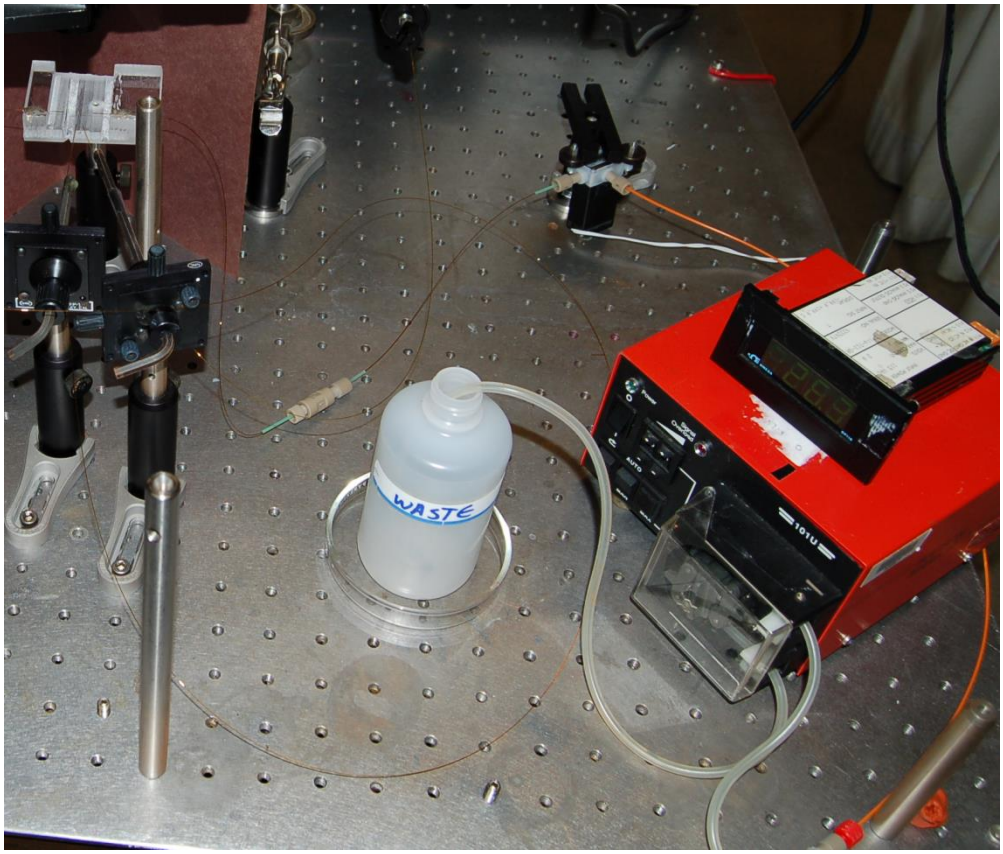

Figure 4-9 – Photo of LCORR fluidics system. On the right is a peristaltic pump (syringe pump also used in place). This draws sample and empties into a waste container. In the top of the screen, a solenoid valve remotely switches between the LCORR and open air (effectively sealing the LCORR sample in place).

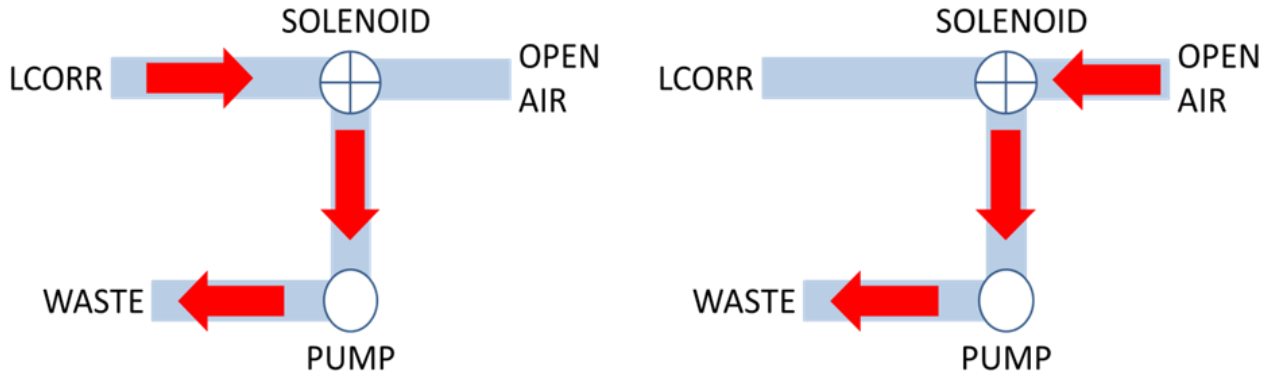

Figure 4-10 – Schematic of Figure 4-9. On the left, sample is drawn in from the LCORR. On the right, the solenoid is switched over to draw in room air, stopping flow in the LCORR and releasing any backpressure from the pump.

For a real-world device, the issue can likely be either avoided or changed by scaling the system down into a micro-fabricated structure. (Scholten, Fan, & Zellers, 2011) If continuing with the capillary form, future design improvements would also include smaller dimensions where possible and minimizing the amount of "dead" volume (i.e., excess sample line) before and after the LCORR region.

Temperature Noise

Temperature fluctuations are another source of noise in the device. According to previous researchers, the RI of fused silica increases approximately $9 \times 10^{-6}\ K^{-1}$ and water decreases $9 \times 10^{-5}\ K^{-1}$ in the visible region being studied. (Abbate, Bernini, Ragozzino, & Somma, 1978) (Leviton & Frey, 2006). Therefore, with RI shifting in opposite directions for a given temperature change, there is a reduction in the overall n_{eff} change as a function of temperature, dn_{eff}/dT, when compared with pure fused silica. Due to this relationship, Suter et al. found, using a smaller but similar fused silica LCORR, an overall dn_{eff}/dT of $6.4 \times 10^{-6}\ K^{-1}$ (Suter J. , White, Zhu, & Fan, 2007).

In a broadband ring resonator, as described in Chapter 3, a variety of complex optical phenomena contribute to the sensitivity of the device. These are greatly affected by a change in RI drop, n_2/n_1, at the wall/core interface.

To estimate the contribution made by temperature fluctuations on the noise of RI measurements, two additional experiments were performed. First, the fringe spacing sensitivity to temperature, $(d\tilde{\nu}/dm)/dT$, was determined. A T-junction was installed on the capillary, just downstream of the LCORR region. A micro-thermocouple was installed in the side port of this T. Illustrated in Figure 4-11, a sample of deionized water was slowly heated on a hot plate while

interference spectra were collected. Due to the thermal losses associated with such small volumes and relatively low flow rates, over the course of 30 minutes the temperature range at the thermocouple, near the LCORR, increased only 0.8 K despite original sample temperatures increasing significantly more. From the interference spectra, Fourier transform analysis was performed in the same way as described in Chapter 3. A representative FT peak was tracked over the temperature range, and the relationship is plotted in Figure 4-12. Suter, et al. found n_{eff} to have a positive relationship with temperature, and Equation 3-5, showed an inverse relationship between n_{eff} and fringe spacing. (Suter J. , White, Zhu, & Fan, 2007)

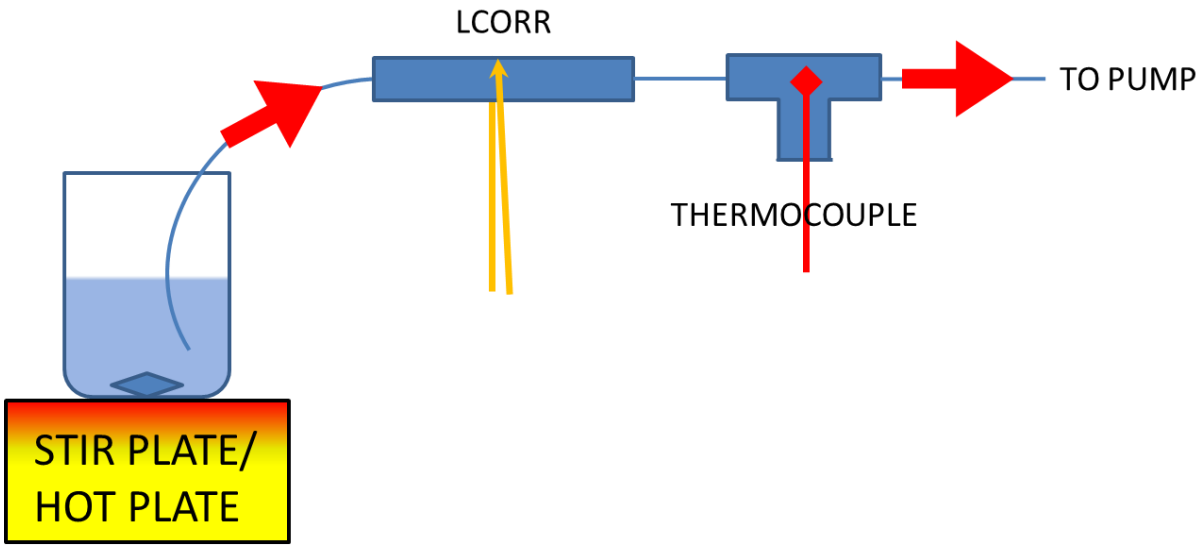

Figure 4-11 – Schematic of setup for temperature-based experiments in LCORR.

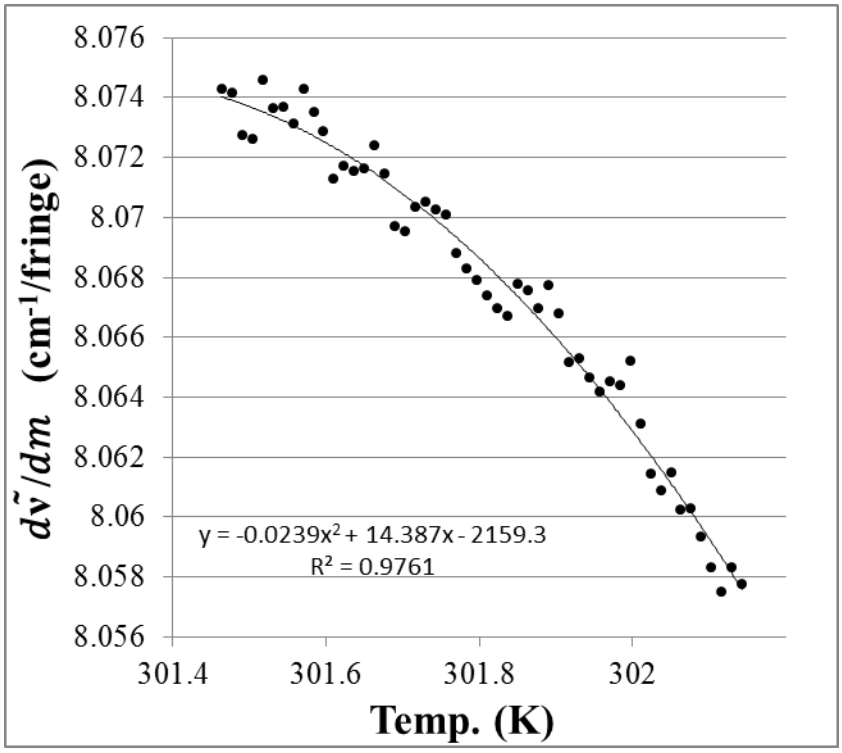

Figure 4-12 – FT fringe spacing (peak position on FT plot) as a function of temperature, as measured by thermocouple in fluidic T fitting just past LCORR region.

The shape of the plot in Figure 4-12 is rather complex for a number of possible reasons. Abbate, et al. showed anomalies in the relationship between temperature and the refractive index of water. (Abbate, Bernini, Ragozzino, & Somma, 1978) In a broadband resonator, each of the many propagation modes will have a unique distribution of field intensity in the wall relative to the core. As the relationship between temperature and refractive index has opposite signs for silica and water, the relationship between n_{eff} and temperature is furthermore complicated and unintuitive. Nonetheless, a quadratic fit showed the closest approximation.

A second experiment was performed to determine the temperature fluctuation of a room temperate sample solution. Note that, with the exception of the previous experiment involving heating, no temperature control or insulation was used for samples. In this same manner, a sample

of deionized water was left at room temperature and the thermocouple output was recorded for 30 minutes. From this, the standard deviation of temperature was found to be 3.3 x 10^{-3} K. For these experiments, this will be taken to represent the 'noise.' From the relationship between fringe spacing and temperature, shown in Figure 4-12 above, this temperature fluctuation noise was calculated to be 8.0 x 10^{-5} cm^{-1}/fringe, according to Equation 4-2. The overall noise of the fringe spacing in the LCORR was found, in Chapter 3, to be 3.86 x 10^{-4} cm^{-1}/fringe. Of this total, the noise contribution from temperature fluctuations therefore constitutes approximately 20%. This estimate is expected to be somewhat high, as the native thermocouple noise was neglected and all fluctuation was assumed to be directly caused by real temperature fluctuation.

Equation 4-2

$$Temp\ Noise\left(\frac{cm^{-1}}{fringe}\right) = Temp\ Noise\ (K)\left[Temp\ Sensitivity\ \left(\left(\frac{cm^{-1}}{fringe}\right)/K\right)\right]$$

Extrinsic improvements could be made to reduce temperature fluctuation in the device. Future designs could include various means of insulation. Described earlier, fully enclosing the device would prevent unwanted particulates and other contamination. Doing so would also provide some degree of temperature insulation through minimized convection. One concern, however, might be the possibility for a slow upward drift in temperature as a result of the introduced optical radiation without a means for convective losses. The ultimate solution for all of this would, perhaps, be a sealed device that includes extremely precise temperature control. This could be done thermoelectrically, with small Peltier elements, however the end result is a device gaining further complexity and cost.

Resolution

As the described analytical methods in this chapter, and previous ones, are based on the extraction of interference spectra, clearly the instrument resolution has an influence on the detection capabilities. The resolution of the system with the 2400 g/mm grating was determined using the 578 nm doublet from a mercury lamp source, shown in Figure 4-13. Resolution was calculated to be approximately 1.5 x 10^4, using Equation 4-3. This implies that a clean fringe pattern would be maximized with a resonator quality factor (Q) of 1.5 x 10^4. Although a resonator of higher quality could be used, the added value may not be fully realized without the use of a higher resolution instrument.

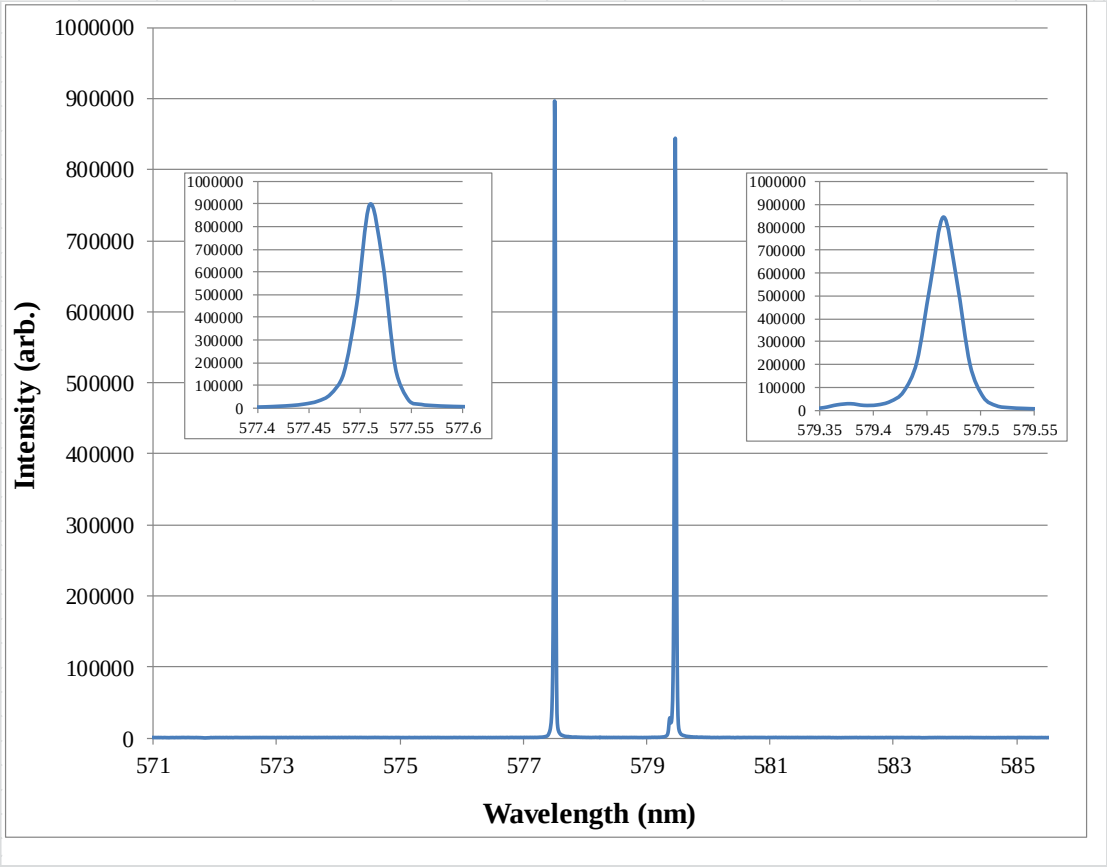

Figure 4-13 – Mercury arc lamp 578nm doublet using 2400g/mm grating. Insets are the individual peaks.

Equation 4-3

$$R = \frac{\lambda}{\Delta\lambda}$$

In the actual broadband LCORR device, multiple wavelengths and propagating modes are employed, and thus a wide variety of Q-factors would be present. As the interference patterns are produced from a complex relationship of overlapping propagation modes, perhaps a more appropriate means of quantifying relative resonance quality would be to compare the relative intensity of FT power peaks. This type of analysis would still be prone to error from the complexity of these relationships, and it would not serve as an appropriate means of comparison with single-mode ring resonators. Nonetheless, if an "estimated Q-factor" were approximated from the peak widths in a typical interference spectrum, using Equation 4-4, this value would be 5.5 x 10^3. (Vollmer & Arnold, 2008) If a direct comparison was requested, this is considerably less than the majority of published Q-factors in single mode ring resonator applications. (Fan X. , White, Zhu, Suter, & Oveys, 2007)

Equation 4-4

$$Q = \frac{frequency(hz)}{FWHM(hz)} = \frac{wavelength(nm)}{FWHM(nm)}$$

Useful analysis with low resolution spectrometers

Using a UV/Vis spectrometer of significantly lower resolution than used in the previous experiments in this chapter, as well as Chapter 3, would produce spectra lacking the clear interference fringes. It would still, however, be possible to produce useful data from the resulting spectra. Several relationships are simultaneously dependent on the optical parameters, including refractive index, of the resonator. This was discussed in greater detail in Chapter 3. Briefly, these relationships form a complex spectral output comprised of varying degrees of interference. Collecting this output with a low resolution spectrometer would produce complex and unintuitive spectra. Nonetheless, as they result from complex behavior of resonance modes, which themselves are strongly a function of RI, these spectra would be rich with information.

A lower resolution grating, 150 g/mm, was installed in the ARC 2300i (Princeton Instruments) spectrometer. Spectra were collected for mixtures of IPA in water, with RI ranging from 1.3415 to 1.3506. These spectra are displayed in Figure 4-14. In this figure, the spectral output is observed to be strongly influenced by RI, albeit with much complexity and multiple relationships present.

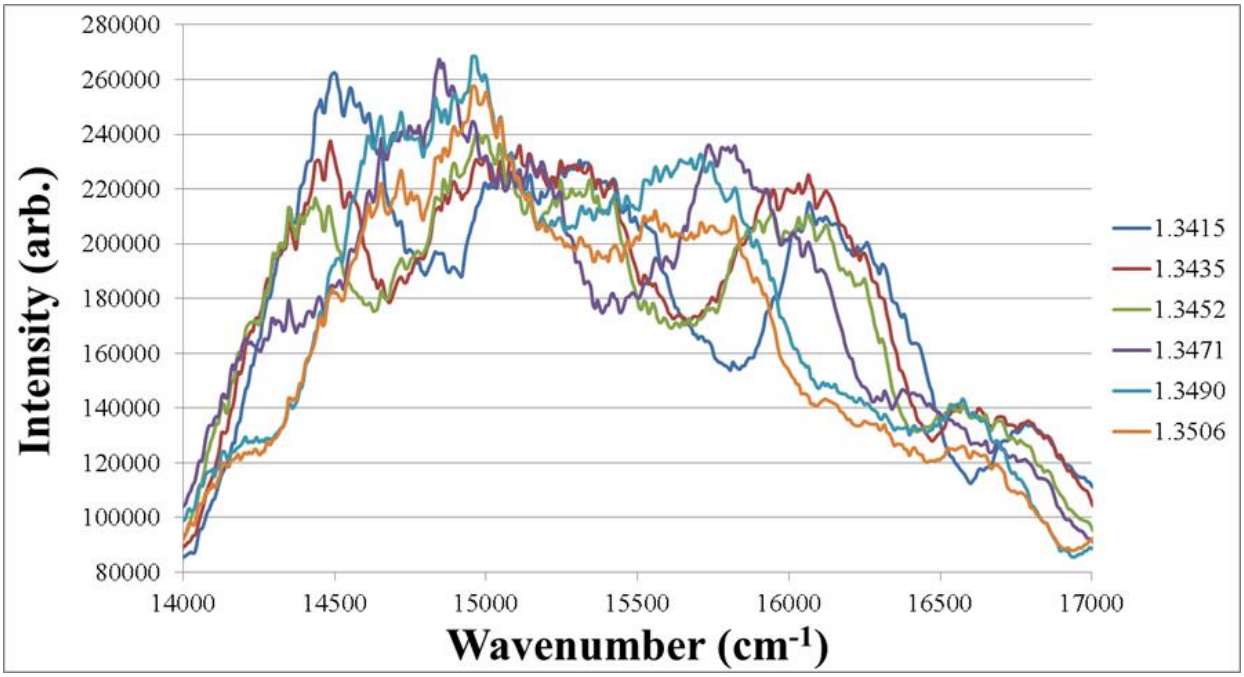

Figure 4-14 – Output spectra for six solutions of varying RI, taken with lower resolution 150g/mm grating installed. Notice the much wider spectral range in comparison with previous spectra. © 2012 American Chemical Society

For a closer look at the response to RI, a mixing flask was used, in the same way as described in Chapter 3, to produce a slowly changing mixture of IPA and water. Forty spectra were collected for IPA/water mixtures over an RI range of 1.3605-1.3680. These spectra are displayed in Figure 4-15. Over the full 0.0075 RIU range covered by these spectra, most of the spectral shifting lacked any simple linear relationship. Although one could attempt a peak tracking method based on one of these peak locations, the source of any single peak is complex, and therefore such method would likely prove futile. For this reason, chemometric approaches to data analysis were investigated.

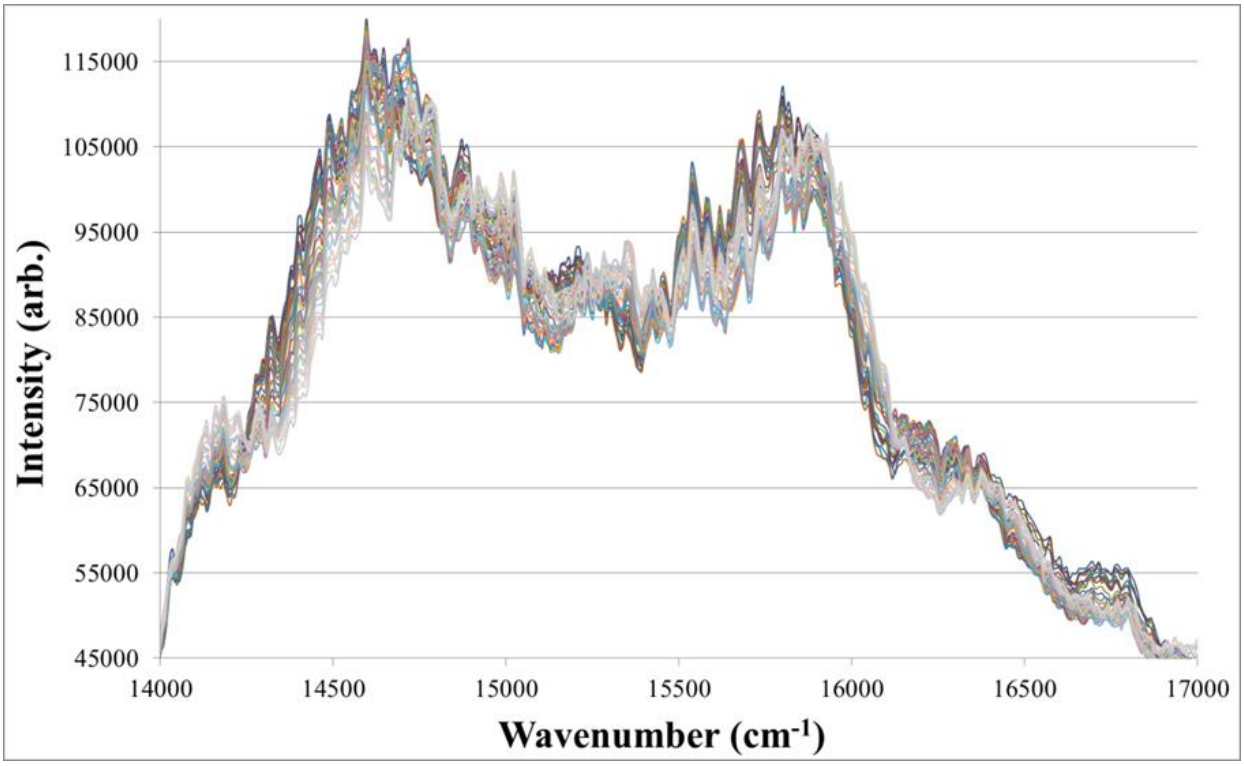

Figure 4-15 – A set of 40 spectra collected over a range of RI from 1.3605-1.3680 with the 150g/mm grating.

A partial least squares (PLS) model was produced from the set of 40 IPA/water spectra. The goal of a PLS model is a linear relationship between the actual and predicted values, in this case sample RI, based on the mathematical fitting ability of a computer program. Ideally, a high predictability is achieved with the smallest possible number of principal (fitting) components. With fewer components used, a model is more adaptable to other types of unforeseen variations in sample properties. (Dahlberg, Lee, Wenger, & Vargo, 1997) (Pereira, et al., 2008)

The root mean squared prediction error (RMSE) of the PLS model is displayed in Figure 4-16 as a function of the number of fitting components used. In Figure 4-17, the resulting r^2 correlation of the linear relationship between actual and fitted RI is displayed as a function of the number of fitting components. While the RMSE is actually minimized with four components, there is only a very slight improvement in both RMSE and r^2 beyond the third component in these

plots. With three components, the RMSE error is 7.2 x 10^{-8} RIU, and the resulting PLS plot of predicted vs. actual RI is shown in Figure 4-18. In some applications, RMSE is used to estimate a detection limit (DL). (Corley, 2003) If estimated DL were accepted as 3 X RMSE, the reported DL from this PLS model would be 2.2 x 10^{-7} RIU. As this model was based exclusively on spectra produced from clean IPA and water mixtures, it must be emphasized that real world samples containing multiple analytes would be likely prone to higher prediction error. This would be a result of the additional complexity of the spectra in the presence of multiple analytes and perhaps multiple optical mechanisms altering the spectra (e.g., absorption). The higher RMSE prediction error would lead to higher detection limits.

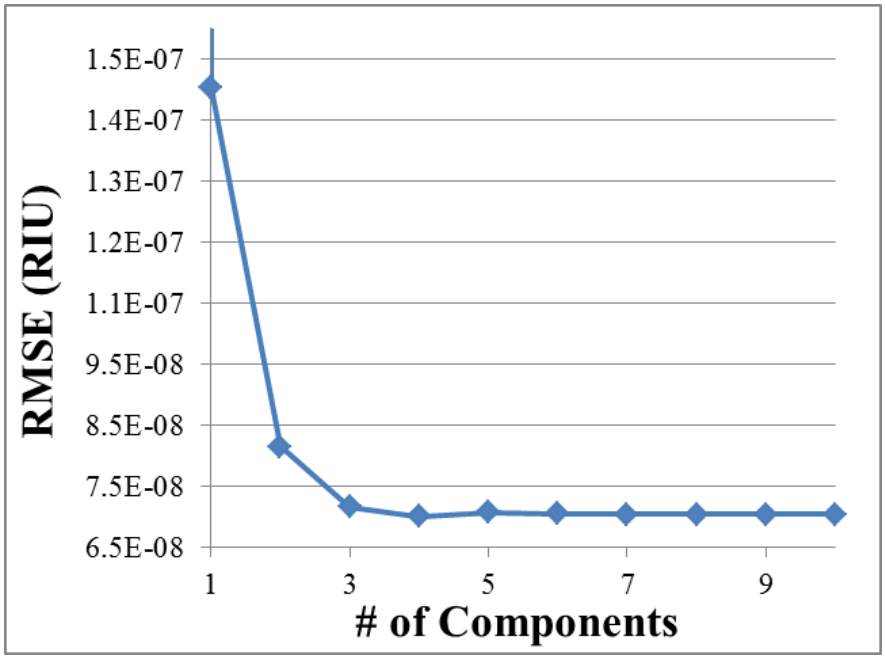

Figure 4-16 – Root mean squared prediction error as a function of the number of fitting components used in a PLS model of the 40 spectra in Figure 4-15.

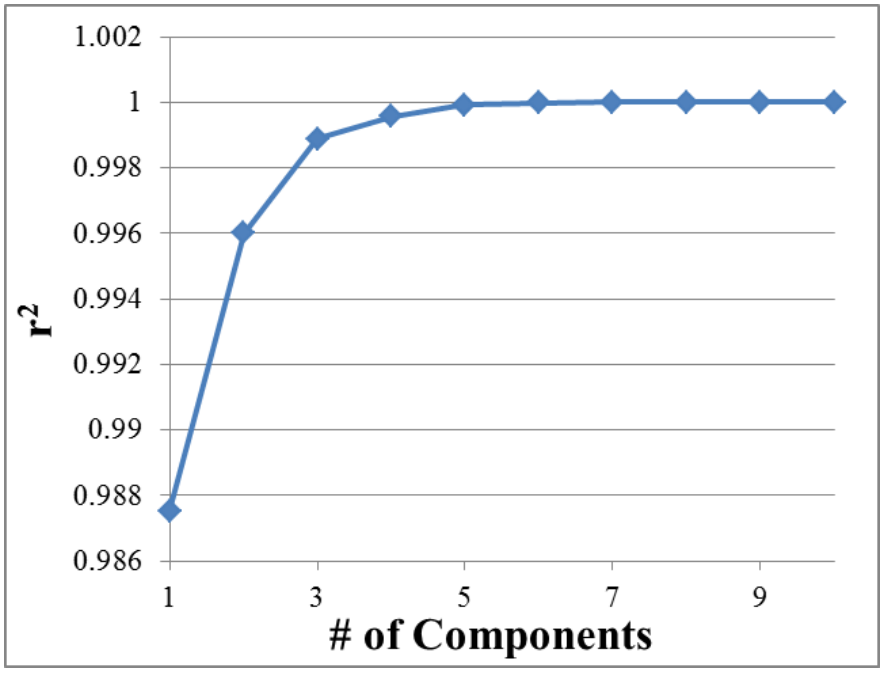

Figure 4-17 – Linear correlation (between predicted and actual RI) as a function of the number of fitting components in a PLS model of the 40 spectra in Figure 4-15.

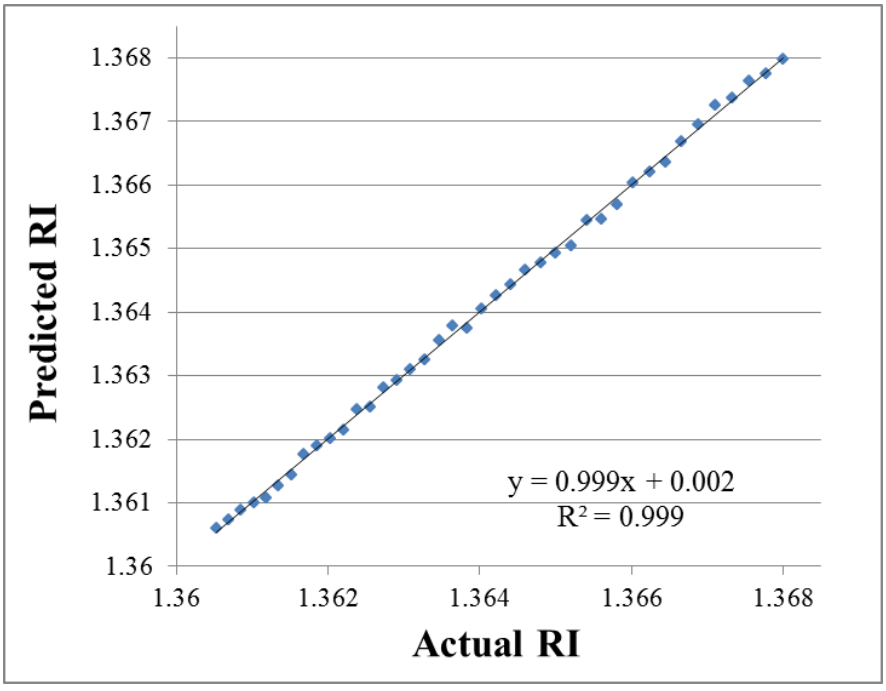

Figure 4-18 – PLS model of predicted vs. actual RI, of the 40 spectra in Figure 4-15, using three fitting components. © 2012 American Chemical Society

Dynamic Range

While the results for absorption and refractive index, in Chapters 2 and 3 respectively, are impressive, the samples being analyzed were of only relatively limited dynamic range. Understanding the dynamic range of measurement is an important part of characterizing a new type of detection system. (Skoog, Holler, & Nieman, 1998)

Absorption

For non-surface active analytes, it was discussed in Chapter 2 how apparent path length, L_{app}, can be assumed to be equal to effective path length, L_{eff}. (Tsunoda, Itabashi, & Akaiwa, 1992) (Tsunoda, Umemura, Ueno, Okuno, & Akaiwa, 2003) This was found to be on the order of 1 mm or less. As a result, rather concentrated chromophores can potentially be analyzed in the device. Shown in Figure 4-19 are the absorbance spectra of BTB solutions at 10^{-3} and 10^{-2} M. The absorbance spectra for the same solutions in the 4 mm cuvette cell, described in Chapter 2, are also displayed in the same figure. The spectra from the cuvette are of poor quality at such high concentrations, and the two concentrations are virtually indistinguishable at the previously established λ_{max} around 610 nm. The absorbance spectra for the LCORR, on the other hand, are of data quality reasonable for distinguishing between the two concentrations.

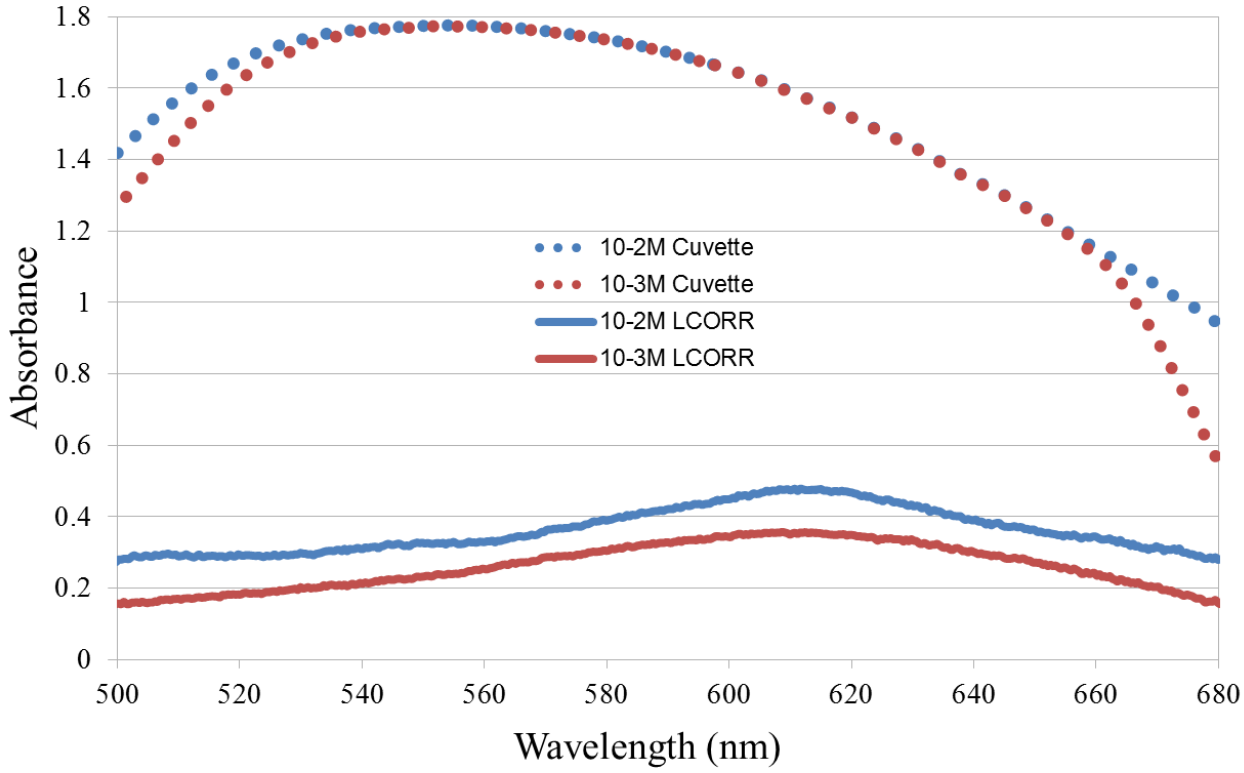

Figure 4-19 – High concentration of BTB in both the LCORR and the 4mm cuvette.

The dynamic range for absorption detection is relatively large, depending on the analyte. Shown in Chapter 2, very low concentrations of surface-active dye were detected down to 10^{-7} M. The distinction comes in the fact that L_{app} can vastly exceed L_{eff} for surface active analytes, whereas other analytes can utilize a very short L_{app}, equal to L_{eff} in these cases, allowing highly concentrated solutions to be analyzed.

Refractive Index

The refractive index analysis in Chapter 3 is limited to the practical range of RI values that would be expected for samples of aqueous and possibly biological in nature. Below the RI of

water, approximately 1.33, very few aqueous applications exist, as added analytes will almost always increase the RI.

Light will generally be guided to some degree for sample RI in the range of n_{out} to n_{wall}. (Gibb, 1942) (Daly, 1984) In other words, a minimum critical angle permitting total internal reflection (and evanescent penetration) will exist whenever the core RI is less than that of the resonator material. If the external wall surface were met with a greater RI than in the sample core, some propagating modes would be "stripped," or lost to refraction. With a liquid-core capillary surrounded by air, this is not a concern.

To follow the resonance behavior at higher RI, and particularly across the boundary where $n_{core}=n_{wall}$, 240 spectra were collected for mixtures of butanol and tolune ranging in RI from 1.430 to 1.465. The mixing of the sample was performed according to the methods described, in greater detail, in Chapter 3. The FTs of these spectra were calculated in the same manner as also described in Chapter 3. (Oates & Burgess, 2012) (Brigham, 1974) To produce a simplified plot representing the relative resonance intensity, the maximum 'Magnitude' was determined for each spectrum. This maximum was plotted against core RI in Figure 4-20. The maximum varies considerably due to the dynamic nature of the resonance spectra and the relatively rapid change in RI- this is an RI range approximately 15 times greater than the one studied in Chapter 3. The significance of this plot is the distinct 'flat-lining' of FT peaks beyond a core RI of 1.457, the point where $n_{core}=n_{wall}$. This could be possibly due to the fact that a dramatically greater multiplicity of modes complicated the interference output to the point where resolution of the individual frequency components via FT was diminished. Another possible contributing factor is that, because the capillary used in this experiment was externally etched, WGMs were not readily supported. Therefore as expected, the useful dynamic range of RI detection reaches its maximum where $n_{core}=n_{wall}$.

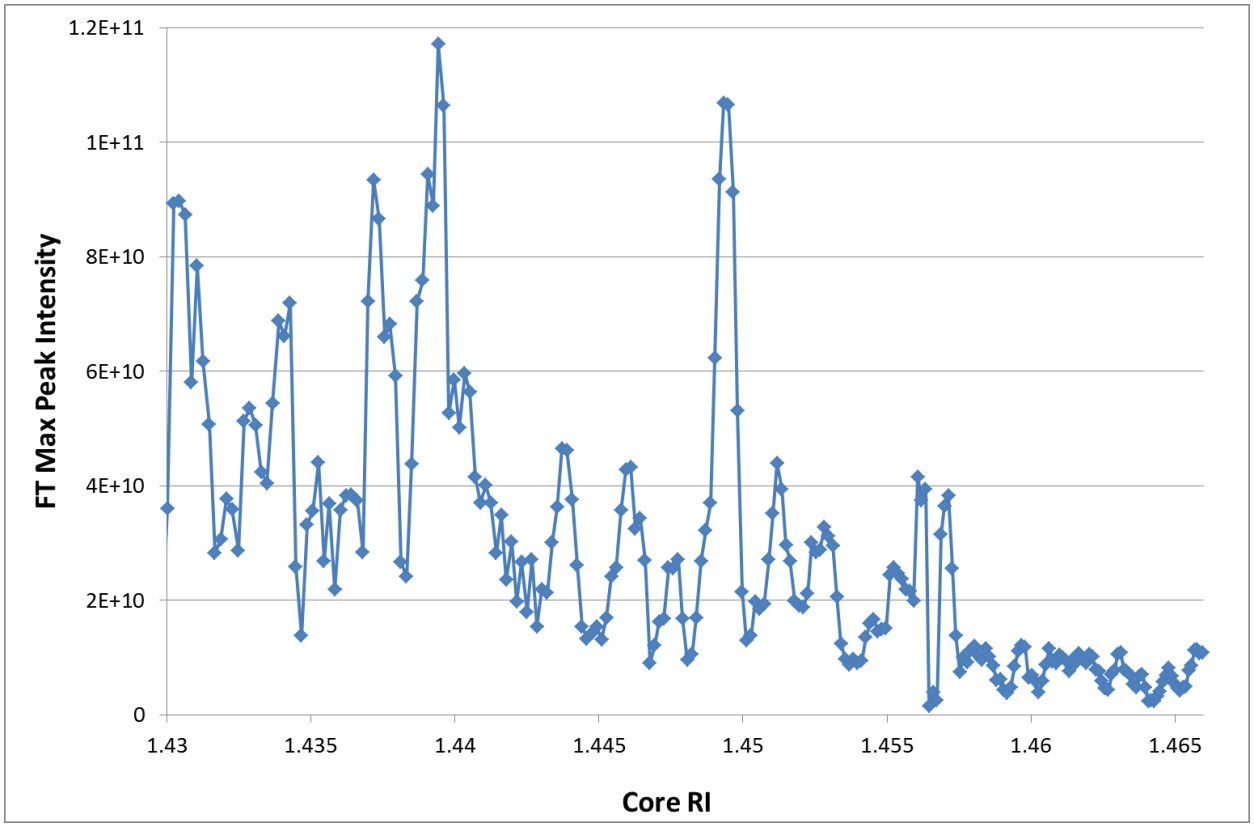

Figure 4-20 – Maximum FT peak intensity as a function of sample RI in core. Note the flattening of the plot around RI of 1.457.

Conclusion

In the development of a potential sensing device, thorough characterization and extensive critical analysis must be performed. In this chapter, the broadband ring resonator device was investigated on several fronts. A reduced wall thickness was confirmed to allow greater sensitivity. Internal etching methods were found to be more convenient and controllable than external etching methods, however they have the tendency to promote whispering gallery modes rather than waveguide modes. The validity of FT-based analysis methods introduced in Chapter 3 was further confirmed through the widely different capillary diameters for internally versus

externally etched capillaries. Noise contribution and minimization from various sources (instrumental, environmental, fluidic, and temperature) was investigated, and an estimated contribution for temperature-induced noise was quantified. The potential for multivariate analysis of low-resolution spectra was also investigated and confirmed. Finally, the dynamic range for both absorption and refractive index detection was characterized.

References

Standard Dimension Ratio - SDR. (2012, 11 05). Retrieved from The Engineering Toolbox: http://www.engineeringtoolbox.com/sdr-standard-dimension-ratio-d_318.html

Understanding CCD Read Noise. (2012). Retrieved from Quantum Scientific Imaging: http://www.qsimaging.com/ccd_noise.html

Abbate, G., Bernini, U., Ragozzino, E., & Somma, F. (1978). *J. Phys. D: Appl. Phys*, *46*, 1167-1172.

Brigham, E. (1974). *Fast Fourier Transform.* Englewood Cliffs: Prentice-Hall.

Corley, J. (2003). In P. Lee, & H. Aizawa, *Handbook of Residue Analytical Methods for Agrochemicals* (pp. 59-75). West Sussex: Wiley.

Dahlberg, D., Lee, S., Wenger, S., & Vargo, J. (1997). *Appl. Spectrosc., 51*, 1118-1124.

Daly, J. (1984). *Fiber Optics.* Boca Raton: CRC Press, Inc.

Deyl, Z., & Svec, F. (2001). *Capillary Electrochromatography.* Amsterdam: Elsevier Science B.V.

Fan, X. (2009). *Advanced Photonic Structure for Biological and Chemical Detection.* Dordrecht: Springer.

Fan, X., White, I. S., Zhu, H., Suter, J., & Sun, Y. (2008). *Anal. Chim. Acta., 620*, 8-26.

Fan, X., White, I., Zhu, H., Suter, J., & Oveys, H. (2007). *Proc. SPIE,* 6452-18.

Gibb, T. (1942). *Optical Methods of Chemical Analysis.* New York: McGraw-Hill Book Company, Inc.

Hamamatsu. (2012). *CCD Noise Sources and Signal-to-Noise Ratio.* Retrieved from Concepts in Digital Imaging Technology: http://learn.hamamatsu.com/articles/ccdsnr.html

Harrick, J. (1979). *Internal Reflection Spectroscopy.* Ossining: Harrick Scientific Corporation.

Leviton, D., & Frey, B. (2006). *Proc. SPIE, 2*, 6273-6299.

Oates, T., & Burgess, L. (2011). *Appl. Spectrosc., 65*, 1187-1192.

Oates, T., & Burgess, L. (2012). *Anal. Chem., 84*, 7713-7720.

Pereira, A., Pontes, M., Neto, F., Santos, S., Araujo, M., & Galvao, R. (2008). *Food Res. Int., 41*, 341-348.

Safety, U. o. (2009). *Hydrofluoric Acid*. Retrieved from Technical Information & Practical Solutions: http://www.ehs.washington.edu/manuals/tips/hydrofluoricacid.pdf

Scholten, K., Fan, X., & Zellers, E. (2011). *Appl. Phys. Lett., 99*, 141108.

Skoog, D., Holler, F., & Nieman, T. (1998). *Principles of Instrumental Analysis.* United States: Thomson Learning.

Sumetsky, M., Windeler, R., Dulashko, Y., & Fan, X. (2007). *Opt. Express, 15*, 14376-14381.

Suter, J., & Fan, X. (2010). In A. Hawkins, & H. Schmidt, *Handbook of Optofluidics* (pp. 11(1-29)). Boca Raton: Taylor & Francis.

Suter, J., White, I., Zhu, H., & Fan, X. (2007). *Appl. Opt., 46*, 389-396.

Suter, J., White, I., Zhu, H., & Fan, X. S. (2008). *Biosens. Bioelectron., 23*, 1003-1009.

Tsunoda, K., Itabashi, H., & Akaiwa, H. (1992). *Bull. Chem. Soc. Jpn., 65*, 1581.

Tsunoda, K., Umemura, T., Ueno, H., Okuno, E., & Akaiwa, H. (2003). *Appl. Spectrosc., 57*, 1273.

Vollmer, F., & Arnold, S. (2008). *Nat. Methods, 5*, 591-596.

White, I., Oveys, H., & Fan, X. (2006). *Opt. Lett., 31*, 1319-1321.

CHAPTER 5

Potential Absorption Detection Applications

Intro

In order to accurately forecast the potential applications for a new analytical technology, one must answer the following questions: "What are its advantages and limitations, and how do these justify replacement of a current technology?" This chapter will answer these questions and outline some supporting experiments.

With specific regard to the methods likely to be used for absorption detection, one large advantage of using a broadband ring resonator is the potentially low-cost design. If a suitable micro-fabricated design could be used, the ring resonators and fluidics could be mass-produced on a large scale, significantly lowering the unit cost. (Vdovin, Sarro, & Middelhoek., 1999) It must be emphasized that, for the purposes of absorption detection, a traditional (i.e. utilizing a grating or prism) spectrometer is not necessarily required. This is clearly the most costly component of the current system. If a limited number of possible analytes and absorption peaks were expected, such as in a controlled assay, the output at perhaps only one or two wavelengths would be necessary. In this case, LED(s) could be used as the source, and a simple photodiode as the detector. (Yokota, Okada, & Yamaguchi, 2007)

The current proof-of-concept device is by no means portable. The potential for a low-cost design, as described above, could be envisioned with micro-fabricated components. If pursuing a micro-fabricated design, portability is a natural benefit. A device that is both low-cost and portable has an attractiveness to that is lacking in most bench-top laboratory instrumentation.

In Chapter 2, the sensitivity of the broadband LCORR was found to be greatly enhanced for surface-attracted analytes. While the benefits of having high sensitivity and low detection limits might seem obvious, often overlooked is the ability to exhibit low sensitivity and analyze

highly concentrated samples. (Chai, Li, & Zhu, 2002) (Chai, Hou, & Verrill, 2005) With conventional UV/Vis absorption analysis, a dynamic range of 1-2 orders of magnitude is often the case. (Skoog, Holler, & Nieman, 1998) In Chapters 2 and 3, a dynamic range of 5 orders of magnitude is demonstrated for bromothymol blue detection, for example. The value in having a wide dynamic range is in reducing the potentially time-consuming and labor-intensive act of diluting sample to the proper concentration range. The additional value in being able to analyze highly concentrated samples is the potential to analyze unadulterated raw samples, such as those in industrial process settings or in medical settings (e.g, blood). (Burdick, 2002) (Blum & John, 2011) (Howard, et al., 2009) (Billot, Couty, & Hosek, 2010) (Doyle & Tran, 1999) (Steiner & Renschen, 1992) (Simhi, Gotshal, Bunimovich, Sela, & Katzir, 1996) (Zourob & Lakhtakia, 2010)

In the current proof of concept device, a 250 μm ID capillary is used as the flow channel and ring resonator support. The sample volume in this capillary is approximately 50 nL per mm axial length, as calculated using Equations 5-1 and 5-2. The region of detection is estimated to be less than 1mm, axially, based on the width and positioning of the input and output fibers. For comparison, a standard cuvette for UV/Vis analysis requires 2-4 mL of sample- over three orders of magnitude more than the LCORR being currently used. (Thomas, 1996) It must be emphasized that the current device is very much a proof-of-concept. Future designs, if it were desired, could minimize the sample volume much further.

Equation 5-1 $$A = \pi r^2$$

Equation 5-2 $$V = AL$$

Low Cost Analysis

The low-cost potential for broadband ring resonators can be approached from several angles. O'Toole and Diamond outline the simplicity of detectors that simply employ a monochromatic LED and photodiodes. (O'Toole & Diamond, 2008) In doing so, complete spectral information is neglected. In many controlled sample environments, only a limited number of analytes and spectral features (e.g. absorption bands) are possible. In these situations, precise spectral information might not be critical, and the current instrumentation being used could be unnecessarily complex and expensive. In recent years, LEDs have become available at many wavelengths across the entire visible spectrum. (Technical LED Color Chart, 2012) According to Haitz's law, the cost per lumen of light output falls by a factor of 10 per decade, and the amount of light generated by LED package increases by a factor of 20 for the same time period. (Graydon, 2007) (Steele, 2007) This is illustrated in Figure 5-1.

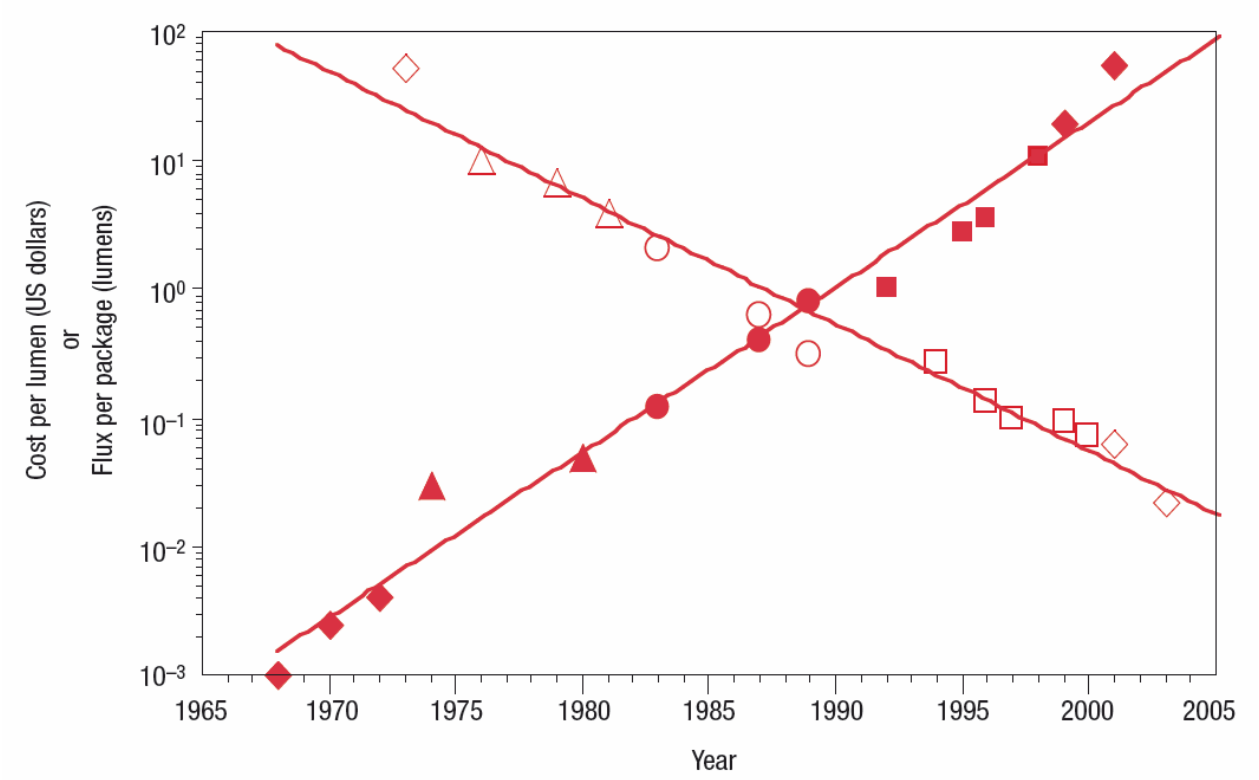

Figure 5-1 – Cost per lumen and flux (output) per LED package vs. year. Open symbols denote cost per lumen (in US Dollars) and closed symbols denote flux per package (measured in lumens). (Reprinted by permission from Macmillan Publishers Ltd: Nature Photonics (Steele), copyright 2007)

In some applications, the absorption being detected is generically the loss of overall signal transmission. (Ferreira, Werneck, & Ribeiro, 2001) (Leung, Shankar, & Mutharasan, 2007) In other words, no spectral information is collected other than the total source output. As expected, this type of analysis can only be effective where a very either one or a limited number of analytes are present that will produce a signal. For example, this will be the case when the reflecting surface is functionalized with a specific binding chemistry. The surface will then vastly favor the analyte of interest binding to the surface over all else that may be in the sample solution.

Harrick described two basic types of optical attenuation in total internal reflection: "Attenuated Total Reflection", or ATR, and "Frustrated Total Reflection", or FTR. (Harrick, 1979)

In the former, ATR, signal loss is a result of absorbing species on the reflection surface. As this is the mechanism responsible for the detection of methylene blue and all other analytes in Chapter 2, is it clear that spectral information can be resolved, if desired. FTR, on the other hand, is a result of partial transmission, away from the reflecting surface, reducing the total amount of light internally reflected. One source of this transmission is the presence of an analyte that locally alters the refractive index. Although this type of mechanism invites a very simple means of detecting a refractive index shift in a low cost ring resonator, it is limited by the detectability of an intensity shift. Additionally, nonspecific (broadband or monochromatic) intensity is vulnerable to a vast array of noise sources, ranging from anything contacting the surface, causing ATR/FTR, to any external influences such as source or detector fluctuation.

(FTR) Broad Attenuation BSA

As a proof of concept, bovine serum albumin (BSA) solutions were analyzed in the LCORR, measuring spectrally non-specific attenuation. BSA has been shown to adsorb to glass surfaces, particularly in mildly acidic aqueous solution. (Bull, 1956) (Yeung, Lu, & Cheung, 2009)

Unless otherwise specified, all configuration parameters (e.g., taper positions) remained the same as in Chapter 2 for this experiment. BSA solutions were produced in pH 4.5 buffer solutions of monobasic sodium phosphate (MSP). An initial stock solution of 3 mg/mL was created from solid powdered form (Sigma Aldrich). Serial dilutions of this were produced, down to 0.012 mg/mL. During analysis, BSA solutions were drawn into the capillary and then held in place for 30s to allow for surface binding with a fixed amount of time. The solutions were analyzed lowest to highest concentration, and a variety of solvents and alkaline solutions were found to clean and restore the surface to baseline conditions.

Results

As BSA is colorless, lacking a visible absorption band, the transmission loss associated with BSA binding is a result of frustrated total internal reflection, as described above, as the BSA protein has a greater RI than the water molecules it displaces when it adsorbs to the wall surface. (Leung, Shankar, & Mutharasan, 2007) In Figure 5-2, percent transmission of light from 510 nm to 590 nm is shown as a function of BSA concentration. This plot has a non-linear shape due to the availability of potential surface sites for adsorption. (Duff, Ross, & Vaughan, 1988) In other words, at low concentrations, the relative availability of free surface sites is high and BSA molecules have greater ability to adsorb. As concentrations increase, the surface sites are taken by BSA molecules, leaving fewer available for additional molecules to adsorb. This results in a diminishing added response with incrementally greater concentrations. The results from this experiment are modest; however, they verify the concept of using a simplified, low-cost ring resonator for RI measurements.

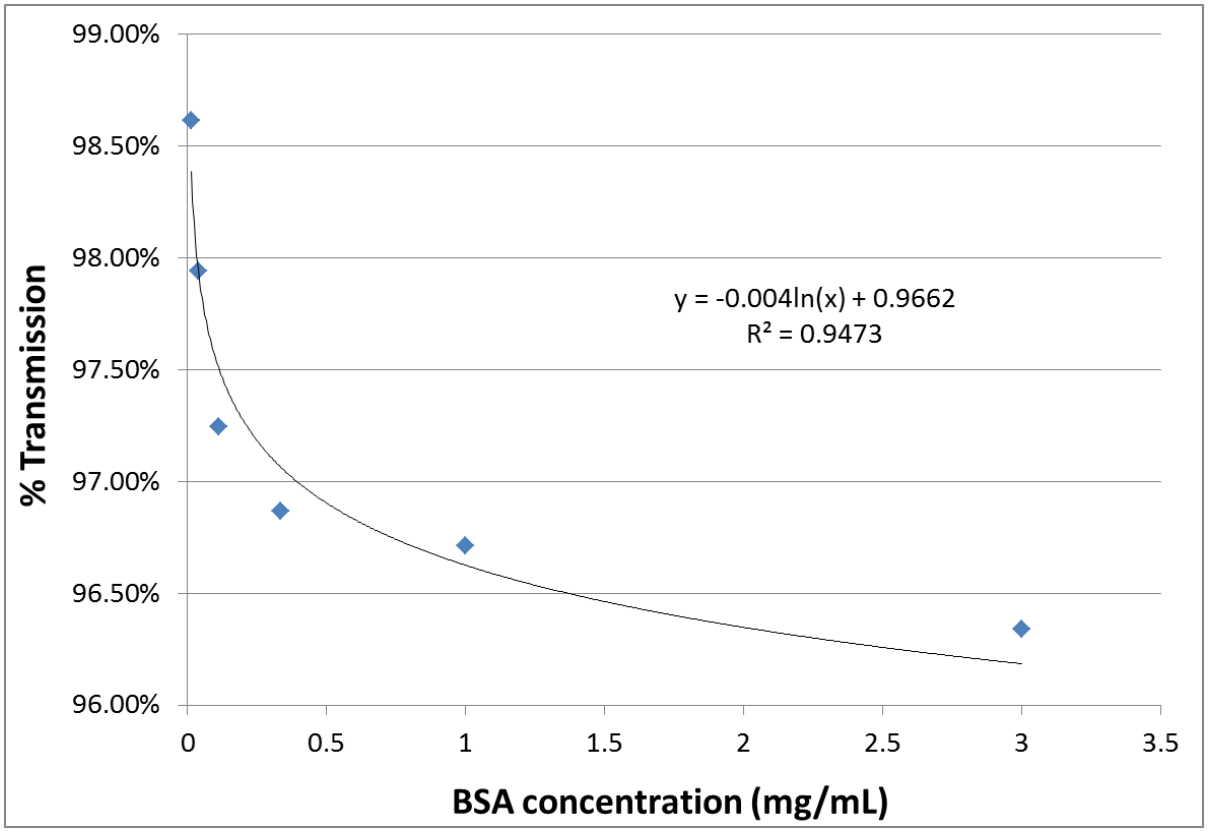

Figure 5-2 - %Transmission of 510nm to 590nm light as a function of BSA sample concentration.

Absorption without a Spectrometer

While the mechanism of attenuated total internal reflection (ATR) in a ring resonator has already been demonstrated with the absorption spectra produced in Chapter 2, a basic proof-of-concept experiment was performed to demonstrate the type of data that would be produced in a simple, low-cost, monochromatic ring resonator device. Methylene blue was analyzed with a monochromatic amber LED light source and a photomultiplier tube (PMT) as the detector.

Unless otherwise specified, all configuration parameters (e.g., taper positions) remained the same as in Chapter 2 for this experiment. An initial stock solution of methylene blue was prepared to 10^{-3} M from powdered form (Sigma-Aldrich) in deionized water. All subsequent concentrations were prepared from serial dilutions of this stock. Samples were analyzed from lowest to highest concentration. An amber (591nm) LED (#MR-L0000-20S, Luxeon Star LEDs) was used as a light source. Rather than using the spectrometer described in previous chapters, the ring resonator output fiber led simply to a PMT (H5783-01, Hamamatsu). The PMT current output was converted to voltage by a custom circuit and the voltage was recorded using an analog-to-digital convertor.

Shown in Figure 5-3 is the raw detected output from the (PMT) as the sample in the LCORR goes from DI water to MB solutions of 10^{-6}, 10^{-5}, and 10^{-4} M, respectively. This type of output would, most intuitively, be measured as percent transmission, T/T_o. In this case, T_o would be the output voltage in the case of DI water blank, with the dark (output with source off) output subtracted. An absorbance value could also be calculated, if desired, from Beer's Law in Equation 2-1. This would be treated as an estimate, as the PMT output is recording a spectral range rather than a single wavelength, as is the case in a spectrometer, where absorbance is traditionally measured. Although the PMT and data recording equipment used is more costly and sophisticated than a simple photodiode with basic circuitry, this experiment and illustrates the same type of data that would be produced, thus demonstrating the feasibility of a very low-cost device for surface absorption detection

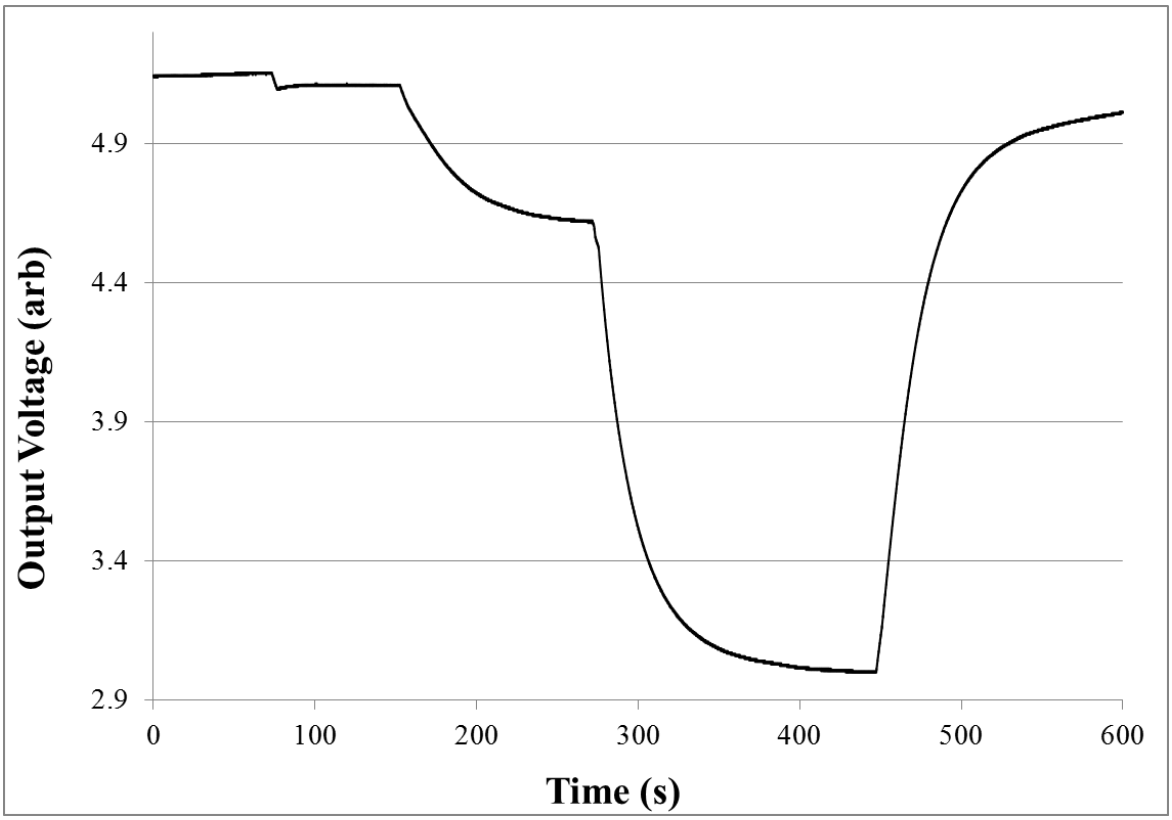

Figure 5-3 – Simple PMT detection of MB using a 592nm LED. The output voltage is converted from PMT current, which is a function of light output being detected. The three successive drops in transmission were from increasing the concentration from zero to 10^{-6}M, then to 10^{-5}M, then to 10^{-4}M. Finally, the capillary was washed out.

Beyond the cost-reduction and simplification at the source and detector ends of the system, as demonstrated in the above two experiments, the ring resonator itself must be investigated for a thorough analysis. Microfabricated ring resonators have been demonstrated by a number of researchers. (Xu, Fattal, & Beausoleil, 2008) (Scholten, Fan, & Zellers, 2011) (Kim, et al., 2010) (Fan, Advanced Photonic Structure for Biological and Chemical Detection, 2009) In these instances, the methods are usually based on lithographic etching of a solid material. For this reason, mass production is easily envisioned- thereby significantly reducing cost. As discussed in more detail in Chapter 1, the main limitation with microfabricated ring resonators is the reduced

resonator quality (smoothness) as a result of the etching process. (Deyl & Svec, 2001) In Chapter 4, the resonator quality was discussed in detail, with the conclusion that lower quality resonators were compatible with the analytical methods introduced in this work. While that discussion was not pertaining specifically to the simplified, monochromatic analysis proposed in this section, it is reasonable to assume that the compatibility would hold true in this scenario. Shown in Figure 5-4 is an overall schematic of a low-cost, simplified ring resonator system utilizing the components discussed in this section- an LED, photodiode detector, and microfabricated ring resonator.

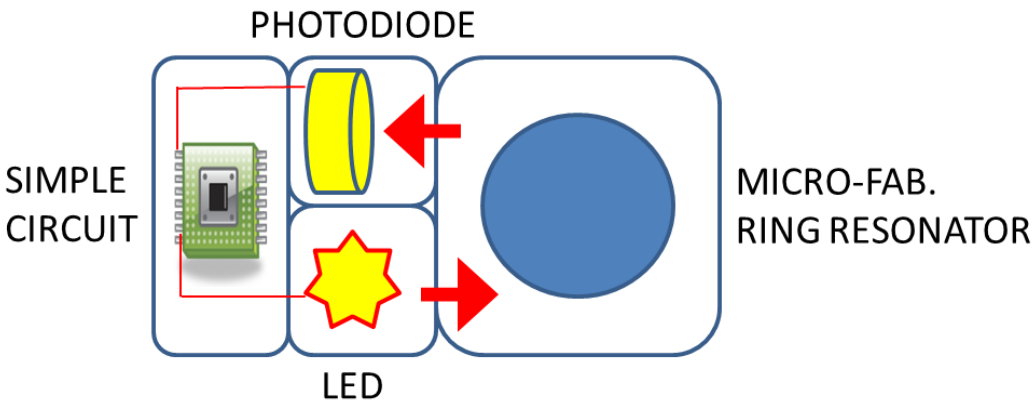

Figure 5-4 – Schematic of possible simplified, low-cost ring resonator system.

Portability Analysis

An exhaustive analysis to demonstrate portability feasibility would be premature. In its current form, the broadband ring resonator device is highly immobile. In the previous section, components such as LEDs, photodiode detectors, and microfabricated ring resonators were proposed for a simplified and low-cost system. In doing so, a portable device could easily be envisioned. LEDs and photodiode detectors, as well as the simple circuitry to operate them, are easily powered by battery. Also suited for portability, microfabricated ring resonators generally

have no moving parts or physical adjustments required, and are typically constructed from non-breakable materials. While these components may lead to an easily portable device, it must be emphasized that this type of analysis is restricted to the monochromatic detection described in the previous section. As discussed above, monochromatic analysis is limited in the information produced, as well as sensitivity, but is appropriate for certain applications where a limited number of analytical outcomes (i.e., analytes that will produce the measured signal) are possible.

If spectral information and more substantial data are desired, one can also envision a portable broadband ring resonator device that employs a portable spectrometer. This system would certainly not be as inexpensive as a monochromatic one, primarily due to the cost of a spectrometer relative to a simple photodiode. For an example of a portable model, Ocean Optics produces the handheld 'STS Microspectrometer' that is 40 mm x 42 mm x 24 mm and consumes only 0.75 W of power. (STS Microspectrometer, 2012) This particular model contains a 600 g/mm grating, and it is likely that most portable spectrometers would not be pre-configured with a higher resolution than this. The enhanced absorption methods in Chapter 2 as well as the chemometric RI analysis in Chapter 4 make use of common (relatively low) resolution devices. Incorporating a portable spectrometer with a higher resolution grating, such as the 2400 g/mm used in Chapter 3, should theoretically be approximately the same cost except for the lack of demand requiring custom construction. On a large production scale of ring resonator systems, this would become negligible.

Dynamic Range Analysis

With the ability to analyze sample concentrations over five orders of magnitude, or more, certain applications in biological and industrial settings are likely well suited for broadband ring resonator analysis. (Zourob & Lakhtakia, 2010) (Simhi, Gotshal, Bunimovich, Sela, & Katzir, 1996) (Steele, 2007) (Burdick, 2002) While one can easily envision the benefits to high sensitivity and a low detection limit, in certain situations there is a need for lower sensitivity. Attenuated total (internal) reflection (ATR) spectroscopy is often employed, in probe format typically, in industrial process applications where samples can be highly concentrated, murky, or otherwise unsuitable for standard methods of absorption detection. (Blum & John, 2011) (Chai, Li, & Zhu, 2002) (Chai, Hou, & Verrill, 2005) (Howard, et al., 2009) (Billot, Couty, & Hosek, 2010) (Doyle & Tran, 1999) For absorbance measurement with surface sensors, the mechanism of detection is the attenuation of the evanescent field at the surface of reflection. (Harrick, 1979) As such, the effective path length is what dictates the sensitivity of the device. Effective path length was discussed in more detail in Chapter 2. Briefly, it represents the equivalent direct transmission path length that would cause the amount of sample interaction experienced evanescently by the surface sensor. (Tsunoda, Itabashi, & Akaiwa, 1992) (Tsunoda, Umemura, Ueno, Okuno, & Akaiwa, 2003) (Umemura, Kasuya, Odake, & Tsunoda, 2002) The effective path length is a function of the number of reflection points. Therefore, it can be longer in the case of a resonant sensor such as an LCORR, or intentionally shorter in the case of a probe sensor.

Industrial

In a ring resonator, the effective path length is enhanced through resonance. In the case of a highly concentrated chromophore in the core it is expected that the resonance of waveguide modes (core-interacting) would be diminished, along with the effective path length. This was demonstrated, in Chapter 4, to widen the dynamic range of concentrations detectable in the LCORR.

In an ATR probe, pictured in Figure 5-5, as few as two reflection points minimize the effective path length, allowing highly colored and murky solutions to be analyzed in situ. Doyle and Tran illustrated the potential for analysis of strongly absorbing chromophores by UV-visible ATR spectroscopy. (Doyle & Tran, 1999) This included photographic dyes and neat aromatics. Chai and coworkers extensively studied the use of UV-visible ATR for the analysis of the various components in kraft liquors during paper mill operations. (Chai, Li, & Zhu, 2002) (Chai, Hou, & Verrill, 2005) For reference, kraft liquors are caustic solutions that aid in the digestion of wood pulp into pure cellulose. As such, for this and many other industrial sampling environments, the durability and robustness of a possible ring resonator design must account for potentially harsh sample matrices and extreme temperatures.

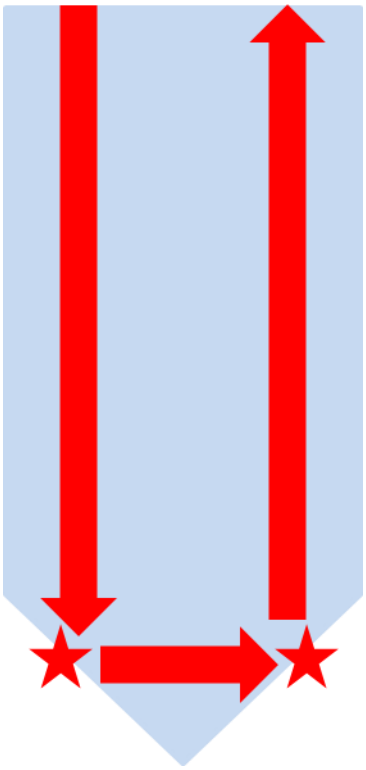

Figure 5-5 – Basic illustration of ATR probe mechanism. In this figure, incoming light makes two reflections before being reflected back up towards a detector. The evanescent field resulting from merely two reflection points results in a very minimal path length, thus ATR probe devices are useful for analyzing strongly concentrated and optically dense solutions.

Biological

In recent years, a number of potential biosensor applications have been demonstrated based on evanescent absorption. In some of these applications, the absorbance signal being measured is simply the attenuation of the overall evanescent field, not resolving any spectral information. This particular type of analysis was discussed earlier in this chapter, as a possible candidate for low-cost, simple (monochromatic) analysis. While this approach is attractively simple, the analytes and detection concepts can be taken a step further with regards to the information collected. A spectrometer could be used if spectral information is desired, either stationary or portable, as described earlier in this chapter. Burdick demonstrated the potential for surface ATR absorption

analysis of raw blood samples. (Burdick, 2002) He described that biomolecules of interest, in a specific binding assay for example, are detectable at the surface they are bound to without requiring that the light transmission pass through the optically dense blood cells.

Sample Volume Analysis

Certain applications could benefit simply from the potentially very small sample volume required for ring resonator analysis. Using Equation 5-1, the cross-sectional area of the inside of the 250 μm capillary is determined to be 0.049 mm^2. For every mm of capillary length, the volume occupied is, therefore, 0.049 mm^3, or 49 nL. These figures are illustrated in Figure 5-6. One mm is approximately, but greater than, the length of capillary utilized by the ring resonator, as estimated from the visibly illuminated region and space occupied by the slightly offset fiber tapers. Nonetheless, considerably smaller ring resonators have been demonstrated, and incredibly small microfabricated resonators can easily be envisioned.

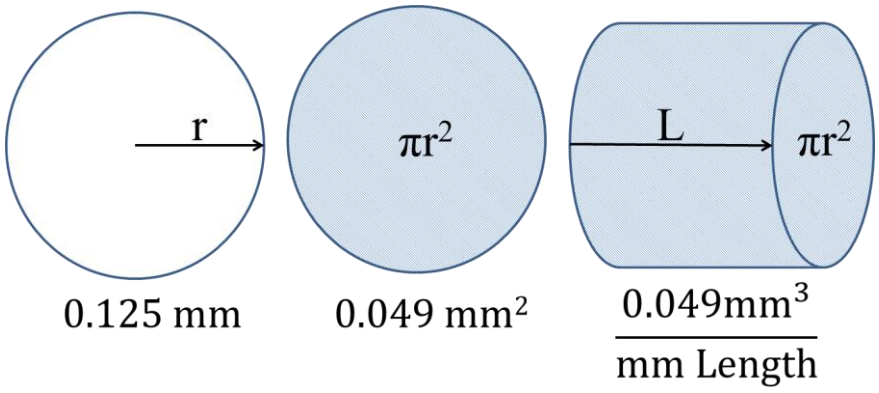

Figure 5-6 – Illustration of linear volume estimation. On the left, the radius of a 250 μm capillary is shown. In the middle, the area is determined, which is equivalent to the volume per linear distance in the capillary, on the right.

Historically, a vast number of reagent-based colorimetric techniques were used for a wide variety of analytes. (Onishi, 1978) These have largely been replaced by methods employing complex, modern instrumentation. Many reagent-based colorimetric methods are attractive due to their simplicity and low-cost. While some reagent-based techniques are still used because of this, some of the main disadvantages that have resulted in many being replaced include the toxicity of many reagents and solvents, the potential for human error in solution making and mixing, often poor detection limits, and large sample volumes often required. (Paradkar & Williams, 1994) (Shar & Soomro, 2006) (Abdollahi, Panahi, & Khoshayand, 2003) The last of these, sample volume, is easily solved in a broadband absorption ring resonator, as the volume required for a conventional UV/visible cuvette cell (1 cm path length) is on the order of 2-4 mL, many orders of magnitude greater than that required for a ring resonator. The poor detection limit of some colorimetric methods can be improved upon by the enhancement seen as a result of the building field intensity by resonant wavelengths of light. This was demonstrated, for surface-active dyes in particular, in Chapter 2. By reducing the reagent volumes necessary, and utilizing a sample cell (ring resonator) that it suited well to microfluidics, an automated mixing system could be envisioned with small reservoirs of reagents. This would prevent human error associated with the measuring and mixing processes. Older analytical methods are more likely to utilize carcinogenic solvents and other hazardous and toxic chemicals. While the replacement of these chemicals with less harmful alternatives is not something exclusive to ring-resonator sensors, there is no reason to believe the newer chemistries would be incompatible.

Classic Colorimetric Methods

For an experimental demonstration of a ring resonator-based improvement on a classic, colorimetric method, trace lead in water was analyzed using dithizone (1,5-dipheylthiocarbazone)

reagent. (Paradkar & Williams, 1994) (Dawson & Lyle, 1990) Pictured in Figures Figure 5-7 and Figure 5-8, dithizone is an organic molecule that forms metal complexes that absorb strongly in the visible spectrum. These complexes are highly immiscible in water and therefore classically these methods used chloroform or other organic solvents. (Morton, 1936) More recently, in the interest of environmental and safety concerns, methods using surfactants have been developed to allow aqueous sample analysis, eliminating the need for harmful solvents. (Paradkar & Williams, 1994) (Shar & Soomro, 2006) (Abdollahi, Panahi, & Khoshayand, 2003) (Khan, Ahmed, & Bhanger, 2005) As a demonstration of detectability and small sample volume, a standard methylene chloride-based extraction method was simply scaled down for analysis in the broadband LCORR. In a second experiment, surfactants were investigated as an alternative to the methylene chloride.

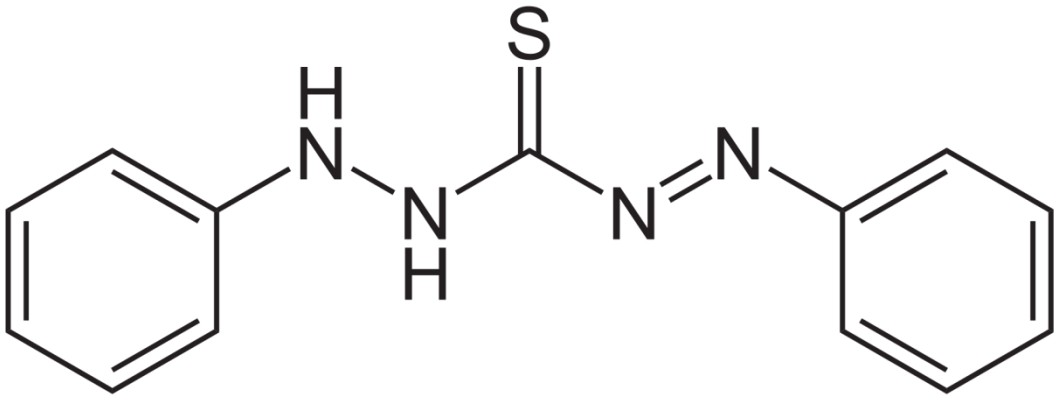

Figure 5-7 – Uncomplexed dithizone (1,5-diphenylthiocarbazone) molecule

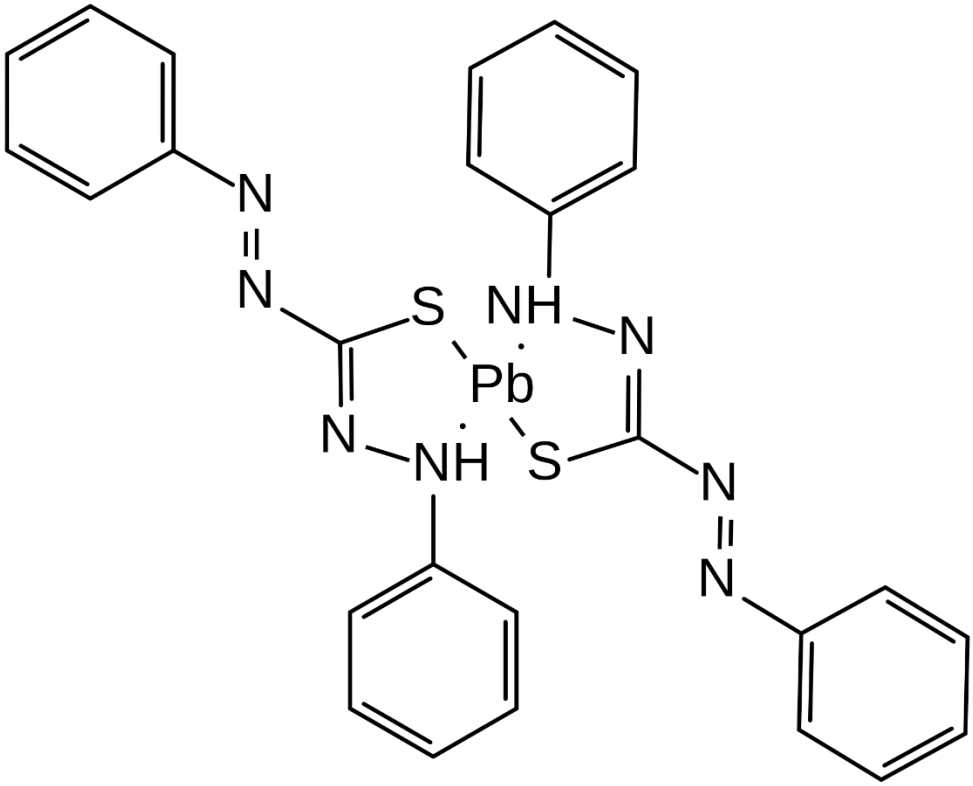

Figure 5-8 – Dithizone complex with Pb.

Experimental

Unless otherwise specified, all configuration parameters (e.g., taper positions) remained the same as in Chapter 2 for this experiment. Also, unless otherwise specified, all chemicals were obtained from Sigma-Aldrich. Powdered dithizone reagent (80% purity) was further purified by acid-base extraction using NH_4OH, H_2SO_4, and CCl_4. (Aprahamian, 1985) This was possible due to the solubility of dithizone in strongly basic solution but nearly complete insolubility in neutral and acidic solution. Lead samples were made simply by dissolving lead nitrate in deionized water. From an initial stock of 1000 ppm, all other solutions were made through serial dilutions, down to 10 ppb. Surfactants are environmentally hazardous, however to a lesser degree than organic

solvents. Briefly, a surfactant is a molecule that contains a polar and nonpolar groups, thereby allowing otherwise immiscible molecules to mix.

For the experiments involving organic extraction, purified powdered dithizone was dissolved in CH_2Cl_2 to a concentration of 30 mg/mL. One mL of this reagent was added to each 10 mL aqueous lead sample, in a glass centrifuge tube. The samples were agitated approximately 30 seconds. For analysis, the sample intake capillary was lowered to the bottom of each capillary tube to directly access the organic layer containing the Pb-dithizone complex. By leaving the aqueous sample in the tube, evaporation of the organic solvent was minimized, preserving original concentration.

In a separate set of experiments, surfactants were investigated as a means of eliminating the need for harmful organic solvents such as CH_2Cl_2. Shown in Figures 5-9, 5-10, 5-11, and 5-12 is a selection of surfactants used, including sodium dodecyl sulfate (SDS), cetrimonium bromide (CTAB), benzalkonium chloride, and Triton X-100, respectively. Most of these were found to be unacceptable in dissolving detectable amounts of dithizone across a wide pH range. These surfactants were only capable at dissolving dithizone in alkaline solutions, where, at a pH high enough, dithizone will dissolve on its own without the aid of surfactants. One clear exception was benzalkonium chloride, which was found to be capable in a wide range of basic, neutral, and acidic pH solutions. For each lead sample analyzed using benzalkonium chloride, a solution of 0.5 mg/mL dithizone and 0.1 mg/mL benzalkonium chloride was created in deionized H_2O. For each sample analyzed, 0.5 mL of this solution was mixed with 0.1 mL of each lead sample. As separate phases were not present, the sample solutions were diluted to have $1/6^{th}$ the lead concentration that they originally had.

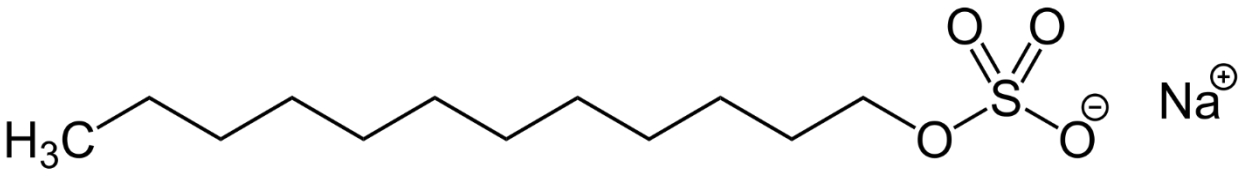

Figure 5-9 – Sodium dodecyl sulfate (SDS) molecule.

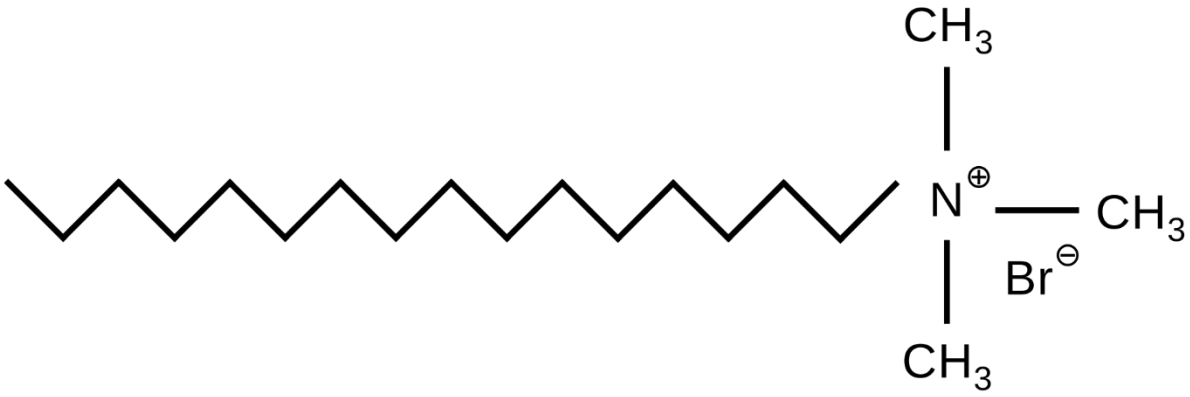

Figure 5-10 – Cetrimonium bromide (hexadecyl-trimethyl-ammonium bromide) molecule.

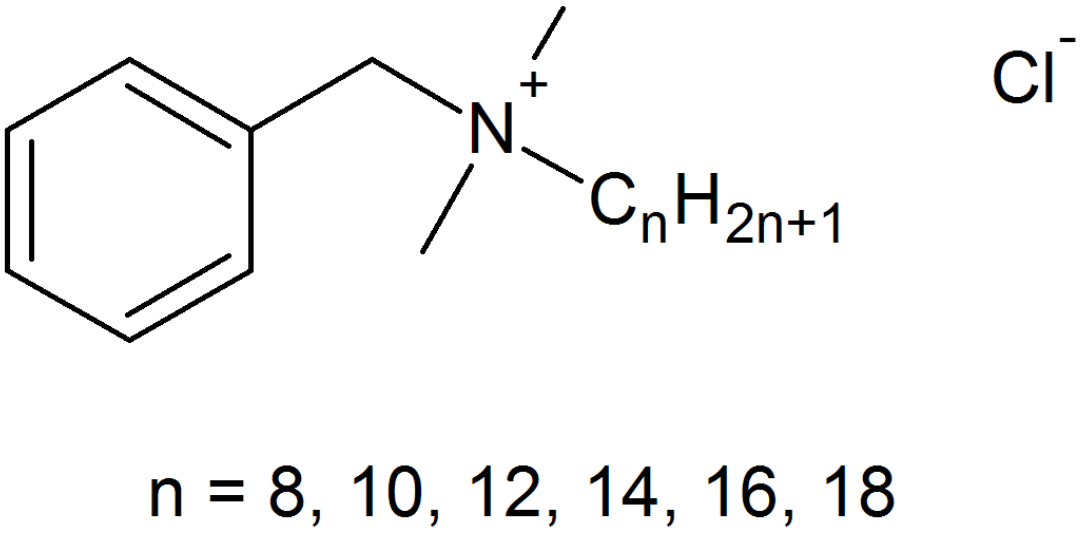

Figure 5-11 – Benzalkonium chloride molecule.

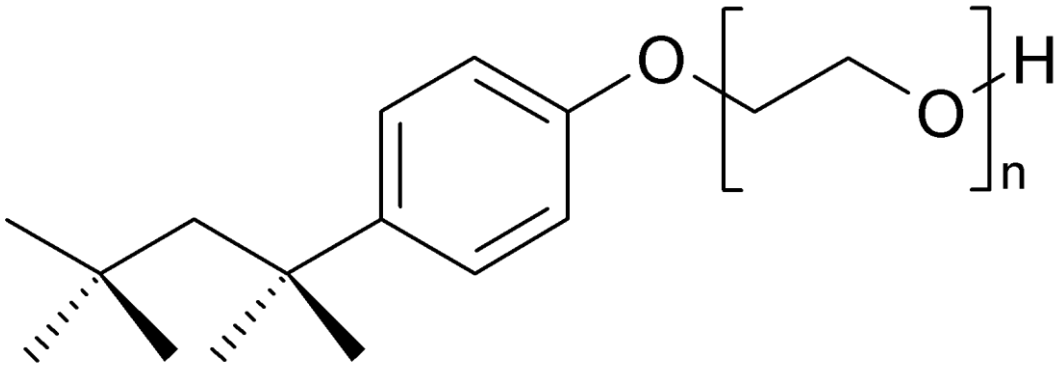

Figure 5-12 – Triton X-100 (polyethylene glycol octylphenyl ether) molecule.

Results

Shown in Figure 5-13 are the spectra collected for the dithizone in CH_2Cl_2 samples in the broadband LCORR. These agree with the spectra published by Fitch, taken by standard cuvette measurement. (Fitch, 1998) For comparison, the sample volume being analyzed in the cuvette is approximately 50,000X greater than that in the LCORR. Fitch proposes that, for the uncomplexed dithizone, the peak around 620 nm corresponds to a thiol form and the peak around 450 nm corresponds to a thione form. In other words, the molecule rotates between an open and cyclic ring, respectively. He also proposes that the absorption band shift for the lead complex is a result of increased rigidity throughout the molecule. If a simple, low-cost device were desired for a simple colorimetric method such as this one, one could envision a system that incorporates a limited number of LED sources, selected for the proper absorption bands, and a simple photodiode detector, as described earlier in this chapter, monitoring the transmission of light at these wavelengths. Such data is simulated in Figure 5-14, extracted from the spectra in Figure 5-13. A simple "YES/NO" output could easily be envisioned, corresponding to a detection limit.

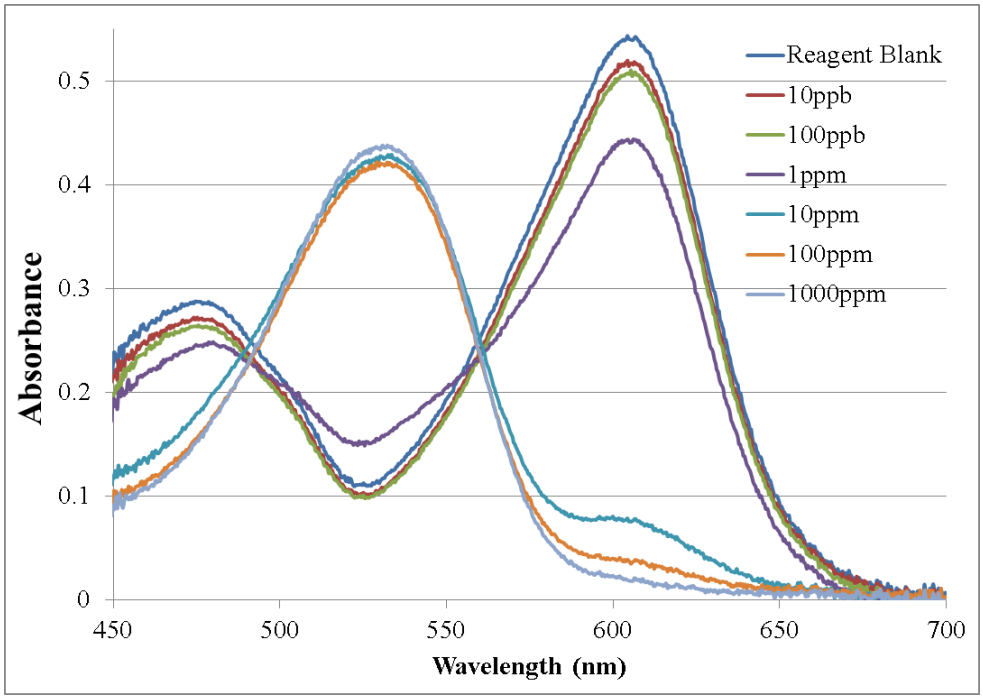

Figure 5-13 – LCORR absorption spectra of dithizone and dithizone-lead complex for extractions of aqueous samples of varying lead concentration from 10ppb to 1000ppm.

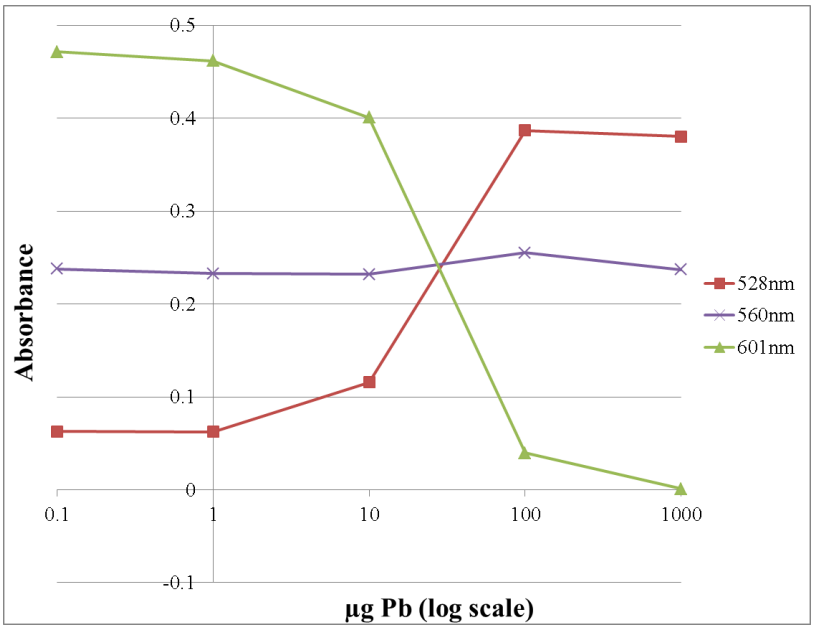

Figure 5-14 – To illustrate the type data that might be produced from a simple detection system, the plots above were taken from the spectra in Figure 5-13. This could represent the transmission of three LEDs of different wavelengths. In this case, 601nm represents the uncomplexed dithizone, 528nm the Pb-dithizone complex, and 560nm is a wavelength that could possibly be used as a reference.

Interpretation of the results for the surfactant-based sample solutions was not quite as clear. In these solutions, a wide absorption band appeared centered around 500 nm. In the presence of lead, assuming a lead-dithizone complex is formed, the peak appeared to shift red to 525nm. These spectra are shown in Figure 5-15. In comparison, three fairly clear peaks were shown in the CH_2Cl_2 spectra. One possibility for the appearance of the surfactant-based spectra is that the 620 nm peak, which Fitch proposed to be a thiol form of uncomplexed dithizone, is not present because it is less favorable than the thione form in the presence of the surfactant. (Fitch, 1998) If the remaining two peaks, corresponding to the thione form and the lead complex, were shifted closer to each other this would likely produce the spectra shown in Figure 5-15. While this data is not as clear as the CH_2Cl_2 based spectra, one possible way to use it would be to monitor the relative transmission at multiple wavelengths, as described above, and calibrate the relative transmission of the wavelengths to concentration. As an example, the ratio of 520 nm to 475 nm absorbance is plotted against lead concentration in Figure 5-16.

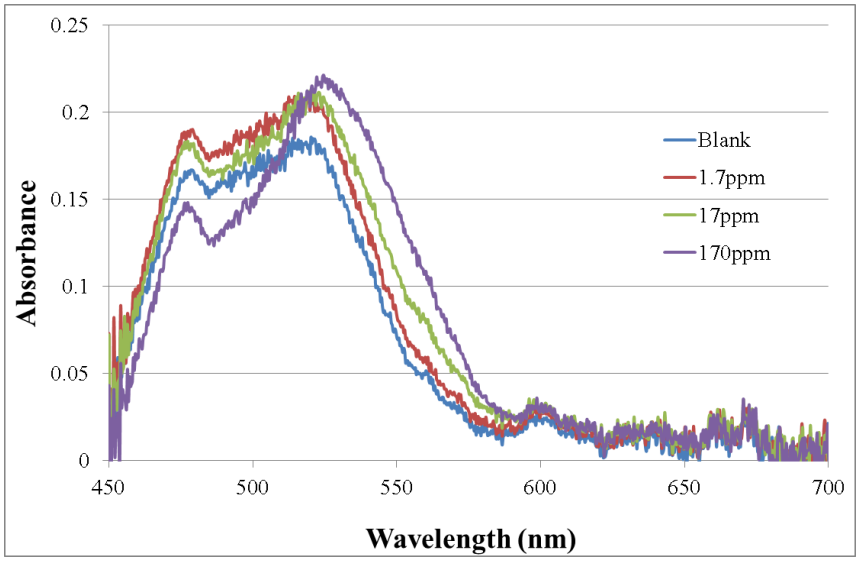

Figure 5-15 – Absorption spectra of aqueous dithizone and Pb-dithizone complex for varying concentrations of lead. Rather than extractions, these samples utilized benzalkonium chloride as a surfactant. In this case, the λmax vary from the solvent-based extractions in Figure 5-13.

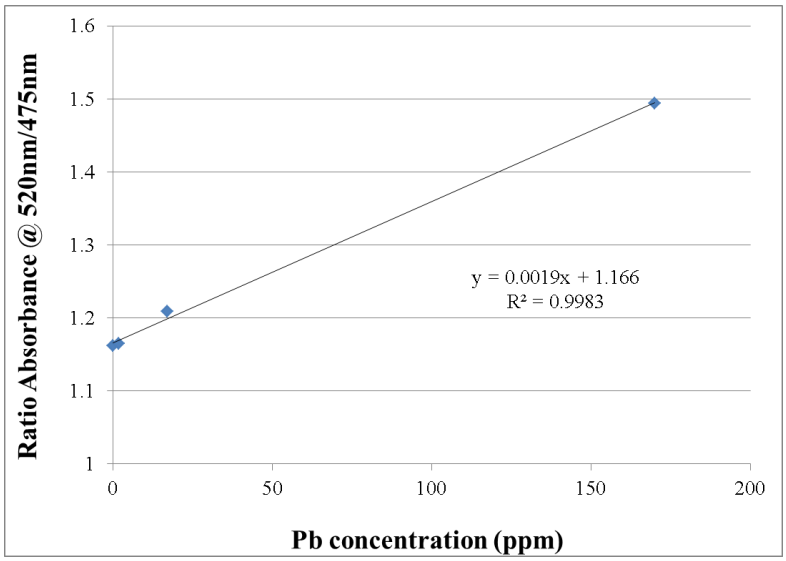

Figure 5-16 – As another approach to simplified detection methods for potential applications, the ratio of absorbance of 520nm to 475nm is plotted against lead concentration, from the spectra presented in Figure 5-15. This could represent data collected from two LEDs.

Theoretically, as benzalkonium chloride is a cationic surfactant, it should be surface-attracted in the same manner as a cationic dye. This, in turn, should aid in the detectability of the hydrophobic dithizone complexes, as they in turn would be brought to the surface. A comparison was not possible with a non-cationic surfactant, however, as none were found to produce acceptable results for use with dithizone complexes in likely sample matrices.

In this section, the feasibility for scaling down a classical reagent-based colorimetric analytical method is demonstrated. While in the first experiment one of the greatest disadvantages of the particular method, use of halogenated organic solvent, is still present, the reagent and solvent quantities required in a ring resonator-based method are theoretically several orders of magnitude than traditionally used in these types of methods. Additionally, in the second set of experiments, surfactant is used to avoid the use of harmful solvents. This demonstrates the possibility for using modified versions of reagent-based methods in a ring resonator device to increase their modern attractiveness.

Conclusion

From the research and experiments discussed above, potential absorbance applications on several fronts appear to be feasible. For absorption detection, it was shown that a light source and detector can be as simple an inexpensive as LEDs and photodiodes, respectively. If the desired application is something very simple and inexpensive overall, microfabricated ring resonators are the most logical format to pursue. These inexpensive components naturally favor a design that is also compact and portable. In Chapter 4, the dynamic range of detection for the ring resonator device was explored, both in terms of RI and absorption sensing. In terms of potential applications, both high and low absorption sensitivity can be desirable in certain situations.

A vast array of colorimetric assays has been developed over more than a century, but with declining use in recent years. If certain limitations can be overcome, they present a wide variety of potentially simple and inexpensive analysis methods. Some limitations include large required sample and reagent volumes, the use of hazardous reagents and solvents, and poor sensitivity. This chapter presented ring resonator-based analysis methods that overcame these limitations.

References

Abdollahi, H., Panahi, M., & Khoshayand, M. (2003). *Iran. J. Pharm. Res., 2*, 207-212.

Aprahamian, E. (1985). Role of the Interface in the Kinetics and Mechanism of Solvent Extraction Systems. *Ph.D. Dissertation, University of Arizona*.

Billot, P., Couty, M., & Hosek, P. (2010). *Org. Process Res. Dev., 14*, 511-523.

Blum, M., & John, H. (2011). *Drug Test. Anal., 4*, 298-302.

Bull, H. (1956). *Biochim. Biophys. Acta, 19*, 464-471.

Burdick, B. (2002). Evanescent-Wave Biosensors. In W. Law, N. Akmal, & A. Ismani, *Biomedical Diagnostic Science and Technology* (pp. 170-183). New York: Marcel Dekker.

Chai, X., Hou, Q., & Verrill, C. (2005). *J. Pulp Pap. Sci., 31*, 81-84.

Chai, X., Li, J., & Zhu, J. (2002). *J. Pulp Pap. Sci, 28*, 105-109.

Dawson, M., & Lyle, S. (1990). *Talanta, 37*, 443-446.

Deyl, Z., & Svec, F. (2001). *Capillary Electrochromatography.* Amsterdam: Elsevier Science B.V.

Doyle, W., & Tran, L. (1999). *Spectroscopy, 14*, 46-54.

Duff, D., Ross, S., & Vaughan, D. (1988). *J. Chem. Educ., 65*, 815.

Fan, X. (2009). *Advanced Photonic Structure for Biological and Chemical Detection.* Dordrecht: Springer.

Ferreira, A., Werneck, M., & Ribeiro, R. (2001). *Biosens. Bioelectron., 16*, 399-408.

Fitch, A. (1998). Lead Analysis: Past and Present. In C. Lochmuller, *Critical Review in Analytical Chemistry* (pp. 267-345). Boca Raton: CRC Press.

Graydon, O. (2007). *Nat. Photonics, 1*, 23.

Harrick, J. (1979). *Internal Reflection Spectroscopy.* Ossining: Harrick Scientific Corporation.

Howard, K., Nagy, Z., Saha, B., Robertson, A., Steele, G., & Martin, D. (2009). *Cryst. Growth. Des., 9*, 3964-3975.

Khan, H., Ahmed, J., & Bhanger, I. (2005). *Anal. Sci, 21*, 507-512.

Kim, G., Lee, H., Park, C., Lee, S., Lim, B. B., & Lee, W. (2010). *Opt. Express, 18*, 22215-22221.

Leung, A., Shankar, P., & Mutharasan, R. (2007). *Sens. Actuators, B, 123*, 888-895.

Morton, F. (1936). *Analyst, 61*, 465-471.

Onishi, H. (1978). *Colorimetric Determination of Traces of Metals.* New York: Wiley.

O'Toole, M., & Diamond, D. (2008). *Sensors, 8*, 2453-2479.

Paradkar, R., & Williams, R. (1994). *Anal. Chem., 66*, 2752-2756.

Scholten, K., Fan, X., & Zellers, E. (2011). *Appl. Phys. Lett., 99*, 141108.

Shar, G., & Soomro, G. (2006). *J. Chem. Soc. Pak., 28*, 331-336.

Simhi, R., Gotshal, Y., Bunimovich, D., Sela, B., & Katzir, A. (1996). *Appl. Opt., 35*, 3421-3425.

Skoog, D., Holler, F., & Nieman, T. (1998). *Principles of Instrumental Analysis.* United States: Thomson Learning.

Steele, R. (2007). *Nat. Photonics, 1*, 25-26.

Steiner, G., & Renschen, C. (1992). *Proc. SPIE, 1796*, 26-33.

STS Microspectrometer. (2012). Retrieved from Ocean Optics: http://www.oceanoptics.com/productsheets/sts_product_sheet.pdf

Technical LED Color Chart. (2012). Retrieved from OK Solar: http://www.oksolar.com/led/led_color_chart.htm

Thomas, M. (1996). *Ultraviolet and Visible Spectroscopy.* West Sussex: John Wiley & Sons, Ltd.

Tsunoda, K., Itabashi, H., & Akaiwa, H. (1992). *Bull. Chem. Soc. Jpn., 65*, 1581.

Tsunoda, K., Umemura, T., Ueno, H., Okuno, E., & Akaiwa, H. (2003). *Appl. Spectrosc., 57*, 1273.

Umemura, T., Kasuya, Y., Odake, T., & Tsunoda, K. (2002). *Analyst, 127*, 149.

Vdovin, G., Sarro, P., & Middelhoek. (1999). *J. Micromech. Microeng., 9*, R8-R20.

Xu, Q., Fattal, D., & Beausoleil, R. (2008). *Opt. Express, 16*, 4309-4315.

Yeung, K., Lu, Z., & Cheung, N. (2009). *Colloids Surf., B, 69*, 246-250.

Yokota, M., Okada, R., & Yamaguchi, I. (2007). *Meas. Sci. Technol., 18*, 2197-2201.

Zourob, M., & Lakhtakia, A. (2010). *Optical Guided-wave Chemical and Biosensors I.* New York: Springer.

CHAPTER 6

Refractive Index Applications

Intro

In Chapter 3, the concept of refractive index detection using data analysis of (relatively) broad interference spectra was demonstrated. In Chapter 4, the possibility of sensitive RI detection was further expanded to include a wide range of spectrometers of varying resolution. With these possibilities revealed, the potential applications can be explored. In this chapter, the advantages and disadvantages of broadband-based RI analysis will be looked at further with respect to potential applications. Additionally, an experiment demonstrating the RI-based detection of bovine serum albumin (BSA) will be discussed. BSA is often used as a surrogate for various proteins and other biomolecules in sensor/instrument development. (Fan X. , White, Zhu, Suter, & Oveys, 2007) (Alvarez & Lechuga, 2010) (Zhu, White, Suter, Dale, & Fan, 2007) (Suter & Fan, Handbook of Optofluidics, 2010)

Previously, in Chapter 5, potential applications were investigated on several fronts that apply to both absorbance and refractive index analysis, including advantages in reduced sample volume and potential portability. For the sake of redundancy, these topics will not be discussed again in this chapter.

Combined Absorbance and RI analysis

One of the attractive benefits of a broadband ring resonator is the ability to take absorption and refractive index measurements from the same device, without any physical configuration changes aside from, possibly, the detector. (Oates & Burgess, 2012) This is not to say, however, that the device is well-suited for *simultaneous* measurement of both absorbance and RI.

Theoretically, complication arises from the fact that refractive index is actually a complex function of real and imaginary parts. (Daly, 1984) (Harrick, 1979) Shown in Equation 6-1, the complex refractive index, $\tilde{n}$, is the sum of the relative phase speed, *n*, and the imaginary part, $i\kappa$, which corresponds to absorption losses. For most transparent matter, the refractive index across the visible region has an inverse relationship with wavelength. This relationship is therefore known as "normal dispersion." In contrast, where an absorption band is present, anomalous dispersion can occur, where the relationship is proportional.

Equation 6-1

$$\tilde{n} = n + i\kappa$$

Besides the theoretical complexities with truly simultaneous detection of absorption and RI, instrumental conflicts arise from the methods presented in Chapters 2 and 3. The higher resolution spectra collected for Fourier transform-based analysis used a 2400 g/mm grating, while the absorption data in Chapters 3, 4, and 5 used a lower resolution, 150 g/mm grating. While the spectrometer used in this work had the ability to quickly and automatically switch between multiple gratings, this is not necessarily the case for other spectrometers. In Chapter 4, a demonstration of RI calibration based on the multivariate, chemometric PLS modeling utilized the same 150 g/mm that was being used for absorption detection. The spectra produced in this experiment revealed dramatic peak shifts as a result of complex interfering relationships that simultaneously depend on refractive index. While chemometric analysis would be able to account for an absorption band in a fitting model of RI, conventional absorbance measurement would likely fail in the presence of a significantly changing RI. In the case of both absorption and RI simultaneously changing, one would likely resort again to multivariate chemometric methods to quantify absorption.

The physical configuration of the ring resonator device was, in fact, slightly different between Chapters 2 and 3, where absorption and refractive index were measured, respectively. This was simply due to the fact that the main experiments in the chapters were performed at different points in time, several months apart. With the refractive index measurements, a larger and steeper fiber taper was found to allow for greater quantities of light to be coupled into the ring, allowing better data quality. Many of the subsequent absorption-based experiments, including most of those in Chapters 4 and 5, were performed using the exact same configuration as the refractive index experiments of Chapter 3.

Improved Sensitivity Relative to Conventional Methods

By utilizing and analyzing many resonance peaks simultaneously, these methods produce results improved over what would be possible using a conventional, single wavelength/mode peak tracking method. (Oates & Burgess, 2012) In an attempt to quantify the estimated performance enhancement delivered by using the Fourier transform-based methods detailed in Chapter 3, further data analysis was performed on the same data that was used and presented in that chapter. Shown again in Figure 6-1, this interference spectrum was analyzed in terms of fringe spacing, $d\tilde{\nu}/dm$, in Chapter 3 and using this method a detection limit of 2.9×10^{-6} RIU was estimated.

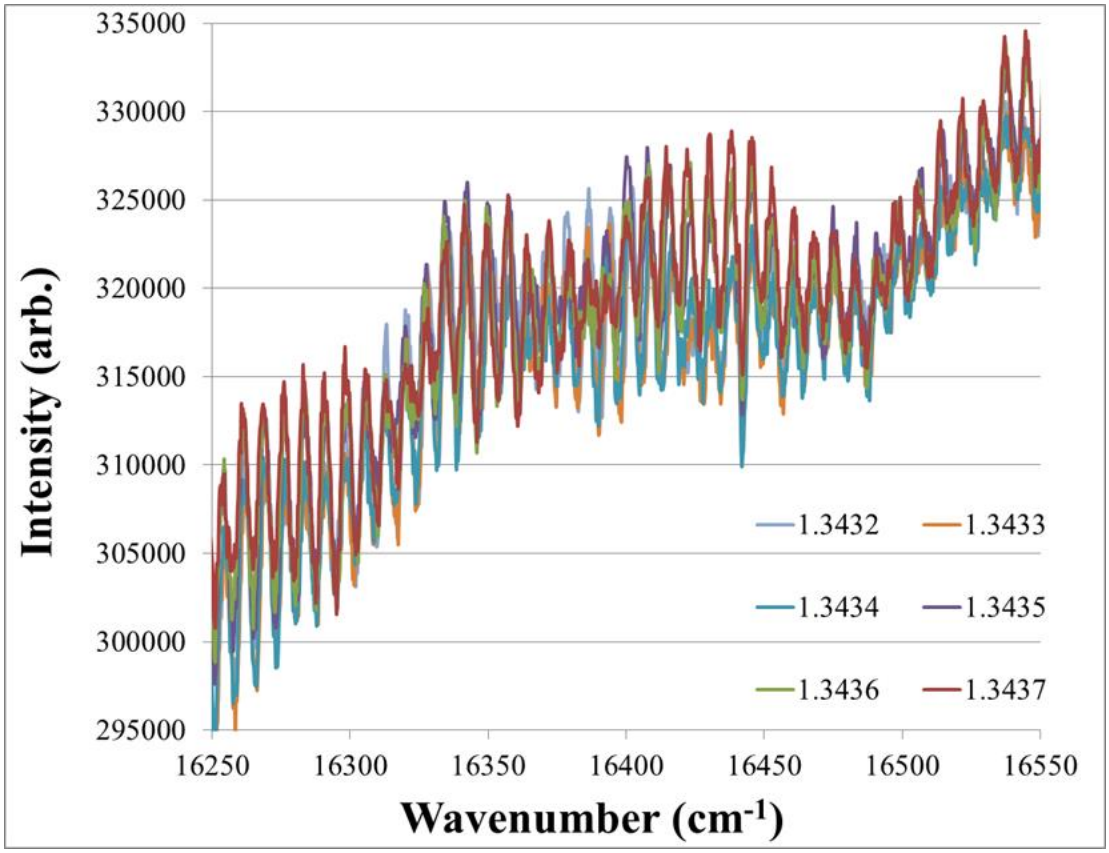

Figure 6-1 – Raw interference spectra of 6 IPA/water mixtures of varying RI.

In a much simpler method, based on those used by many researchers in the field of resonant sensors, the wavelength of a single, representative resonance peak was tracked. (Vollmer F. B., 2002) (Vollmer & Arnold, 2008) (White, Oveys, & Fan, 2006) (Arnold, Khoshsima, Teraoka, Hollser, & Vollmer, 2003) (Suter J. , White, Zhu, & Fan, 2007) (Suter J. , White, Zhu, & Fan, 2008) (Suter & Fan, Handbook of Optofluidics, 2010) (Fan X. , White, Zhu, Suter, & Oveys, 2007) (Fan X. , White, Zhu, Suter, & Sun, 2008) (Fan, Advanced Photonic Structure for Biological and Chemical Detection, 2009) This position was calculated from one half of the integral of the peak area, with the assumption of a symmetrical peak shape. The determined peak position is plotted against RI in Figure 6-2. The RI sensitivity using this method was found to be 0.6926 nm/RIU.

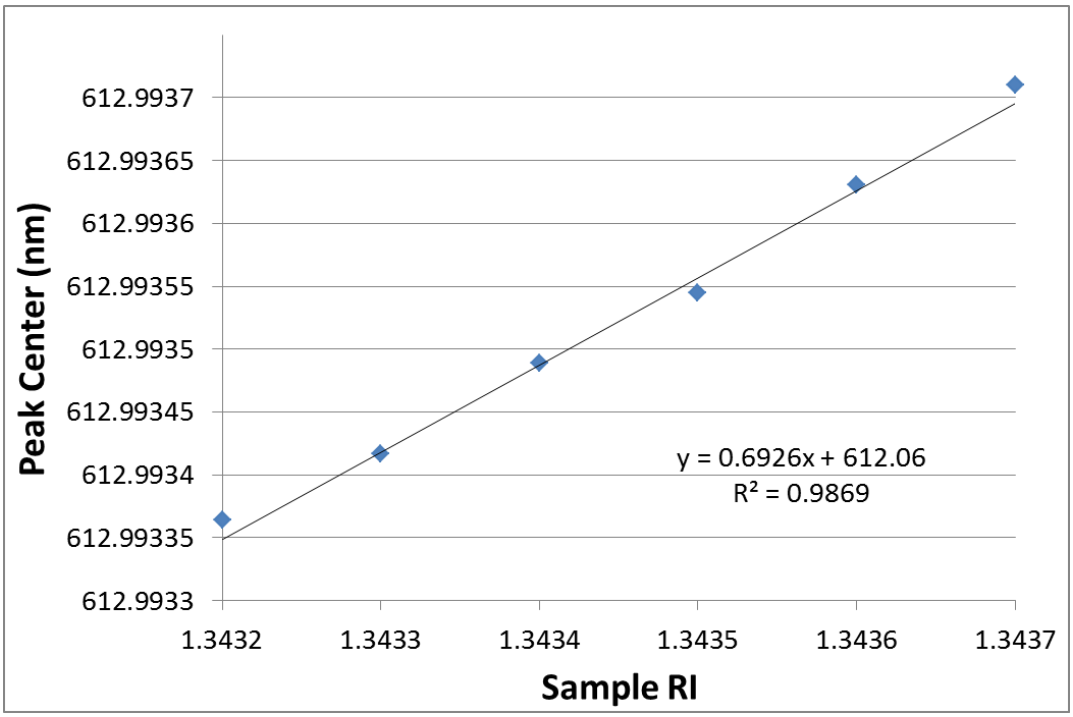

Figure 6-2 – Tracking of a single resonance peak across the 6 RI samples presented in Figure 6-1.

To produce the most direct comparison with the results presented in Chapter 3, the noise determination was conducted using the same raw data that was presented in Figure 3-16 from that chapter. Briefly, the sample solution was held constant for 30 minutes, while spectra were collected once each minute. This was done with the higher resolution, 2400 g/mm, grating installed in the spectrometer. In this case the noise was presented, in Figure 6-3, in terms of wavelength rather than $d\tilde{\nu}/dm$. From this, the noise (standard deviation of the baseline position) was found to be 2.85×10^{-5} nm. Taking three times this value to be the estimated detection limit, the minimum detectable shift in peak position would therefore be 8.55×10^{-5} nm. Based on Equation 6-2, using the RI sensitivity found above, an estimated detection limit of 1.2×10^{-4} RIU is calculated. The detection limit for the Fourier transform-based method was shown to be approximately 50X lower than this, revealing a significant enhancement and justification for that type of analysis.

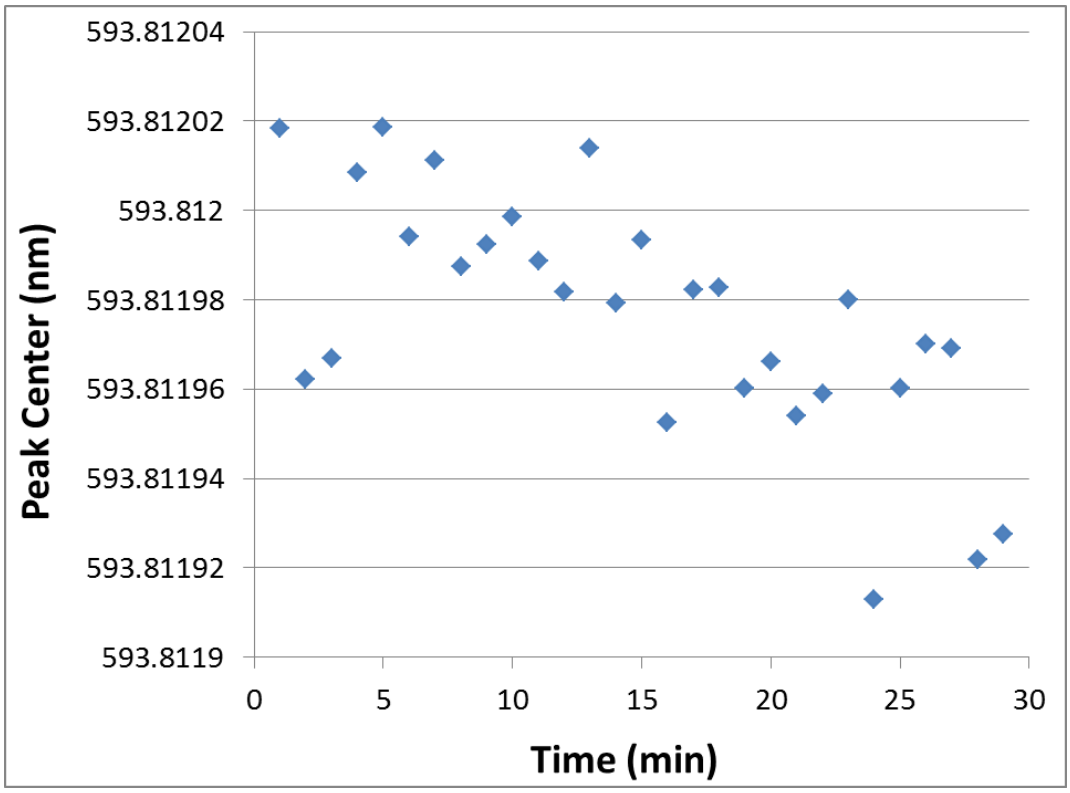

Figure 6-3 – For noise determination, the peak position of a representative resonance peak was tracked for 30 minutes. For the most direct comparison, this was created from the data used for noise determination using FT methods in Chapter 3.

Equation 6-2

$$Detection\ Limit(\text{RIU}) = \frac{3\sigma_{\text{noise}}(\text{nm})}{Sensitivity(\text{nm/RIU})}$$

Compatibility with Lower Quality Resonators

One of the greatest benefits to the Fourier transform-based analytical methods introduced in Chapter 3 is the compatibility with resonators of lesser quality. As shown above, the utilization of multiple resonance peaks produces improved detection limits and sensitivity, for a given resonator, over single mode methods. In a conventional single wavelength/mode analytical method, the detection limit is highly dependent on the resonator's quality. (Vollmer & Arnold,

2008) This restricts several pathways of sensor development that, beyond their quality limitations, would otherwise be possibly attractive in certain applications. One clear example of this is microfabricated ring resonators. (Scholten, Fan, & Zellers, 2011)

Ring resonators produced using microfabrication methods have precise and reproducible dimensions, but lack the "quality" (smoothness) of those produced using other methods such as pulling or melting, for LCORRs and microspheres, respectively. (Fan X. , White, Zhu, Suter, & Oveys, 2007) These methods can produce resonators with Q-factors in excess of 10^6, while microfabricated resonators typically achieve Q-factors on the order of 10^2-10^3. (Fan X. , White, Zhu, Suter, & Oveys, 2007) For potential real world applications, microfabricated devices are much more desirable and practical as they can be mass-produced. As the conventional ring resonator analysis, tracking a single resonance peak, is highly dependent on the resonator quality for peak resolution, and thus sensitivity, therein lays perhaps the greatest challenge to widespread ring resonator deployment in analytical sensing. Scholten, et al. attempted to design and construct an LCORR that could be microfabricated and also have the highest possible Q-factor. (Scholten, Fan, & Zellers, 2011) The device they produced, shown in Figures Figure 6-4 and Figure 6-5, produced resonance peaks with Q-factors on the order of 10^4.

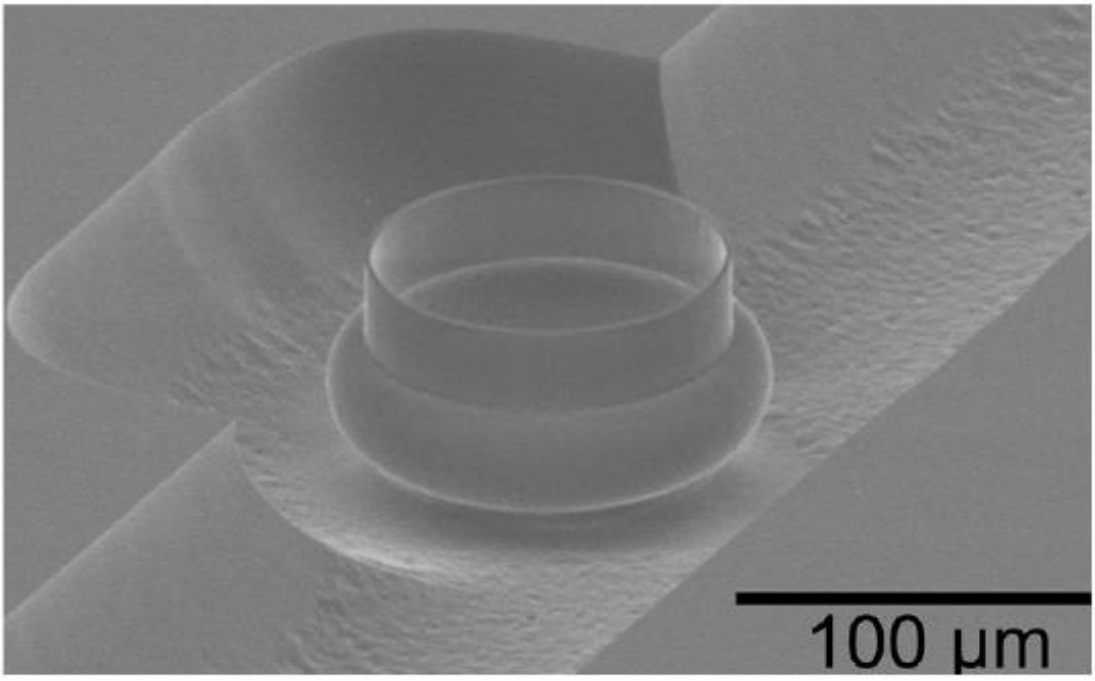

Figure 6-4 – SEM image of microfabricated optofluidic ring resonator. Reprinted with permission from Scholen, Fan, & Zellers. Copyright 2011, American Institute of Physics.

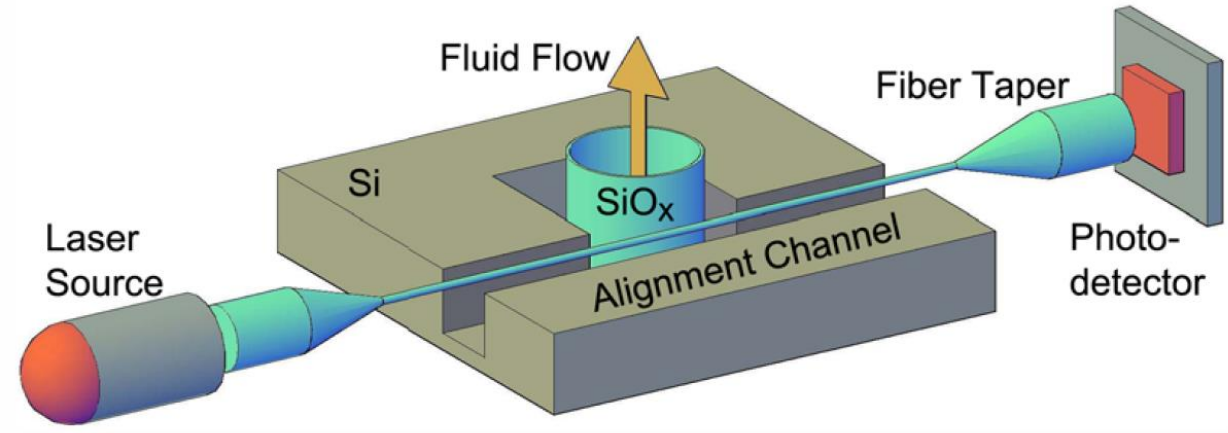

Figure 6-5 – Diagram illustrating the basic structure and operation of the microfabricated optofluidic ring resonator pictured in Figure 6-4. Reprinted with permission from Scholen, Fan, & Zellers. Copyright 2011, American Institute of Physics.

The ring resonator operation and analysis method presented in Chapter 3 overcomes the need for extraordinarily high Q-factors. By utilizing many resonance peaks simultaneously and analyzing the spacing between them, rather than their absolute positions, detection limits were considerably better than would be predicted for the same resonator using conventional single wavelength peak tracking method. This comparison was presented in Chapter 4. The LCORR used in this entire work was thinned exclusively by means of etching. Therefore, the quality is estimated to be more comparable to microfabricated rather than pulled resonators. Also in Chapter 4, an "estimated Q-factor" was determined to be 5500, which is on the same order as the microfabricated resonators referenced; however, this is a very crude estimate as there will be a broad number of propagating modes, wavelengths, and thus Q-factors present during analysis.

Compatibility with Existing Applications

In the field of analytical chemistry, many of the applications that are based on the detection of refractive index involve surface sensing of biomolecules. (Hunt & Armani, 2010) (Mendelson, 2000) Immunological assays, such as shown in Figure 6-6, generally involve functionalizing a surface with an antibody specific to the analyte of interest, then introducing the sample possibly containing that particular analyte. (Boisde & Harmer, 1996) At this point, step 2 in the figure, sensors that detect a surface refractive index change would be able to detect a shift as the analyte of interest bound to its complementary antibody. Refractive index sensing in this manner is often coined "label-free", as no further chemistry is required to detect the analyte binding. In other applications, after the analyte (if present) is bound to the complementary antibody, more of the same antibody is introduced; however, this antibody is "labeled" or "tagged". The tag is usually

a fluorophore, sometimes a chromophore. As a result, very simple detection methods can be used, as the sample will have a fluorescent intensity, or absorbance respectively, that is proportional to the quantity of analyte present. While simpler to analyze, additional labor is required to perform the assay, and more importantly to manufacture the custom tagged antibody. This increases the attractiveness of label-free RI-based methods.

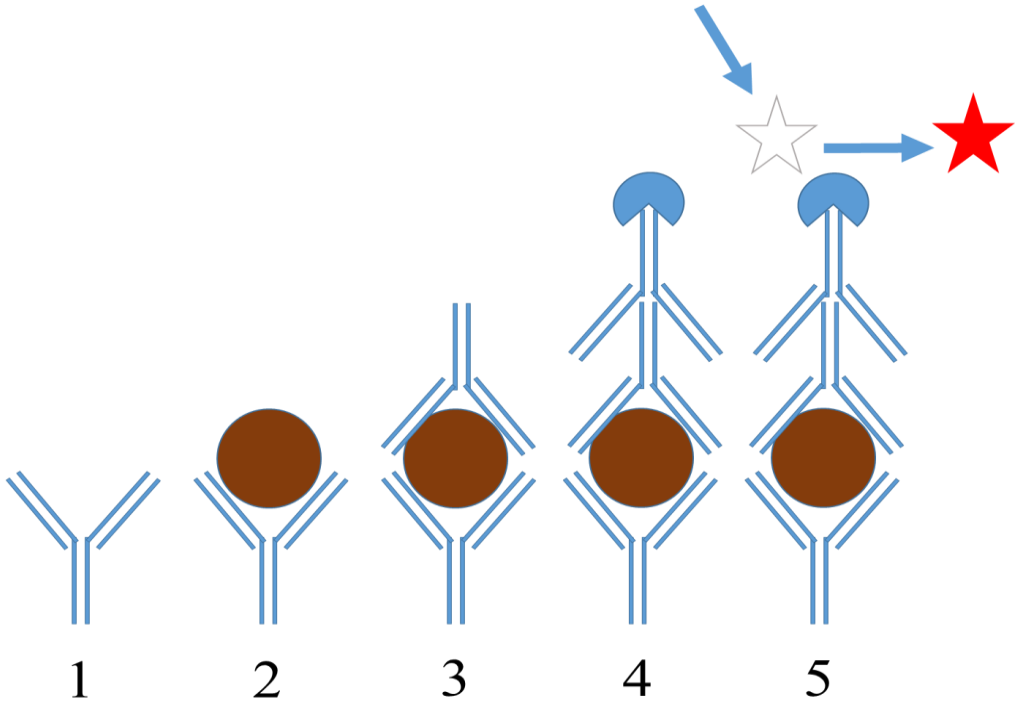

Figure 6-6 - A sandwich immunoassay (1) Plate is coated with a capture antibody; (2) sample is added, and any antigen present binds to capture antibody; (3) detecting antibody is added, and binds to antigen; (4) enzyme-linked secondary antibody is added, and binds to detecting antibody; (5) substrate is added, and is converted by enzyme to detectable form. Note that an RI sensor would produce a signal at step (2).

A number of different surface RI sensors have been demonstrated and developed for label-free biosensing. (Hunt & Armani, 2010) (Mendelson, 2000) (Zourob & Lakhtakia, 2010) Several different biosensing demonstrations have been made in ring resonators, specifically, using single resonant wavelength peak tracking, as described earlier. (Vollmer & Arnold, 2008) (Fan, Advanced Photonic Structure for Biological and Chemical Detection, 2009) Their widespread

commercial deployment could therefore possibly be hindered to some degree by the limitations with single-wavelength analysis discussed in the previous section. One could expect that nearly any RI sensing application using any similar device, especially another ring resonator, should be translatable to the broadband methods described in this work.

To verify the feasibility of surface RI detection, and application of broadband RI sensing methods towards biomolecules, an additional experiment was performed. While the studied sensing mechanisms were already shown, theoretically and practically, to detect analytes very near the surface, within the evanescent field, this was not yet explicitly demonstrated for RI sensing. To verify this, solutions of Bovine Serum Albumin (BSA) were analyzed. BSA is a commonly available protein, as a byproduct of the beef industry, often used in sensor characterizations in early method development. This is due not only to BSAs availability, but its tendency to adsorb to a variety of surfaces. (Bull, 1956) (Yeung, Lu, & Cheung, 2009)

Solutions of BSA were created from pH 4.5 buffer solutions of monosodium phosphate (MSP). Previous literature showed adsorption of BSA on silica surfaces to be maximized at a slightly acidic pH. (Bull, 1956) (Yeung, Lu, & Cheung, 2009) An initial 3 mg/mL stock solution was created and serial dilutions were created down to 7.5×10^{-3} mg/mL. BSA solutions were drawn into the capillary by the syringe pump and then stopped and held in place for 30 s to allow a fixed amount of time for surface binding. Solutions were analyzed from lowest to highest concentration. Many solvents and alkaline solutions were found to clean the surface to restore back to baseline conditions. (Baker, Laiwalla, Yoon, Canavate, & Garrel, 2001)

Shown in Figure 6-7 is a plot of FT peak center position as a function of BSA concentration in the bulk solution. A gradually diminishing incremental sensitivity can be seen as the

concentration is increased. As concentrations increase, the surface sites are taken by BSA molecules, leaving fewer available for additional molecules to adsorb. The shape of the plot in Figure 6-7 is logarithmic as a result, and agrees with the results found in Chapter 5 where transmission loss of internally reflected light was measured as a function of BSA concentration. The logarithmic shape of the plot also agrees with the surface preconcentration and absorption detection of a surface-attracted dye, methylene blue, in Chapter 2. Based on the RI sensitivity of the Fourier transform-based method, found in Chapter 3 to be approximately 400 (cm^{-1}/fringe)/RIU, and the noise determined in that same chapter, the detection limit of this experiment is estimated to be 7.6 x 10^{-3} mg/mL BSA.

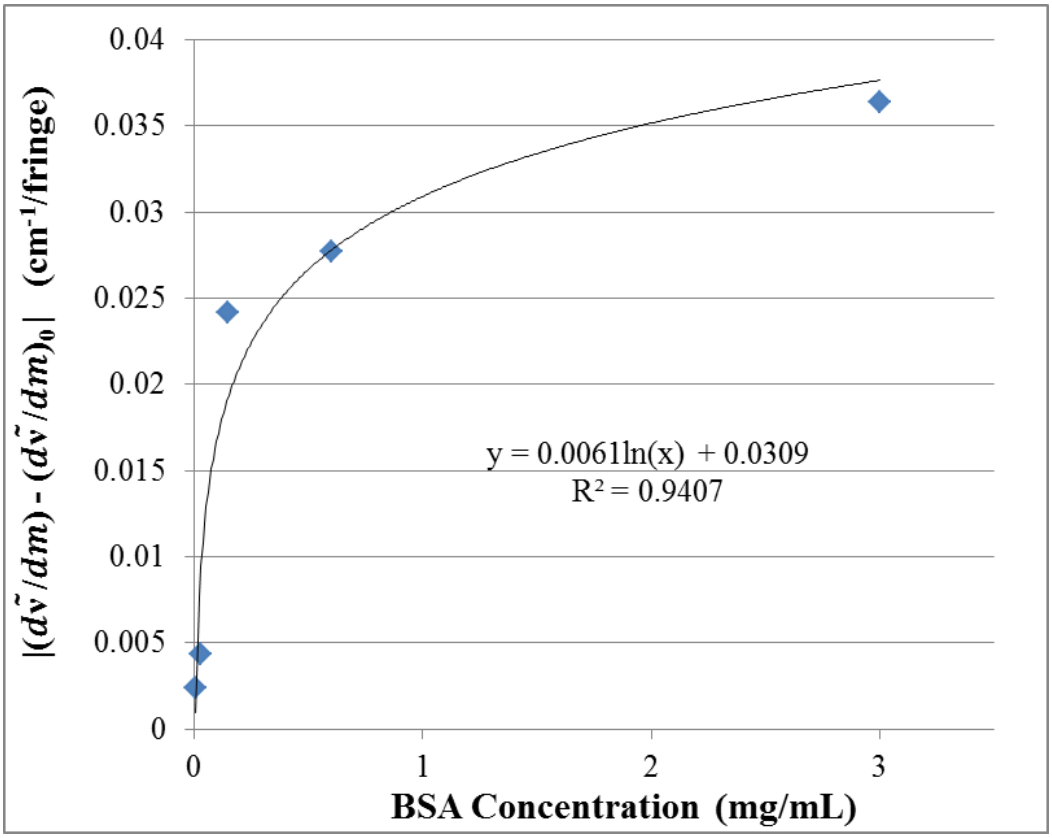

Figure 6-7 – Fringe spacing shift as a function of Bovine Serum Albumin (BSA) binding to the capillary surface with increasing concentration. Absolute, baseline-subtracted shift is shown for clarity.

In Chapter 2, it was shown that the surface kinetics of methylene blue adsorbing to the capillary surface fit to a Freundlich isotherm. A plot of $\log(C_{eff})$ vs. $\log(C_{bulk})$ was shown to produce a linear form with the slope of 1/n, which is a dimensionless heterogeneity factor, and an intercept of $\log(K_f)$, representing the Freundlich constant. (Proctor & Toro-Vazquez, 1996) (Sharma, 2012) If fringe spacing, $d\tilde{\nu}/dm$, is assumed to be linear with a change in surface refractive index, as was shown in Chapter 3, and refractive index is assumed to be linear with protein concentration, then the Freundlich model could be used to approximate the surface kinetics of BSA adsorption. By plotting $\log(d\tilde{\nu}/dm)$ vs. $\log(C_{bulk})$, a fairly linear relationship is confirmed in Figure 6-8.

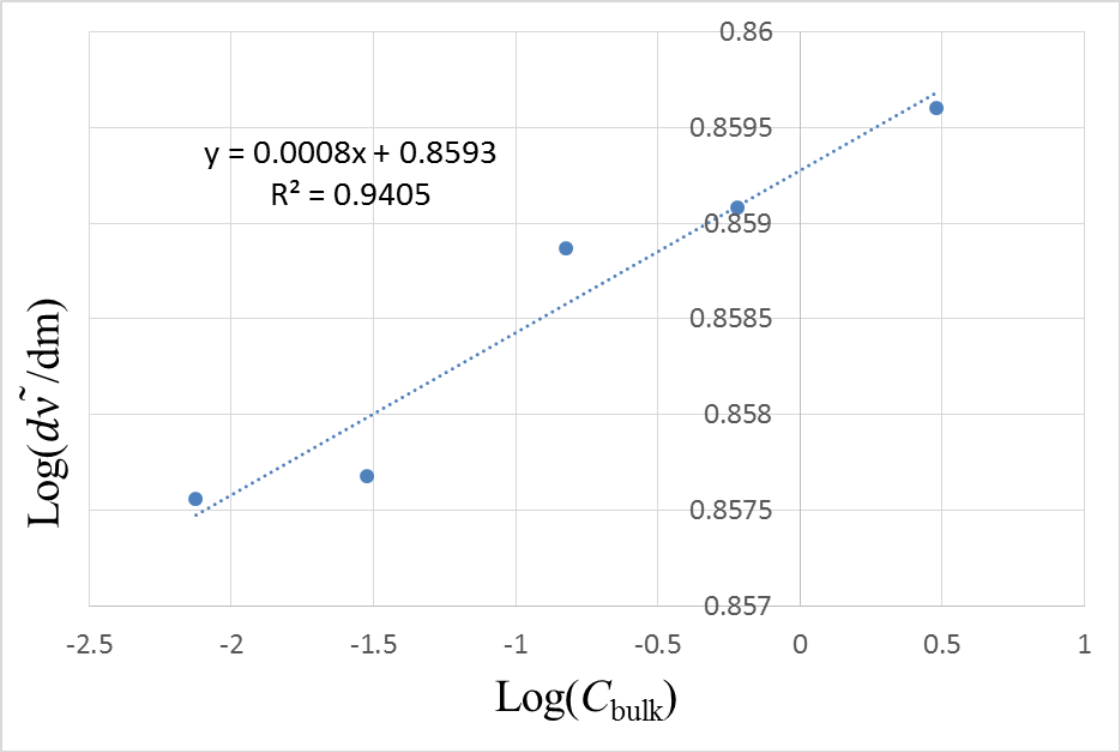

Figure 6-8 – Freundlich adsorption model for data presented in Figure 6-7.

It should be emphasized that the goal of this experiment was not to detect the smallest possible quantity of protein, but rather to verify the surface detectability in RI sensing and demonstrate the feasibility of the presented broadband Fourier transform-based analysis for biomolecule sensing. Were the goal to detect the smallest quantity of BSA possible, surface functionalization would have been investigated to further concentrate the protein to the surface, as numerous other researchers have. (Fan X. , White, Zhu, Suter, & Oveys, 2007) (Alvarez & Lechuga, 2010) (Zhu, White, Suter, Dale, & Fan, 2007) (Suter & Fan, Handbook of Optofluidics, 2010) Additionally, as other researchers have done while demonstrating (BSA) detection, longer wait times of minutes, or hours, rather than seconds could have been used to maximize the surface adsorption. (Zhu, White, Suter, Zourob, & Fan, 2007) (Suter J. , White, Zhu, & Fan, 2008)

One could assume, from the demonstrated feasibility of biomolecule detection, that most RI based detection applications could be translated to a broadband ring resonator for analysis using the methods described in this work.

Conclusion

In this chapter, some of the device characteristics specific to refractive index sensing were discussed in the context of potential applications. While one of the distinct advantages to using a broad-band ring resonator is the ability to take both absorbance and RI measurements; however, due to the complex relationship between absorption and RI, a careful and scientific approach must be taken in order to simultaneously measure both. Based on the additional data analysis shown in this chapter, the broad-band FT-based RI detection methods presented in Chapter 3 are estimated

to significantly outperform conventional single wavelength, peak tracking-based methods in terms of detection limit.

In Chapter 5, a thorough discussion was presented in terms of possible low-cost and portable ring resonator applications. One possibly critical component in these applications is a microfabricated ring resonator that could be produced on a large scale and at a low unit cost. The primary disadvantage to these resonators was mentioned as the reduced quality from the fabrication process. For this reason, the FT-based methods presented in Chapter 3, shown in Chapter 4 to be compatible with lower quality resonators, is a possibly attractive pairing for microfabricated resonators.

A vast number of analytical methods have been already developed for the sensing of a refractive index shift. Many of these are surface-based sensors that employ a specific binding chemistry and detect an RI shift at the surface resulting from a successful binding event. Many, perhaps most, RI sensing applications should be translatable a broad-band ring resonator. In the early stages of surface sensor development, a common proof-of-concept experiment is to detect a protein, such as BSA, binding to the surface. This was performed successfully using the broad-band ring resonator and FT-based analytical methods described above.

References

Alvarez, M., & Lechuga, L. (2010). *Analyst, 135*, 827-836.

Arnold, S., Khoshsima, M., Teraoka, I., Hollser, S., & Vollmer, F. (2003). *Opt. Lett., 28*, 272-274.

Baker, B., Laiwalla, A., Yoon, J., Canavate, J., & Garrel, R. (2001). *Polym. Mater. Sci. Eng., 85*, 115-116.

Boisde, G., & Harmer, A. (1996). *Chemical and Biochemical Sensing With Optical Fibers and Waveguides.* Boston: Artech House, Inc.

Bull, H. (1956). *Biochim. Biophys. Acta, 19*, 464-471.

Daly, J. (1984). *Fiber Optics.* Boca Raton: CRC Press, Inc.

Fan, X. (2009). *Advanced Photonic Structure for Biological and Chemical Detection.* Dordrecht: Springer.

Fan, X., White, I. S., Zhu, H., Suter, J., & Sun, Y. (2008). *Anal. Chim. Acta., 620*, 8-26.

Fan, X., White, I., Zhu, H., Suter, J., & Oveys, H. (2007). *Proc. SPIE*, 6452-18.

Harrick, J. (1979). *Internal Reflection Spectroscopy.* Ossining: Harrick Scientific Corporation.

Hunt, H., & Armani, A. (2010). *Nanoscale, 2*, 1544-1559.

Mendelson, Y. (2000). Optical Sensors. In J. Bronzino, *The Biomedical Engineering Handbook.* Boca Raton: CRC Press LLC.

Oates, T., & Burgess, L. (2012). *Anal. Chem., 84*, 7713-7720.

Scholten, K., Fan, X., & Zellers, E. (2011). *Appl. Phys. Lett., 99*, 141108.

Suter, J., & Fan, X. (2010). In A. Hawkins, & H. Schmidt, *Handbook of Optofluidics* (pp. 11(1-29)). Boca Raton: Taylor & Francis.

Suter, J., White, I., Zhu, H., & Fan, X. (2007). *Appl. Opt., 46*, 389-396.

Suter, J., White, I., Zhu, H., & Fan, X. S. (2008). *Biosens. Bioelectron., 23*, 1003-1009.

Vollmer, F. B. (2002). *Appl. Phys. Lett, 80*, 4057-4059.

Vollmer, F., & Arnold, S. (2008). *Nat. Methods, 5*, 591-596.

White, I., Oveys, H., & Fan, X. (2006). *Opt. Lett., 31*, 1319-1321.

Yeung, K., Lu, Z., & Cheung, N. (2009). *Colloids Surf., B, 69*, 246-250.

Zhu, H., White, I., Suter, J., Dale, P., & Fan, X. (2007). *Opt. Express, 15*, 9139-9146.

Zhu, H., White, I., Suter, J., Zourob, M., & Fan, X. (2007). *Anal. Chem, 79*, 930-937.

Zourob, M., & Lakhtakia, A. (2010). *Optical Guided-wave Chemical and Biosensors I.* New York: Springer.

CHAPTER 7

Final Conclusions

In conclusion of this work, two important questions can be answered. First, "What novel ideas and concepts has this research introduced?" Second, "What impact could these results have on future research and development in the field?"

In Chapter 2, broadband absorption detection was demonstrated in a liquid core optical ring resonator (LCORR). Dramatic increases in sensitivity for surface active analytes confirmed the success of this work. In the following chapter, refractive index measurements were demonstrated in the same device, opening up a novel alternative analytical method that could be applied to various ring resonators. By utilizing the complex relationship between the multiplicities of resonance wavelengths and propagating modes, RI detection limits for this very early proof-of-concept design easily met those of existing RI sensing devices.

Looking to the future, Chapter 4 further characterized the broadband ring resonator on several fronts including wall thickness, etching/thinning method, sources of noise, and detector resolution. These, and other, aspects must be carefully considered for future research and the design of future devices. Chapter 5 explored possible directions for future absorption-based applications of a broadband ring resonator. Some advantages that could lend direction to specific paths forward include the potential for both very low-cost and portable designs. In addition to these, the small sample volume required for analysis argues for an improved take on classic colorimetric assays, which were often rather simple and inexpensive. Finally, Chapter 6 looked at potential directions for RI-based applications. The advantages of the broadband ring resonator with regard to absorption-based sensing are also attractive for RI-sensing. In addition to these, the compatibility with lower quality resonators, which is generally the case for those that are microfabricated, opens doors for inexpensive and portable systems.

Vita

Thomas Oates grew up in Everett, WA. He attended Central Washington University in Ellensburg, WA and earned his B.S. in Chemistry in 2005. He then worked for Southwest Research Institute at the Umatilla Chemical Depot, near Hermiston, OR, from 2005-2008. After this, he attended the University of Washington in Seattle, WA and earned his Ph.D. in Chemistry in 2013.